Project Number: RYD-FR80

Electrochemical Characterization and Aging in PEM Fuel Cells

A Major Qualifying Project Report
submitted to the faculty of
WORCESTER POLYTECHNIC INSTITUTE
in partial fulfillment of the requirements for the
Degree of Bachelor of Science

Submitted to:
Professor Ravindra Datta

By:
Neal Dandekar
Alison Mendonca

February 29th 2012

Co-Advised by:
Botao Huang (ENSIC)
Francois Lapique (ENSIC)

Abstract

Fuel cell degradation and defects are factors that prohibit the commercialization of fuel cells. To understand how fuel cells may degrade, they are tested with and without defects to simulate real-world applications. By analyzing degradation patterns of a fuel cell stack, operating conditions and geometry within a stack can be optimized. Preliminary work analyzed a three-cell stack of healthy polymer electrolyte membrane fuel cells (PEMFC) under steady state conditions for four weeks. The voltage, resistance and water production of this stack were monitored each day to characterize degradation and aging. Further efforts utilized theoretical modeling to predict fuel cell performance of a single cell.

Experiments conducted on the healthy stack demonstrated that the mass transport and charge transfer resistances increased over time while the ohmic resistance remained constant. The degradation of the catalyst and gas diffusion layers may have caused the increase in mass transport and charge transfer resistances. Due to the increase in resistance, the overall potential of the cell decreased over time. Through the use of theoretical modeling, potential drop was predicted for data collected on a single cell and a stack. Resistances extracted from EIS could not be predicted from the model. Overall, experiments conducted at ENSIC in Nancy, France, provide a basis for future research.

Acknowledgments

We would like to express our gratitude to those who contributed and assisted in the completion of our project. We would like to acknowledge advisors in Nancy, France at ENSIC as well as those in Worcester at WPI. Many thanks to:

ENSIC

Botao Huang

Yohann Chatillon

Francois Lapicque

The LRGP & SysPol Teams

WPI

Professor Ravindra Datta

Professor Terri Camesano

Table of Contents

Table of Figures

Table of Tables

Nomenclature

C_{H2O}	water concentration
d_M	catalyst metal crystalline diameter
$E_{A,\varphi0}$	effective activation energy for HOR (34.6 kJ mol^{-1})
$E_{C,\varphi0}$	effective activation energy for ORR (67.0 kJ mol^{-1})
E_{μ}	activation energy for water viscosity (14000 kJ mol^{-1})
F	faraday's constant (96,485 C eq^{-1})
F_i	molar flow rate (mol s^{-1})
i	fuel cell current density (A cm^{-2})
i_{xc}	crossover current at the cathode
i_0	exchange current density (A cm^{-2})
i^*_{0ref}	exchange current density reference(A cm^{-2})
i_L	limiting current density (A cm^{-2})
K_A	equilibrium constant
k_{H2}	permeability of hydrogen (mol $bar^{-1}cm^{-1}s^{-1}$)
L_{EL}	thickness of electrolyte
M_{PT}	platinum molar mass (195.084 g/mol)
M_{RU}	ruthenium molar mass (101.07g/mol)
m_m	catalyst loading (mg cm^{-2})
p_i	partial pressure
R	gas constant (J mol^{-1} K^{-1})
R_{ct}	charge transfer resistance
R_{diff}	diffusion resistance
R_{Ω}	ohmic resistance
T	temperature (K)
T_{ref}	reference temperature
V_0	thermodynamic potential
V	fuel cell voltage
W	vapor content coefficient

Greek Symbols

α	water transport coefficient
$\alpha^{\cdot}$	transfer coefficient
β	degree of dissociation
δ	ratio of mutual to matrix diffusion coefficients
ε_0	Nafion® volume fraction
ε_E	water volume fraction
γ_m	roughness factor
λ	number of molecules absorbed per $-SO_3H$ group
ρ	density (g cm^{-3})
η	over potential
φ_I	available metal surface involved in electro catalysis in contact with ionomer
$\nu^{\cdot}_{ie-}$	electron stoichiometric number
σ_{EL}	protonic conductivity of the membrane
χ	percolation threshold

1.0 Executive Summary

Fuel cells are an ever-expanding topic of research in academia and energy-based industries. They are electrochemical devices that have fuel entering the cell continuously, and differ from battery cells which have a fixed amount of reactants. (Baker & Zhang, 2011) Interest in fuel cells has grown over time as dependence on fossil fuels triggered a global effort to find alternative sources of energy for electrical power generation and transportation applications.

Although considered a new age energy source, research on fuel cells can be dated back to 1838. In 1838, the fuel cell effect (electrolysis) or the decomposition of water into hydrogen and oxygen was discovered. It was not until approximately a year later that inverse electrolysis was utilized to produce electricity by forming water from hydrogen and oxygen. Although fuel cell research has been conducted over many centuries, much knowledge and research is still needed to perfect this alternative source of energy.

Worcester Polytechnic Institute has collaborated with Ecole Nationale Supérieure des Industries Chimiques (ENSIC) in Nancy, France to perform research on fuel cell operation and degradation. The focus of LRGP at ENSIC has been the degradation of proton exchange membrane fuel cells (PEMFC). Degradation and aging of PEMFC components have been a major limiting factor in the implementations of PEMFCs for real-world applications. In concept and practice, PEMFCs prove to be practical alternatives to batteries and engines in many applications if the lifetime of the cells can be ensured and validated.

Several past research projects have analyzed the degradation of single cell PEMFCs with various analytical techniques. (Choi & Moss, 2009) This project was split into two major sections: prolonged aging tests at nominal conditions and prediction of fuel cell performance by theoretical modeling. The first objective of this project was to observe aging of a PEM fuel cell stack comprised of three healthy cells under steady state conditions. This type of experiment, conducted over four weeks, was considered as a control stack that would provide aging patterns that could be compared to those of a defective stack. Electrochemical impedance spectroscopy and water management data were collected each day to monitor the resistance and aging within the fuel cell stack. Data could be analyzed from a cell to cell basis or as a stack.

The setup of the experiment consisted of a fuel cell bench with a three-cell stack, temperature indicator, flow meters and electrochemical data collectors. To ensure steady state conditions, the operating parameters of the stack were held constant by flow and temperature meters. At the anode, dry hydrogen gas entered the cell at 0.94 L/min at 55℃ . Humidified air at 55℃ and 62% relative humidity entered at the cathode at approximately 4.48 L/min. A constant current of 30A was applied to the stack. Through hot water heaters, the stack was maintained at a temperature of 55℃ and pressure of one atmosphere. Data from the stack was collected and analyzed each day.

The general procedures for the experiment were as follows: at the end of each day, effluent water from each electrode was collected and massed, followed by the collection and analysis of impedance spectroscopy. Water management and dynamics within the stack could be understood through the collection of the effluent water and temperature measurement at the anode and cathode. Through mass balances, the water transport coefficient and excess reactant coefficient of the stack were obtained. The analysis of resistances within the stack was acquired from Galvanostatic Electrochemical Impedance Spectroscopy (GEIS). Data exported from GEIS was fitted to Nyquist and Bode plots to determine ohmic, charge transfer and diffusion resistances occurring within the stack as well as through each cell. Cell and stack voltages were also monitored and recorded each day.

Under the same operating parameters and experimental procedures, a defective stack was analyzed. The stack was comprised of three cells in series with a defect, a pin hole, in the first cell's MEA. After operation for a week, experiments on the defective stack were terminated due to inconsistent hydrogen supply to the cell. The first cell was then altered to incorporate sixteen pinholes and was then tested to examine aging patterns. Again, due to inconsistent hydrogen supply, experiments were terminated.

The second objective of this project was to verify the use of theoretical models with fuel cells. To enhance the fuel cell durability, models have been made to predict how fuel cells perform under different operating conditions. One model used in this project is the polarization curve model. A polarization curve is standard electrochemical technique used to characterize the performance of a fuel cell. It is essentially a plot of cell voltage against current density under a set of constant operating conditions. By constructing a polarization curve, the effects of changes to operating conditions such as temperature, composition, and relative humidity can be systematically analyzed. In this project, a theoretical polarization curve was used to model data previously collected from a single cell PEM fuel cell. Although the polarization curve correlated to the data with little discrepancies, theoretical or calculated resistances did not correlate to resistances extracted from impedance data.

This report provides a basic overview of the history and working principle of a typical fuel and provides detailed information on the degradation and aging processes presented in literature. A description of diagnostic tools used to monitor aging and degradation within a fuel cell is also presented in the background of this report. The report also validates the use of theoretical models to predict fuel cell performance. In Chapter 3, a more detailed methodology of experimental procedures is described. Finally, results and analysis obtained from data are discussed in Chapter 4. The outcome of this project was twofold: a polarization curve model for single PEMFCs was validated and theorized mechanisms were utilized to describe chemical phenomena occurring in a three-cell healthy PEMFC stack.

2.0 Background

Fuel cells are favorable alternatives to conventional energy sources. They consume hydrogen and hydrocarbon fuels that contain substantial chemical energy. By utilizing hydrogen as the reactant, fuel cells have a potential to be more efficient, environmentally clean and silent compared to other means of energy production. Typically used as energy generators for small-scale applications, fuel cells can provide energy to rural areas outside the public grid where a huge cost of building an electrical network is required. Despite their advantages, there are some limitations to the usage of fuel cells. For example, due to aging and degradation during operation, the lifespan of a typical fuel cell is shorter than is required to be marketed as practical products. Other challenges include limited durability and accessibility to consumers. Regardless of limitations, fuel cells offer a promising source of alternative energy.

2.1 Fuel Cell Overview

2.1.1 History

The operation of a fuel cell is based on electrochemistry or the field of science that relates electricity with chemical phenomena. In 1791, Luigi Galvani discovered the field of electrochemistry by placing the tip of a scalpel on the internal nerves of a dissected frog which caused its muscles to contract (Srinivasan, 2006). Several years later in 1800, it was discovered that by sandwiching a membrane with zinc and silver plates and wetting it with salt water, electrical current would flow. It was not until 1838 that the “fuel cell effect” was discovered by C.F Schoenbein (Choi et al., 2006). Schoebein demonstrated the “fuel cell effect” (electrolysis) by immersing two platinum wires connected to a battery in a dilute acid. When submerged, bubbles of hydrogen and oxygen evolved on two electrodes. A year later, the invention of the “fuel cell” was made.

During 1839-1845, W.R Grove demonstrated Schoenbein's discovery by inventing the "gas battery" shown in Figure 1 (Larminie & Dicks, 2003). The experiment illustrated water being electrolyzed into hydrogen and oxygen by passing an electrical current on two externally connected platinum electrodes. Grove then showed that when the current was stopped, an electrical current could be generated when hydrogen and oxygen recombined on the platinum electrodes. In other words, hydrogen fuel was being "burnt" or combusted; however, instead of releasing heat energy, electrical energy was produced.

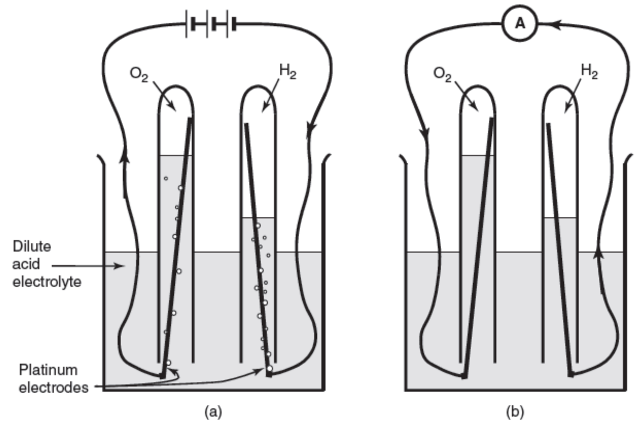

Note that the arrows represent the flow of negative electrons from – to +.

Figure 1 Experiment conducted by Grove. (a) Water is separated into hydrogen and oxygen (electrolysis) by the flow of an electrical current. (b) Reverse electrolysis. Hydrogen and oxygen are combined to form water and electricity. (Larminie & Dicks, 2003)

In 1839, Grove demonstrated the basic principle of a fuel cell stimulating interest in the field of electrochemistry. In Grove's model, due to low contact area and large distances between the electrode and electrolyte, the currents produced were minuscule. Throughout the years, fuel cells evolved to address these and other issues to become more efficient. In 1889, L. Mond and C. Langer utilized a three dimensional porous electrode and claimed the term "fuel cell" (Choi et al., 2006). Later, fuel cells took new forms and were used in variety of ways. For example, in 1965, United Technologies Corporation (UTC) produced an alkaline fuel cell to be used in the Apollo Lunar Mission.

Fuel cell science and technology embodies a variety of disciplines. Currently researchers are focused on better understanding all of the operating parameters that influence the fuel cell, especially its performance. In many cases, researchers have utilized mathematical models to help develop relationships between the fuel cell and its components (Wu et al., 2008a). Nevertheless, fuel cells are efficient, environmentally-friendly, alternative sources of energy with a few limitations that are holding them back.

2.1.2 Fuel Cell Working Principle

A fuel cell is an electrochemical device, i.e. a cell composed of four parts: anode, cathode, electrolyte (membrane) and external circuit. In a hydrogen fuel cell, hydrogen and oxygen combine to generate electricity and water as depicted in Equation (1).

$$2H_{2(g)} + O_{2(g)} \rightarrow 2H_2O + \text{energy (electrical power + heat)} \tag{1}$$

The reaction is similar to a combustion reaction, differing in that a fuel cell will produce electricity and heat energy (Larminie & Dicks, 2003).

To understand how reverse electrolysis works, reactions at each electrode are considered. Although these considerations vary for different types of fuel cells, an acid electrolyte fuel cell will be the base model as it is the simplest and most common (Figure 2). At the anode of an acid electrolyte, hydrogen gas enters the system and ionizes releasing electrons, thereby creating protons (H^+). As protons permeate through the electrolyte, electrons are forced through the external circuit and to the cathode. Oxygen entering at the cathode reacts with the electrons from the anode side. Hydrogen which has permeated through the electrolyte combines with oxygen at the cathode to form the by-product, water. Reactions at the anode and cathode are summarized in Equations (2) and (3).

$$\text{Anode: } 2H_2 \rightarrow 4H^+ + 4e^- \tag{2}$$

$$\text{Cathode: } O_2 + 4e^- + 4H^+ \rightarrow 2H_2O \tag{3}$$

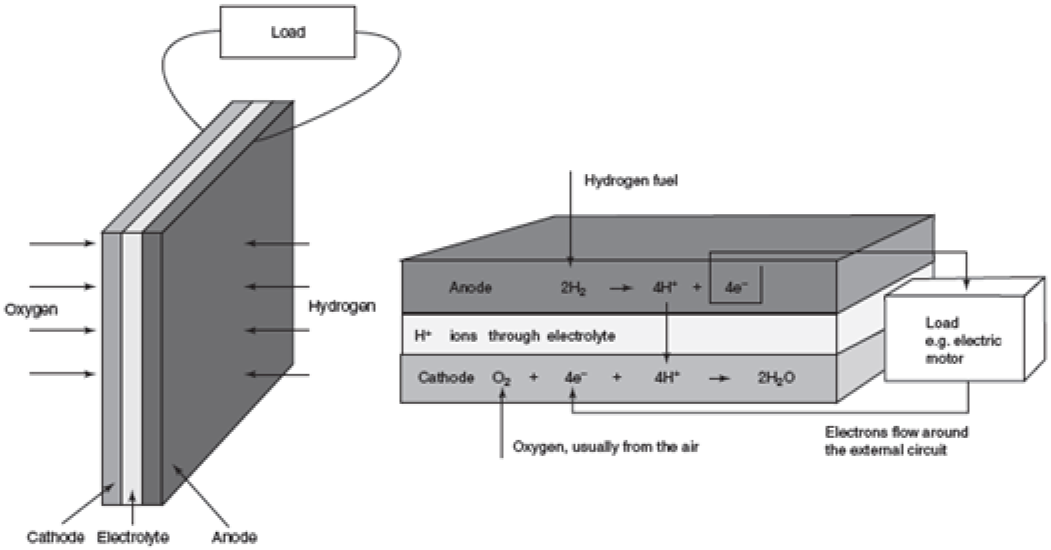

Figure 2 Basic construction of a fuel cell. For an acid electrolyte fuel cell, protons move from the anode to the cathode. Electrons circulate through a load. Water is produced at the cathode side. (Larminie & Dicks, 2003)

Although the acid electrolyte fuel cell is used here as a model, there exists many other types of fuel cells. Other types of fuel cells utilize different materials and mechanisms to effectively produce electricity.

2.1.3 Types of Fuel Cells

Fuel cells differ according to efficiency, applications, and cost. (Mekhielf et al., 2011) They are characterized by the type of electrolyte and fuel used into six major areas:

- Alkaline Fuel Cell (AFC)
- Proton Exchange Membrane Fuel Cell (PEMFC)
- Phosphoric Acid Fuel Cell (PAFC)
- Molten Carbonate Fuel Cell (MCFC)

- Solid Oxide Fuel Cell (SOFC)
- Direct Methanol Fuel Cell (DMFC)

Different types of fuels cells are designed to optimize the different strengths associated with fuel cells (Larminie & Dicks, 2003). For example, PEMFCs capitalize on specific operating parameters and physical design. The simple design incorporates a solid immobile polymer electrolyte. Due to its low operating temperature, PEMFCs utilizes platinum-based catalysts to address problems with slow reaction rates. Fueled by hydrogen, PEMFCs do not address the issue of the reliability of available hydrogen or hydrocarbon fuel. One solution to hydrogen supply is to use methanol, or other alcohols, as a fuel. For example, methanol is used as a fuel in DMFCs. Although there are many types of fuel cells, this project will focus on the PEMFCs, their properties and degradation.

2.2 Proton Exchange Membrane Fuel Cells

The proton exchange membrane fuel cell (PEMFC), also known as the solid polymer fuel cell was originally created for use in the Gemini manned space missions through collaboration between NASA and General Electric (Larminie & Dicks, 2003). Now, PEMFCs are utilized for electric production as portable electric generators for vehicles and power generation for electric devices or local grids. In this section, the functionality of PEMFC components is described.

2.2.1 Membrane Electrode Assembly (MEA)

PEM technology requires a very specific set of conditions and materials for the fuel to operate effectively. Similar to other fuel cells, a PEMFC is composed of four main components: bipolar plates, catalyst, gas diffusion layer and electrolyte; however, it is the fusion of electrolyte and catalyst that makes the PEMFC unique. This unit of PEMFCs, the membrane electrode assembly (MEA), drives the electrochemical reaction (Figure 3). The MEA is composed of three basic functional layers: the anode/cathode catalyst layers and the membrane.

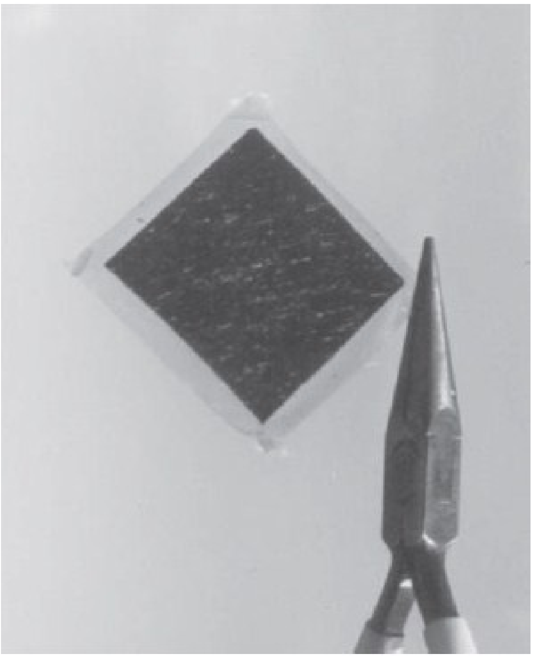

Figure 3 An example of a MEA. The MEA is composed of two main components- the catalyst later and the electrolyte. Typically a membrane is 0.05 to 0.1mm thick; the GDL is between 0.2 and 0.5 mm thick. (Larminie & Dicks, 2003)

One important aspect of the interaction between the PEMFC layers is the integration of the catalyst layer with the membrane. This interlock between the electrode and the membrane produces a charge double layer with opposing static charge (Larminie & Dicks, 2003). This charge double layer allows what is called three phase contact. Three-phase contact occurs at the boundary layer between the reactant gases, membrane layer, and catalyst as can be seen in Figure 4. This direct connection made by fusing the catalyst with electrolyte drastically increases the efficiency of a PEMFC.

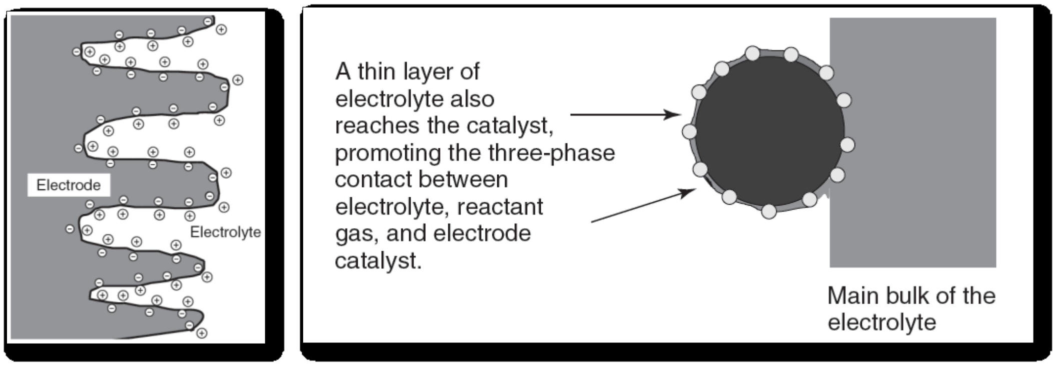

Figure 4 Three Phase Contact. Meshing the electrode and electrolyte promotes three-phase contact and hydrogen ion diffusivity. (Larminie & Dicks, 2003)

2.2.1.1 The Membrane Layer (Electrolyte)

As the name, p*roton exchange membrane* indicates, the technology is based on proton transport through a membrane, the electrolyte of a PEMFC. Protons must be able to readily and actively diffuse through the membrane, but should not conduct electrons, thereby allowing the current to flow from the anode to the cathode and create a potential difference. (Larminie & Dicks, 2003) The membrane should also be as thin as possible to minimize the proton transport resistance across the membrane by limiting hydrogen or oxygen crossover.

The requirements of the fuel cell membrane do not allow for much flexibility with the types of membranes that are presently available. In conjunction with NASA, DuPont™ developed a material named Nafion® that is still the primary membrane implemented in PEMFCs. (Larminie & Dicks, 2003) Nafion®, a Teflon® (tetrafluroethylene or PTFE) derivative, is hydrophobic, enabling it to drive water away from the electrodes. The Nafion® network is infused with sections of sulfonated side chains which in contrast to PTFE, are hydrophilic, and draw water towards them. This porous hydrophobic network with interspersed hydrophilic regions, allows for effective proton transport through a saturated membrane. The sulfonated side chains draw protons towards them (seen in Figure 5), but because of the network of hydrophobic

Teflon, the weaker intermolecular attraction is overcome and protons are driven through the membrane.

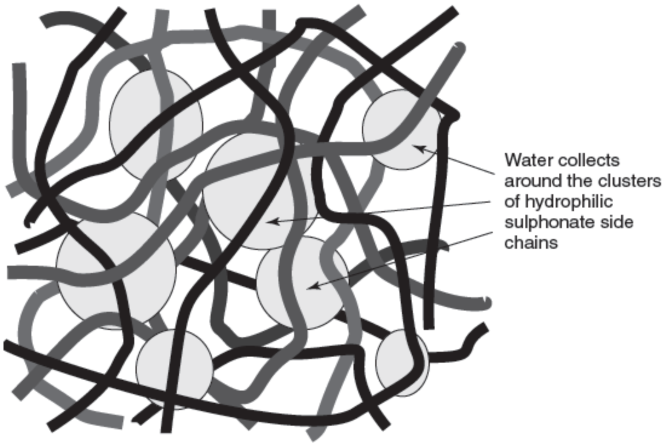

Figure 5 Macro-scale Perfluorosulfonic Acid Membrane (PFSA). As water molecules travel through the PFSA membrane, they are attracted to the hydrophilic sulphonate side chains as depicted in the illustration. (Larminie & Dicks, 2003)

Other perfluorosulfonic acid membranes have been developed under similar principles like Gore-Select® and Primea® (made by Gore™), Aciplex® and Flemion® (made by Asahi™). (Wu et al., 2008b)

Nafion® is still widely used as an industry standard for PEMFCs because of its distinctive properties. Although new membranes have been developed, they are mostly variants of the Nafion® membrane, having similar properties due to the hydrophobic and hydrophilic characteristics generated by perfluorination and sulfonation. Other properties that make Nafion® and fluorosulfonate ionomers unique are that they are more durable and resistant to chemical degradation and can be formed into thin membranes without jeopardizing mechanical integrity. (Wu et al., 2008b)

In addition to membrane material, water management and relative humidity are other parameters vital to maintain operation of a PEMFC. The water content of a PEMFC has a direct relationship with the proton transport through the membrane, so the more saturated the cell, the better the cell operates. (Larminie & Dicks, 2003) However, to have optimal conditions, a water balance must be maintained. If there is too much water, flooding will occur. By flooding the cell, pores and sites at the three-phase interface are blocked, hindering mass transfer of the reactant to the electrode. The result of limited mass transfer within the cell is a decrease in fuel cell efficiency.

In an ideal situation, the water generated by the desirable redox reactions in the PEMFC at the cathode would provide all the water that would be necessary to sustain operation by keeping the membrane hydrated. The membrane would be thin enough for the water to diffuse back through the membrane towards the anode. Water at the cathode that would come in contact with the air would evaporate readily and the fuel cell would be able to run at steady state without any supplementary procedures. There are a number of complications that do not permit this sort of idealization to occur, like the divergent theories on low or high humidification strategies.

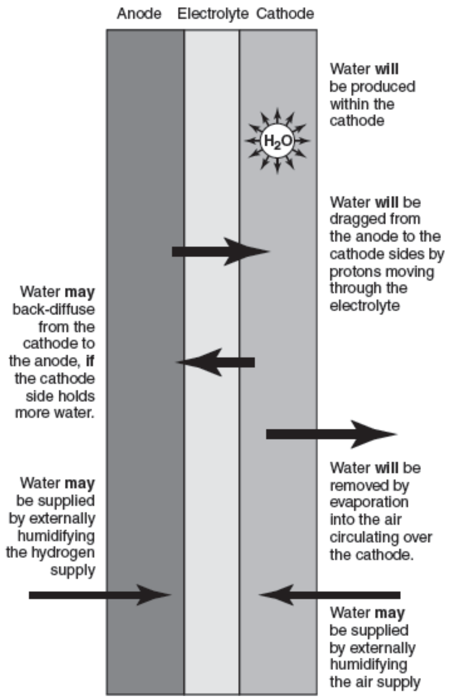

Figure 6 Water flux between electrodes and membrane (Larminie & Dicks, 2003)

When hydrated protons travel through the membrane from the anode side to the cathode, they “drag” water molecules along through the membrane. For each proton, up to five water molecules can be transferred. This phenomenon is known as electro-osmotic drag. (Larminie & Dicks, 2003) Electro-osmotic drag can lead to the anode side drying out even though the cathode side is well saturated. The water distribution across the membrane also may not be uniform, with some regions receiving less water than other regions. An excess of water can cause localized flooding at the electrodes. All of these setbacks are predictable and can be combated with solutions. Water drag and water generation are directly proportional to current and back diffusion changes with the thickness of the membrane, so water saturation can be predicted across the membrane and solved by adding humidity to the reactant gases.

2.2.1.2 The Catalyst Layer

The development of catalysts and catalyst efficiency has vastly improved in the last century. In history of the PEMFC, the most effective catalyst is platinum. (Larminie & Dicks, 2003) Platinum is a precious, expensive metal, but does not substantially contribute to the cost of a fuel cell because only a small amount of platinum is needed. For example, in the 1960s, 28 mg of catalyst were required per square centimeter of electrode; now, the electrodes are plated with 0.2 mg-cm^{-2} or less.

Carbon powder is used as a support platform for the platinum particles. Dispersing these platinum particles across the carbon powder increases the surface contact area of the catalyst layer, increasing the effectiveness of the redox reactions that take place (Schiraldi, 2006).

2.2.2 The Gas Diffusion Layer (GDL)

The essential function of the gas diffusion layer (GDL) is to disperse the reactant gases evenly to the corresponding electrode. (Schiraldi, 2006) It is in place to facilitate water management within the cell by 1) expelling water from fuel cell to avoid catalyst flooding and 2) maintaining water within the cell to optimize proton transport. (Larminie & Dicks, 2003)

The appropriate material selection is crucial to achieve and maintain high efficiency, especially when size restrictions are imposed on the design. Carbon paper or carbon cloth is often used as the GDL as it has the ability to drive water out of the cell while providing a conductive layer for electron flow. Carbon paper is usually selected when the PEMFC must be small and thin in size, whereas carbon cloth is thicker (Larminie & Dicks, 2003). Carbon cloth will absorb more water, making PEMFC manufacturing easier due to fewer voids in the cell compared to carbon paper. However, because carbon cloth is thicker and more absorbent, it will also expand more into the bipolar plate channels where reactant gas may be restricted.

Some GDLs employ a stratified level of porosity that has been shown to deliver different results than uniformly porous GDLs. (SGL Technologies GmbH, 2012) These GDLs can have two layers with a microporous layer (MPL) on the catalyst side, and a macroporous layer on the opposing side, adjacent to the bipolar plate, seen in Figure 7. The difference in pore size increases efficiency and durability of a fuel cell by limiting exposure of contaminants and undesired reactants to the catalyst. The diffusion characteristics of the macroporous layer can be examined by Fick's 1st and 2nd laws of diffusion, while the microporous layer generally exhibits Knudsen diffusion.

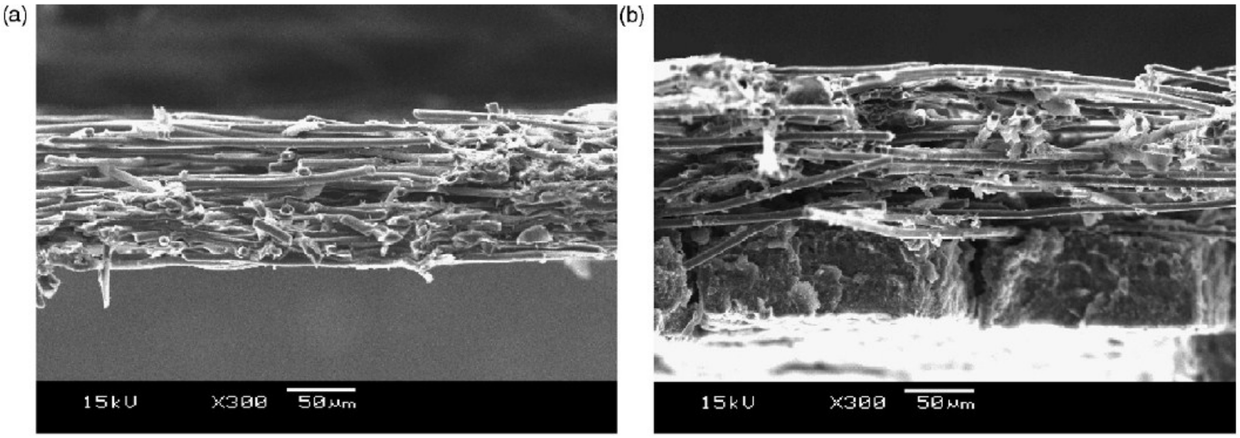

Figure 7 SEM GDL cross-section micrographs. a) In the single layer GDL a macroporous layer is shown, and b) in the dual-layer GDL, macroporous and microporous layers are shown. (Han et al., 2008)

2.2.3 Bipolar Plates and Flow Fields

The primary use of bipolar plates in PEM cells is to feed reactant gases to their appropriate electrodes. Plates are also used to connect multiple fuel cells in a stack to achieve voltages essential for various applications. Bipolar plates, usually made of graphite or steel, are grooved to channel the reactant gases through them. The use of graphite or steel facilitates the passage of electrons to the current collectors. (Baker & Zhang, 2011) The collections of conduits on bipolar plates that channel the reactant gases of the fuel cell are better known as flow field patterns. There are many different patterns for flow fields and research has not brought one unifying optimal design, but has elucidated efficient options for flow field patterns. (Larminie & Dicks, 2003) One study has tested multiple parameters of the flow fields by changing heights and widths of channels. (Wang et. al, 2006) In this experiment, the goal was to balance the manufacturing costs and performance of the bipolar plates. The geometry of five channels was varied in shape to promote convection and exchange between the layers of the MEA. The study concluded that flow fields can be optimized with diverging tapered channels that change the convection currents. By optimizing the channels at the inlet and outlet of each cell the efficiency of the cell could be increased.

Another important characteristic of bipolar plates that is directly related to the resistance of the plates is thickness. Increasing thickness of the plates contributes to larger voltage drop so the thickness of the plates should be minimized to improve the power to weight ratio. The optimization of these plates becomes more complicated when considering the high flow rates of air that are necessary to provide the appropriate amount of oxygen at the cathode for the oxygen reduction reaction (ORR). Ultimately, there is a trade-off between electrical conductivity and reactant flow rate that must be balanced in the design of these plates and the overall design of the fuel cells. The bipolar plates can be integrated within a PEMFC with individual cells connected with one bipolar plate, thus reducing the number of interconnects.

2.3 Fuel Cell Degradation

PEMFCs are remarkable energy conversion devices that have high energy densities in comparison to cells of similar size. For the technology to be effective, PEMFCs need to be able to withstand the stresses of the environments and loads that are imposed on them. The durability of PEMFCs is necessary for them to be viable products. In the mid-1990s, the PEMFC was expected to be commercially viable for stationary applications by 2001 and viable for transportation applications by 2003, but even today there are hurdles that are still present. (Wu et al., 2008b)

The DOE established a target for the cost of $61-per-kilowatt in 2009 ($51 per kilowatt in 2002 USD) to make fuel cells a competitive alternative in the market of portable cells for all types of power applications. (Spendelow & Marcinkoski, 2009) Since fuel cells are required to have lifetimes that vary from 5,000 to 40,000 hours, there are various methods to test the cells to simulate the operating conditions of their applications. (Wu et al., 2008b) Real-time testing for the lifespans of fuel cells would cost exorbitant amounts of capital, but similar stressed conditions can be reproduced by using accelerated testing techniques at much lower costs. Further, the results of steady state tests for fuel cells presented a much lesser change in average voltage drop per hour (when run for significantly less than 40,000 h) than accelerated stress tests (ASTs). (Wu et al., 2008b)

The components of PEMFCs degrade in different manners and the mechanisms involved in this degradation are not completely understood. The various mechanisms are related, so one degradation mechanism may trigger or exacerbate another. Noteworthy research has been performed in this realm with the purpose of uncovering the mechanisms involved in the degradation of PEMFCs. In this section, detailed degradation mechanisms of PEMFC components are presented.

2.3.1 Membrane Degradation

Membrane or electrolyte degradation is a severe form of deterioration that hinders PEMFC performance over time. PEMFCs degrade in manners mechanical, thermal, and chemical or electrochemical in nature. (Wu et al., 2008b) These degradation phenomena could be due to failures and defects in manufacturing processes of the MEAs, including the introduction of voids or foreign objects into the assembly, tears, pinholes, perforations or cracks. (Wu et al., 2008b) Thermal degradation can occur outside the cell's optimal operating range (60-80^{o}C) in extreme temperatures that the fuel cell could be subjected to in real world applications. Chemical and electrochemical degradation of PEMFC membranes can occur when an undesirable side reaction takes place in direct relation to hydrogen and oxygen crossover.

2.3.1.1 Mechanical Degradation

Mechanical degradation of membranes can specifically occur at the interfaces at which the channels formed in the flow field are pressed, causing tears. In addition, humidity plays a big role in the dimensional shrinking or swelling of the membrane, which adds to the pressure at these interfaces. (Wang, 2009) With increasing humidity, the membrane and gas diffusion layers take up more water and expand, increasing the overall dimensions of the PEMFC. The opposite occurs with decreasing humidity. Non-humidification, low humidification, and humidity cycling particularly impart intense mechanical stress upon the membrane and accelerate mechanical degradation. Also, when crossover occurs at pinholes near electrodes, a highly exothermic reaction can occur that may slowly spread through the membrane and cause catastrophic failure.

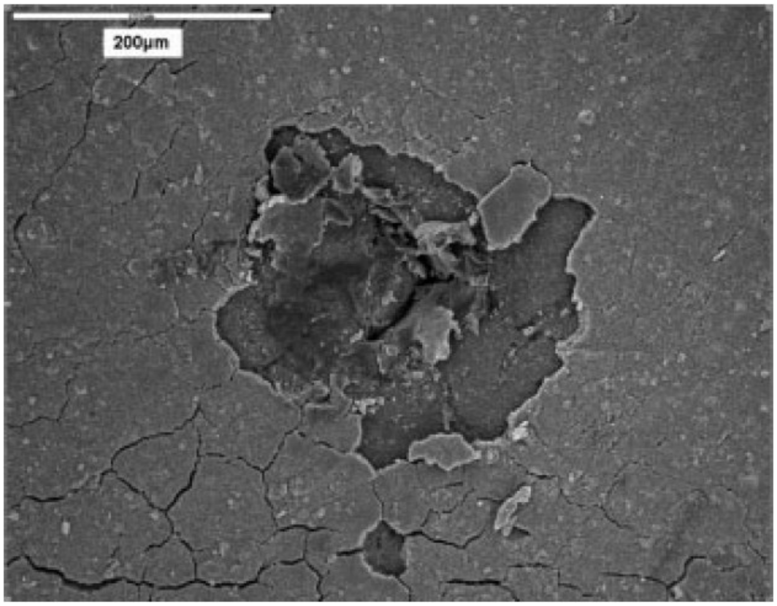

Figure 8 SEM image of a pinhole in an MEA. The localized damage of pinholes can lead to diminished performance and further, widespread degradation of a fuel cell with exothermic crossover reactions creating regions of increased temperatures. (Lu et al., 2011)

2.3.1.2 Thermal Degradation

Thermal degradation generally arises when PEMFCs are subjected to extreme temperatures, typically high temperatures. (Wu et al., 2008b) With the use of Nafion®, the membrane is thermodynamically stable because of the strength of the carbon-fluorine bond and the electronegativity of fluorine. Above 80°C, Nafion®'s glass-liquid transition will begin to alter the morphology of the membrane and the membrane will begin to chemically decompose in appreciable amounts in excess of 150°C. Beyond this point, Nafion®'s weaker sulphonic acid groups start to separate from the membrane. At even higher temperatures, covalent bonds in the membrane split between carbon and sulfur based radicals. Low temperatures also present a problem for the practicality of PEMFCs because of their reliance on water. Because of water's physical properties, studies have shown that water in the PEMFC tended to partially freeze within the membrane causing degradation.

Cycling between low and high temperatures proves to result in considerable degradation. (Wu et al., 2008b) A study evaluating thermal cycling on a PEMFC was performed by Giner Inc. and General Motors. In this study, repeated cycling was performed 385 times between -40°C and 80°C for two hour stints at each extreme over the course of three months. (McDonald & Mittelsteadt, 2004) Severe changes in ionic conductivity, gas impermeability, and impaired mechanical strength of the membranes were observed; however, no catastrophic failures occurred.

2.3.1.3 Chemical Degradation

Chemical and electrochemical degradation occur when a perfluorosulfonic acid membrane, such as Nafion®, decomposes due to undesired side reactions. Researchers have sought out to solve the problem involved with the membrane by understanding the mechanisms involved in degradation. It is believed that hydroxide and hydroperoxide radicals (·OH and ·OOH) form at the cathode surface causing chemical attack on the membrane electrolyte and catalyst. The studies performed have indicated that radicals do indeed form, but whether the source of the free radicals is the cathode, anode or both is still uncertain. Chemical degradation mechanisms detailed in this section are weak end group initiation, carboxylic acid end group unzipping and side chain cleavage.

The following mechanism has been proposed for when metals from the electrodes or bipolar plates corrode and enter the membrane. (Wu et al., 2008b) In this mechanism, the iron ion can be substituted with any divalent cation that could possibly contaminate the fuel cell.

$$\mathrm{H_2O_2 + Fe^{2+} \rightarrow \cdot OH + OH^- + Fe^{3+}} \tag{4}$$

$$\mathrm{\cdot OH + Fe^{2+} \rightarrow OH^- + Fe^{3+}} \tag{5}$$

$$\mathrm{\cdot OH + H_2O_2 \rightarrow \cdot HO_2 + H_2O} \tag{6}$$

$$\cdot HO_2 + Fe^{2+} \rightarrow HO_2^{\ -} + Fe^{3+} \tag{7}$$

$$Fe^{3+} + \cdot HO_2 \rightarrow H^+ + O_2 + Fe^{2+} \tag{8}$$

The peroxide and hydroperoxide radicals that are formed in this mechanism can proceed to attack the membrane layer of a PEMFC and cause catastrophic failure of the cell.

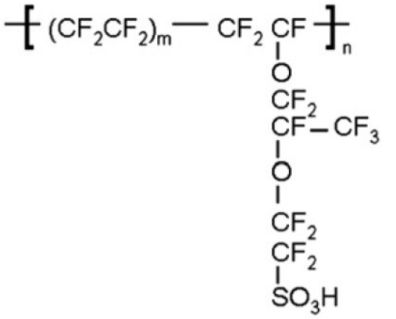

Figure 9 Structure of Nafion. The Teflon based backbone is shown with hydrophilic, sulphonic side chains. (Xie & Hayden, 2007)

Equations 9 - 11 represent the mechanism of the end group unzipping reaction at the Nafion backbone shown in Figure 9. (Xie & Hayden, 2007) The mechanism supports the general theory and experimental evidence that deterioration of the cell membrane will lead to fluoride leaving the membrane from the side chains and backbone, and eventually entering the water. This mechanism can be described as an unzipping reaction in which the electrolyte backbone is attacked and the functional fluoride units are broken off of the membrane. This mechanism can proceed in a chain reaction that continues until termination, at which point shorter, low molecular weight compounds are created**.** Equation 12 exemplifies the overall reaction of the mechanism, with a pair of hydroxyl radicals attacking the carboxylic end groups to remove a CF_2 group from the main chain and being incorporated into a carbon dioxide molecule and two hydrogen fluoride molecules.

$$\mathrm{R_f - CF_2COOH + \cdot OH \rightarrow R_f - CF_2 \cdot + CO_2 + H_2O} \tag{9}$$

$$\mathrm{R_f - CF_2 \cdot \ + \ \cdot OH \rightarrow R_f - CF_2OH \rightarrow R_f - COF + HF} \tag{10}$$

$$\mathrm{R_f - COF + H_2O \rightarrow R_f - COOH + HF} \tag{11}$$

$$\therefore \mathrm{R_f - CF_2COOH + 2 \cdot OH \rightarrow R_f - COOH + CO_2 + 2HF} \tag{12}$$

In addition to the primary degradation mechanism via end group unzipping, there is a secondary reaction that is not negligible and must be accounted for. (Wu et al., 2008b) The mechanism formulated for the secondary degradation is shown below in Figure 10. The figure demonstrates how the mechanism cleaves along the main chain between the side chains of the polymer backbone. Once a portion of the main chain is cleaved, the reaction continues according to the primary mechanism outlined in Equation 9-12 until a termination reaction occurs.

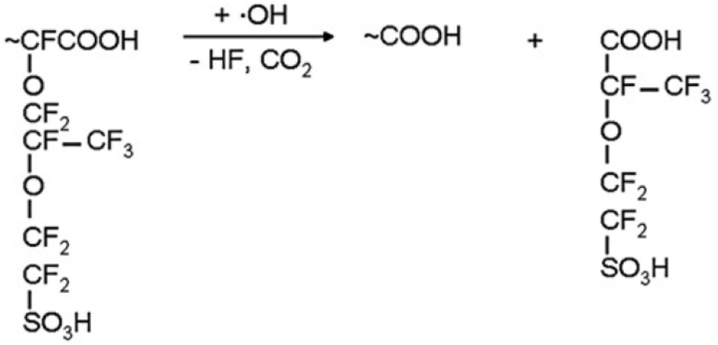

Figure 10 Secondary degradation reaction via end group unzipping. (Xie & Hayden, 2007)

The molecular product, $\mathrm{HOOC\text{-}CF(CF_3)\text{-}O\text{-}CF_2CF_2\text{-}SO_3H}$, of the reaction illustrated in Figure 10 is small enough to diffuse through the polymer membrane and block sites for hydrogen ions to flow through. (Xie & Hayden, 2007) This molecule can undergo further unzipping as shown in Figure 11, in which ultimately leads to the formation of carbon dioxide, hydrogen fluoride and sulfate ions.

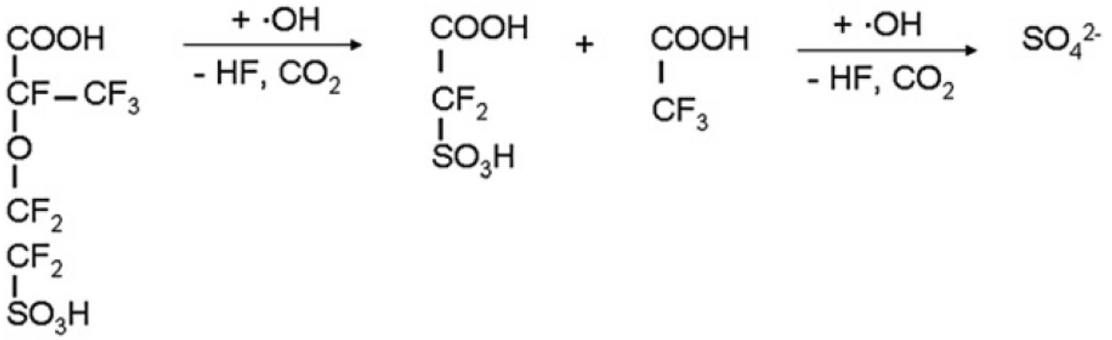

Figure 11 Unzipping progression of product of secondary degradation reaction. (Xie & Hayden, 2007)

Another proposed mechanism for radical formation is initiated by side chain cleavage in which the carboxylic acid groups of the side chains undergo the unzipping reaction. (Xie & Hayden, 2007) An attacking species, X, cleaves the side chain at an unknown linkage and unzips just like in the primary degradation. The side chain cleavage in this reaction continues until junction between the side chain and main chain exists, where the main chain is cleaved and carboxylic acid groups form on the ends of the chain. This reaction is illustrated Figure 12.

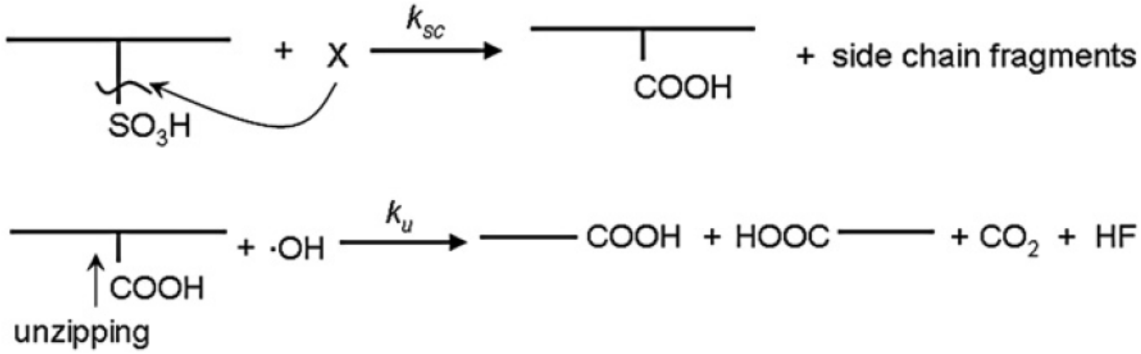

Figure 12 Initiation of degradation via side chain cleavage. (Xie & Hayden, 2007)

In addition, the presence of hydrogen can lead to the reaction shown below in which hydrogen ions attack the carbon atoms of a PTFE chain and displaces fluorine. (Wu et al., 2008b)

$$-\mathrm{CF_2}- + 2\,\mathrm{H_2} \rightarrow -\mathrm{CH_2}- +2\mathrm{HF} \tag{13}$$

Other chemical interactions exist if there is a presence of cations in the membrane that contaminate the fuel cell. (Wu et al., 2008b) Besides the increased chance of corrosion for the fuel cell assembly, cations can reduce the performance of the cell by taking the place of protons in the membrane layer of the fuel cell. This has a directly proportional relationship to ionic conductivity and water uptake. Only 5% of sulphonic acid sites need to be contaminated for water flux to be impacted, potentially drying out regions in the membrane near the anode.

2.3.2 Catalyst Layer Degradation

Platinum is a rare earth metal that is extremely valuable and expensive. (Baker & Zhang, 2011) The effectiveness of platinum as a catalyst for PEMFCs has been proven through much research and discovery. Platinum catalysts are potent alone or accompanied by other metals, like cobalt, chromium, nickel, ruthenium, iridium and tin in several combinations as alloyed compounds. The durability of platinum-based catalysts, however, has not been demonstrated bearing in mind the humidity, low pH, high temperatures, and redox chemistry that they may be subject to.

Degradation of the platinum catalyst layer may stem a wide variety of sources. Faults in platinum refinery before even being implemented in a fuel cell may cause issues that proliferate upon operation of the fuel cell. (Dhaunshkodi, 2010) Reactant gases may also introduce impurities that reduce contact area. Platinum particles may drift on the carbon support surface and aggregate or sinter to decrease surface area, dissolve into the electrolyte or also lose activity due to galvanic corrosion of the carbon support.

There has been no unified agreement on the mechanisms that are involved in catalyst layer degradation, though several have been proposed. A mechanism called Ostwald ripening suggests that platinum particles dissolve into the ionomer phase and precipitate on larger particles that lead to particle agglomeration. (Wu et al., 2008b) The dissolved platinum particles could also flow into the membrane and precipitate within the membrane, causing losses in membrane proton conductivity. Another suggested mechanism is that agglomeration occurs in a normal-log distribution of particle size. Based on particle collision kinetics, the mechanism suggests that even if platinum particles are uniformly distributed when initially manufactured, kinetics will drive particles together. Eventually, the distribution will have agglomeration regions of platinum particles. Another similar mechanism is also based on a normal distribution, except it is based on Gibb's free energy minimization instead of kinetic energy.

Oxide formation at the electrodes has also been attributed to increased platinum particle size as well as reduces active surface area, ultimately decreasing catalytic activity. Carbon corrosion has also been a major contributor to the gradual decline of PEMFC performance of the lifespan of the fuel cell. Power cycling and hydrogen fuel starvation due to pore blockage at the anode in conjunction with voltage cycling are the two modes believed to contribute to carbon corrosion.

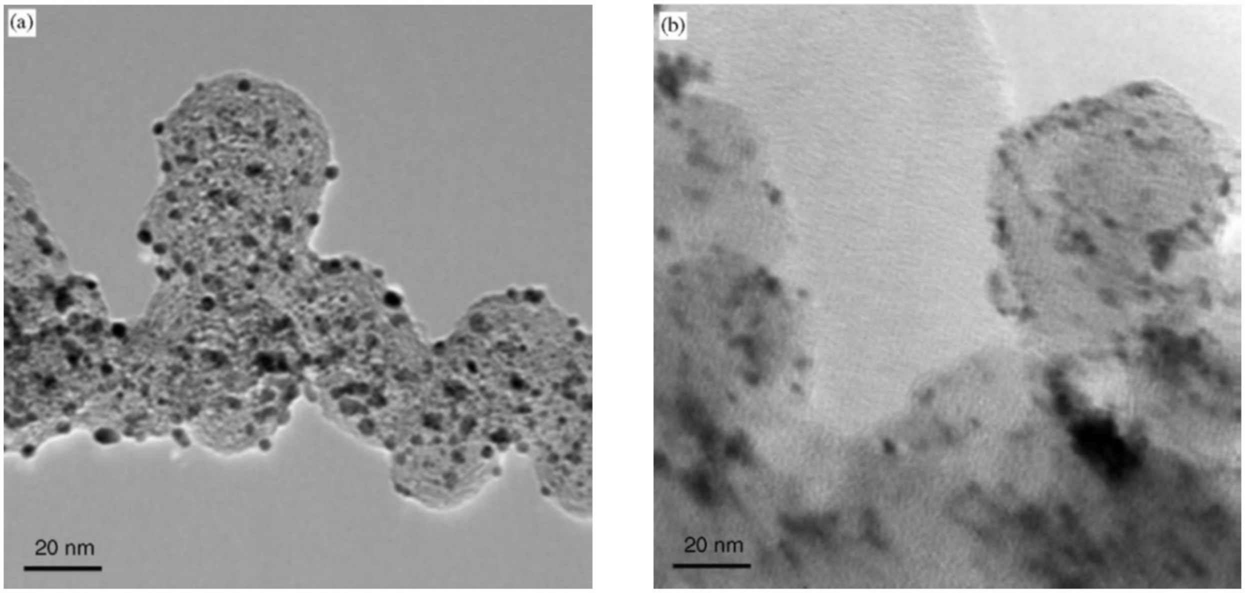

Figure 13 Platinum Catalyst Degradation. a) A TEM micrograph of an original platinum catalyst (black) on carbon support can be seen as well as b) a TEM micrograph degraded catalyst. The operation of the PEMFC has caused agglomeration of platinum particles, a decrease in platinum content, in addition to a morphological change in the carbon support. (Luo et al., 2006)

Power cycling of a PEMFC, or startup and shutdown cycling, creates an uneven supply of reactant gases, with hydrogen at the anode and oxygen in air crossing over towards the anode. Fuel starvation may be the result of uneven sharing of react flow between the cells in a stack or due to ice formation at freezing temperatures. Carbon and water oxidation will occur when hydrogen blocks the pores and its supply is exhausted from the local region of the catalyst layer with the follow reactions:

$$2\,H_2O \leftrightarrow O_2 + 4H^+ + 4e^- \tag{14}$$

$$C + 2\,H_2O \rightarrow CO_2 + 4H^+ + 4e^- \tag{15}$$

Thermodynamically feasible from 0.67 V, carbon oxidation does not happen occur readily, but platinum and platinum-ruthenium catalysts on carbon support have been shown to reduce the carbon oxidation potential from the usual 1.1 V_{RHE} to 0.55 V_{RHE} increasing the frequency of oxidation.

2.3.3 Gas Diffusion Layer (GDL) Degradation

Gas diffusion layers are critical components for mass transport within the fuel cell (Zhang et al., 2007). Although some studies have discussed the morphology of the GDL and the influence of pore size distribution on mass transport, only a limited amount of studies have focused on degradation of the gas diffusion layer and its effect on fuel cell performance (Wu et al., 2008b). Through understanding GDL degradation, fuel cell durability can be improved.

Through each degradation mechanism, the fuel cell will decrease in efficiency. Some studies demonstrated that GDLs are susceptible to chemical attack and electrochemical oxidation. (Wu et al., 2008b) Such losses decrease GDL conductivity and hydrophobicity which further lowers MEA performance. Corrosion on the GDL will increase resistance and decrease electrical output or conductivity. Some other areas where GDLs are vulnerable are degradation of baking material and decreased water management from mechanical stress. In study conducted by Borup, a decrease in hydrophobicity can also be due to an increased operating temperature and the use of sparing air instead of nitrogen (Wu et al., 2008b).

Because each degrading point negatively affects the durability of the entire cell, more studies must be conducted on the GDL. Quantitative correlations between performance loss and changes in GDL properties will give better understanding on fuel cell durability.

2.3.4 Bipolar Plate Degradation

The bipolar plates are used to connect PEM cells with one another, keep reactant gases and utility cooling or heating supplies apart, conduct current and distribute reactant gases across the MEA. These multipurpose plates are susceptible to degradation, primarily in the form of corrosion. Corrosion of bipolar plates can be largely detrimental to PEMFC function. As indicated by the mechanism in Equations 4-8, corrosion leading to foreign cations entering the MEA will take up sites that water and protons will normally exist in.

The manufacturing and production of the bipolar plates for PEMFCs is very important to prevent contamination of the cells, so the material selection and design of the flow fields must be considered in a concerted effort. The material implemented in bipolar plates must have excellent electrical and heat conductivity while the gas permeability must be very low. Strong corrosion resistance and mechanical strength is required, since the plates will be constantly exposed to oxygen, hydrogen, water vapor and an acidic electrolyte. (Larminie & Dicks, 2003) On top of these conditions, the weight, volume and costs must also be minimized. The two main classes of materials that are used are metal and carbon. Graphite based plates the meet the conductivity requirements of PEMFCs, but their advantages are counteracted by their porous and brittle nature and vulnerability to shock and vibration which forces the plate designs to be thick and heavy.

Metals can also be used for bipolar plates, and are conductive and dense so they can be very thin. Common noble metals like platinum, tantalum, niobium, and zirconium have great properties for bipolar plate production, except the raw material cost of these metals is very high. (Wu et al., 2008b) Metals are not without disadvantages, however, understanding that the most feasible metals used for production are either susceptible to oxidation or corrosion. Titanium and aluminum are also effective metals and metal alloys that are much cheaper than noble metals. Nevertheless, these two metals are likely to form oxide layers between the plates and the gas diffusion layer which significantly increases contact resistance. Steel is another metal considered in production; however, it is also susceptible to galvanic corrosion. While coatings can be applied to metals, the production time and costs increase.

It turns out that most of the bipolar plate manufacturers are split on these technologies, as both types of plates are produced for use in fuel cells. Both metal and carbon based bipolar plates are used and introduce various contaminants into the reactant streams as the metals and carbon are oxidized. These metal and carbon contaminants cause degradation at the catalyst and membrane as stated in their respective sections.

2.4 Diagnostic Tools for Experimental Methodology

Due to their low emissions, high efficiency and power density, PEM fuel cells are a promising alternative energy source; however, several challenges still remain. To address these challenges, intensive research and development is needed. To aid in R&D, fuel cell testing and diagnostic tools have become vital in performance optimization, design validation and development of a fundamental understanding of fuel cell operation (Yuan et al., 2010). The diagnostic tools used and discussed in this report are electrochemical impedance spectroscopy (EIS), water management analysis, and the polarization curve.

2.4.1 Electrochemical Impedance Spectroscopy (EIS)

Regarded by scientists as a powerful technique, electrochemical impedance spectroscopy (EIS) is used to investigate physical phenomena and essential loss factors occurring within a fuel cell. By analyzing performance losses, the influence of operating parameters on the overall response can be determined (Zhang et al., 2007). In PEM studies, the uses of EIS technique includes: (a) to obtain electrochemical parameters through the development of an equivalent circuit (EC); (b) to assist in determining problems within the fuel cell by differentiating resistances at individual fuel cell components; (c) to provide microscopic information about the fuel cell to aid in structure optimization and selection of operating conditions. Other uses in PEM include the differentiation of components such as the GDL to overall fuel cell performance, and the identification of individual contribution to the total impedance such as charge transfer and mass transfer (Zhang et al;, 2007)

In a fuel cell, the electrochemical reactions consist of an electron transfer at the electrode surface (Yuan et al., 2010). Through the system, these reactions cause resistances, mainly membrane resistance (ohmic resistance), and charge transfer and mass transfer resistance at the electrode surface. Ohmic resistance (R_{Ω}) is an intrinsic characteristic and can increase due to membrane drying, contamination and thermal degradation. It is mainly due to internal resistance of the fuel cell including electrolyte, catalyst and contact resistance. The charge transfer resistances (R_{ct}), for both the anode and cathode, refer to the barrier through which the electron passes across the electrode surface. This resistance is then related to electrode potential or overpotential. Mass transfer by diffusion refers to the transfer of H_2 and O_2 to the electrode surface. Through EIS, reaction resistances can be represented as an electrical circuit as seen in Figure 14. The circuit includes electrolyte resistance or ohmic resistance, charge transfer resistance, double layer capacitance and mass transfer or diffusion resistance at both the anode and the cathode.

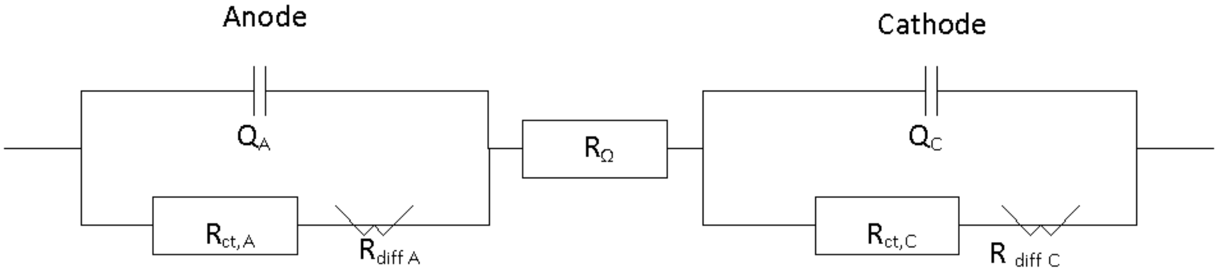

Figure 14 Equivalent circuit to PEM fuel cell. R_{Ω} is ohmic resistance. Rct is charge transfer resistance, and Ws is mass transfer or Warburg impedance. CPE is the capacitance relative to double layer charge at the interface of the fuel cell.

The general PEM circuit depicts resistances involved at both the anode and the cathode. However, due to the slow oxygen reduction reaction and the fast hydrogen reduction reaction, the diffusion resistance of the fuel cell nearly equals that of the cathode (Wu et al., 2008a). The anode side of the circuit of a PEM fuel cell is then reduced to only include the capacitance and charge transfer resistance.

In EIS, a small AC current as a perturbation signal varying between 10 kHz to 100 mHz is applied to the cell in addition to a steady current (Wu et al., 2008a). When this is done, a measurement of the frequency dependence of fuel cell is obtained through the resulting potential response. With this technique, known as Galvanostatic mode (GEIS), the current through the cell is precisely controlled. By using GEIS in combination with an interpretation of the spectra, resistances from each component in the electrical circuit can be extracted. Conventionally, impedance spectra are plotted on both Bode and Nyquist plots (Wu et al., 2008a). Impedance is made up of both imaginary and real parts. In the Bode plot, the impedance is illustrated as the amplitude and phase of impedance versus frequency. In the Nyquist plot, the opposite plot is graphed against the real part of impedance (Z' vs. Z"). Figure 15 illustrates a traditional Nyquist plot with two arcs as frequency decreases from left to right.

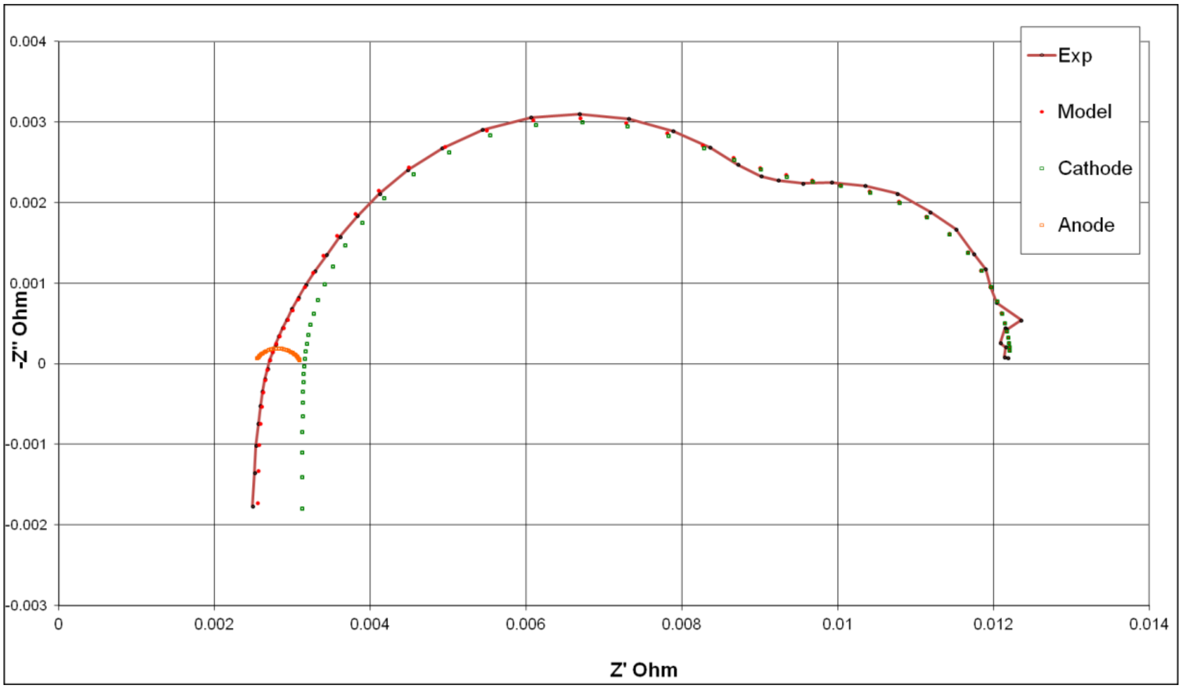

Figure 15 Nyquist plot. A mathematical model is fitted to experimental data to obtain resistance values. From the plot, a high frequency and low frequency arc are displayed. The distance from the origin to where the spectra cross the x-axis is the ohmic resistance.

From the plot, three areas where resistances occur can be identified: high frequency resistance (ohmic resistance), high frequency arc, low frequency arc. Each of these areas relate to resistance due to the electrolyte (ohmic), charge transfer and mass transfer respectfully.

In the Nyquist plot, ohmic resistance is illustrated as the distance from the origin to the point in which the spectra cross the x-axis as seen in Figure 15. Cathode resistance can be split into two sections, the high frequency arc and low frequency arc. The high frequency arc is related to the charge transfer resistance (R_{ct}). The low frequency arc is due to mass transfer or diffusion resistance and can be expressed as Warburg impedance (Zhang et al., 2007.)

From data collected in the GEIS, model fitting can be conducted to identify quantitative parameters representing resistances as well as electrode capacitance. The fitting process is conducted by minimizing the difference between experimental data and the model. By analyzing resistance values over time, information on operation conditions and aging/degradation can be obtained.

EIS provides detail information on operations within the fuel cell. With EIS, measurements can be conducted under real-world conditions i.e. open circuit voltage or under load (Scribner Associates, 2011). From this single experiment, multiple parameters can be determined and analyzed with relatively simple measurements. Other advantages to this diagnostic tool are EIS measurements are high precision and non-invasive.

2.4.2 Water Management

Analysis on the water produced by a fuel cell is used to understand dynamics and degradation. Water flow within the cell can be analyzed by the following parameter:

$$\alpha = \frac{F^{A}_{H_2O,out} - F^{A}_{H_2O,in}}{(F^{A}_{H_2O,out} - F^{A}_{H_2O,in}) - (F^{C}_{H_2O,out} - F^{C}_{H_2O,in})} \qquad (16)$$

where F^A is the molar flow rate of water in the anode and similarly for the cathode. For all experiments conducted, no water was introduced at the anode or $F^A_{H_2O,in} = 0$. Equation 17 is then simplified to

$$\alpha = \frac{F^A_{H_2O,out}}{F_{H_2O,produced}} \tag{17}$$

Typically, α is greater than zero meaning that the net flow of water is from cathode to anode. If the water transport coefficient is zero, there is not net flow and the flow of electro-osmosis is equal but opposite. Finally if α is less than zero, water flow is from anode to cathode. This can occur when water is introduced into the anode side.

2.4.3 Polarization Curve

The standard electrochemical technique used to characterize the performance of fuel cells is the polarization curve. Polarization signifies that an electrochemical reaction takes place as the potential of the electrode surface shifts away from its equilibrium point (Yuan et al., 2010). A polarization curve is essentially a plot of cell voltage against current density under a set of constant operating conditions (Wu et al., 2008a). By constructing a polarization curve, the effects of varying operating conditions such as temperature, composition, and relative humidity can be systematically analyzed.

The ideal polarization curve has three major regions as shown in Figure 16**.** At low current densities, or at activation polarization, the cell potential drops exponentially (Wu et al., 2008a). Losses are due to the slow oxidation reduction reaction and become more significant as the catalyst layer degrades (Choi & Moss, 2009). The next region, ohmic polarization, is encountered at intermediate current densities. Potential losses that occur are due to ohmic resistance or the resistance due to the flow of ions in the electrolyte and the flow of electrons through the electrode. Here, the ohmic resistance contributes the most to the potential drop which is essentially linear. Finally, at high current densities, concentration polarization occurs. Due to the limit of the reactant gas through the GDL, and electrocatalyst layer, cell performance drops significantly. Such losses can be amplified through improper water management or impure gas feeds.

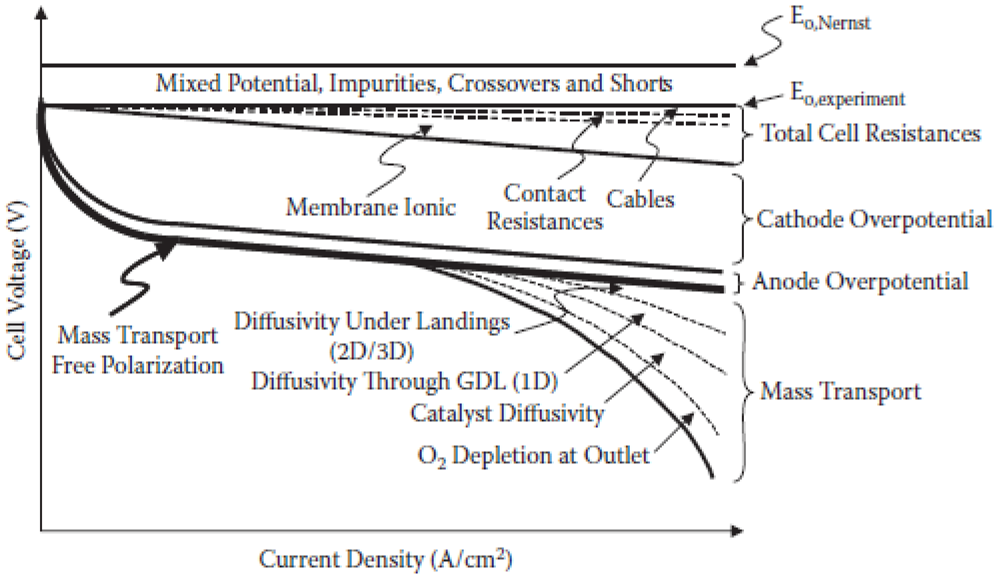

Figure 16 Polarization Curve. In the ideal curve, three regions of resistance are shown. (Dhaunshkodi, 2010)

Not only can the polarization curve directly characterize the performance of fuel cells, it can also be used as a modeling tool to predict how a fuel cell will act. Through modeling, theoretical performance can be compared to experimental results and analyzed.

2.4.3.1 Theoretical Modeling

Mathematical modeling is a useful tool used to predict the performance of a fuel cell. By utilizing theoretical models, operating conditions can be optimized. Although theoretical modeling is a useful tool, it can be challenging due to numerous design parameters and the complexity of a fuel cell itself. Through modeling, the importance of each parameter and its influence on fuel cell performance can be evaluated.

First, to understand correlations from the polarization curve to experimental data, it is vital to investigate the electrochemical parameters. Two significant parameters indicated in the polarization curve are overpotential, η and exchange current density, i_o (Yuan et al., 2010). Overpotential is the difference between the applied potential and the thermodynamic potential, typically 1.229 V for a PEM fuel cell at 25℃. The relationship demonstrates that the higher the current, the higher the overpotential. On the other hand, exchange current density is a kinetic parameter depending on the active electrode surface area that the electrochemical reaction occurs on. In general, the magnitude of i_o determines how easily the reaction occurs on the electrode surface. Exchange current density is related to overpotential in that the smaller i_o is, the higher the overpotential.

The basic model used in the polarization curve is shown Figure 17. In the schematic, the overpotentials represent the five layers of a PEMFC as resistances.

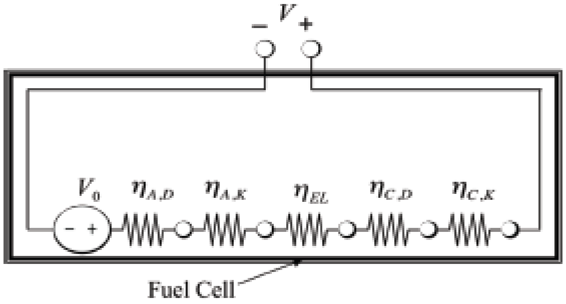

Figure 17 Electrical Circuit of a Fuel Cell. The internals include voltage source and resistances (Datta, 2012).

Mathematically, the model is described as:

$$V = V_0 + \eta_{A,D} + \eta_{A,K} - \eta_{c,D} + \eta_{c,K} + \eta_{EL} + \eta_I \tag{18}$$

where V_0 is the thermodynamic voltage and η is potential drop across each layer (Datta, 2012). Potential drop across the anode and cathode are characterized as diffusion (η_D) and electrode reaction over potential (η_K) which can be summed. Thus

$$V = V_0 + \eta_A - \eta_c + \eta_{EL} + \eta_I \tag{19}$$

The losses for the anode can then be written as:

$$\eta_A = \frac{RT}{\alpha_A^* \nu_{Ae-}^* F} \sinh^{-1}\left[\frac{1}{2}\left\{\frac{i/i_{A,0}}{1 - i/i_{A,L}}\right\}\right] \tag{20}$$

Likewise, the potential drop for the cathode is:

$$\eta_C = \frac{RT}{\alpha_C^* \nu_{Ce-}^* F} \sinh^{-1}\left[\frac{1}{2}\left\{\frac{(i + i_{C,x})/i_{C,0}}{1 - (i + i_{C,x})/i_{C,L}}\right\}\right] \tag{21}$$

where α^* is the transfer coefficient, ν_{e-} is the electron stoichiometric number and i_L is the limiting current density. Unlike the anode, overpotential at the cathode takes into account potential drop due to hydrogen crossover, $i_{C,x}$ (Vilekar & Datta, 2010). The cross over current density due to hydrogen flux, $i_{C,x}$, can be expressed as:

$$i_{C,x} = \frac{2Fk_H p_H}{L_{EL}} \tag{22}$$

where k_H is the permeability of hydrogen and L_{EL} is the membrane or electrolyte thickness. The exchange current density for both the anode and cathode can be calculated as:

$$i_0 = \gamma_m \left(\frac{p_i}{p_{i,ref}}\right) \exp\left\{-\frac{E_\Phi}{R}\left(\frac{1}{T} - \frac{1}{T_{ref}}\right)\right\} i_{0ref}^* \tag{23}$$

where p_i is the partial pressure of the species permeating at the electrode, E_Φ is the effective activation energy and γ_m is the roughness factor. The roughness factor is the ratio of electrochemically active metal catalyst surface area to the geometric MEA area and is given in terms of particle diameter by:

$$\gamma_m = \varphi_I m_M \frac{6}{\rho_M d_M} \tag{24}$$

where φ_I is the part of the metal diameter $d_M$which is accessible for reaction, m_M is the catalyst loading and ρ_M the catalyst density. From these relations, by increasing the roughness factor, temperature or concentration of the species, the exchange current density will be increased.

Next, over potential occurring at the electrolyte layer is calculated as

$$\eta_{EL} = i\left(\frac{L_{EL}}{\sigma_{EL}}\right) \tag{25}$$

Here, σ_{EL} is the protonic conductivity of the membrane (Vilekar & Datta, 2001). By combining the above equations, the theoretical fuel cell performance can be calculated as:

$$V = V_0 - \frac{RT}{\alpha_A^* \, \nu_{Ae-}^* F} \sinh^{-1}\left[\frac{1}{2}\left\{\frac{i_A/i_{A,0}}{1 - i_A/i_{A,L}}\right\}\right] + \frac{RT}{\alpha_C^* \, \nu_{Ce-}^* F} \sinh^{-1}\left[\frac{1}{2}\left\{\frac{(i_C + i_{C,x})/i_{C,0}}{1 - (i_C + i_{C,x})/i_{C,L}}\right\}\right]$$

$$- i_{EL}\left(\frac{L_{EL}}{\sigma_{EL}}\right) - i(Ri) \tag{26}$$

where $i(Ri)$ or (η_I) is described as the interfacial resistance between layers. This expression yields the cell voltage *V* versus current density *i.* Theoretically, in the absence of current, the voltage of the cell should equal to the thermodynamic or ideal voltage; however, due to the presence of side reactions, the voltage at zero current density is not equal to the thermodynamic potential (Vilekar & Datta, 2011). At zero current density, hydrogen crossover exists at the cathode; therefore, the cathode overpotential (η_C) is not equal to zero at zero current density. As current is drawn, the sum of potential drop across the fuel cell is registered. By changing characteristic parameters, the exchange current densities, roughness and limiting current densities, the effect on cell performance can be observed.

Although the polarization curve model provides adequate information on mechanisms within the cell, it is also useful to model the resistances within the cell at different operating conditions via impedance spectroscopy (Datta, 2012). By differentiation of the overpotentials in relation to current, charge transfer resistances at the anode and cathode can be determined. The resistance at the anode and cathode are then:

$$\mathrm{R_A} = \frac{\mathrm{RT}}{\left(2\alpha_{\mathrm{A}}^{*}\,\nu^{*}_{\mathrm{Ae-}}\mathrm{F}\mathrm{i}_{\mathrm{A,0}}\right)(1 - \mathrm{i}/\mathrm{i}_{\mathrm{A,L}})^{2}\sqrt{1 + \frac{1}{4}\left\{\frac{\mathrm{i}/\mathrm{i}_{\mathrm{A,0}}}{1 - \mathrm{i}/\mathrm{i}_{\mathrm{A,L}}}\right\}^{2}}} \tag{27}$$

and

$$\mathrm{R_C} = -\frac{\mathrm{RT}}{\left(2\alpha_{\mathrm{C}}^{*}\,\nu^{*}_{\mathrm{Ce-}}\mathrm{F}\mathrm{i}_{\mathrm{C,0}}\right)\left(1 - \frac{\mathrm{i} + \mathrm{i}_{\mathrm{CX}}}{\mathrm{i}_{\mathrm{CL}}}\right)^{2}\sqrt{1 + \frac{1}{4}\left\{\frac{(\mathrm{i} + \mathrm{i}_{\mathrm{CX}})/\mathrm{i}_{\mathrm{C,0}}}{1 - (\mathrm{i} + \mathrm{i}_{\mathrm{CX}})/\mathrm{i}_{\mathrm{C,L}}}\right\}^{2}}} \tag{28}$$

Through a similar analysis, the ohmic resistance or resistance in the electrolyte is derived as

$$\mathrm{R_{EL}} = \frac{\mathrm{L_{EL}}}{\sigma_{\mathrm{EL}}} \tag{29}$$

The calculated resistances can be compared to data extracted from EIS. The use of modeling by the polarization curve accompanied by resistance calculations provides a useful tool in predicting and interpreting fuel cell performance.

3.0 Methodology

The experiments presented in this report were executed at Ecole Nationale Supérieure des Industries Chimiques (ENSIC) in Nancy, France. Experiments were separated into three sections, aging of a three-cell healthy stack, degradation in a three-cell stack with a defect in the first cell, and basic polarization curve modeling. Experiments conducted on the three-cell stack fuel cell operated at nominal conditions over a period of four weeks. Over the course of four weeks, water and electrochemical impedance spectra were collected and analyzed from the cell. Experiments on the three-cell stack with a defect in the first cell occurred at the same operating conditions as the healthy stack. Finally, the polarization model was used to predict cell performance of a single cell. Resistances from the stack were also compared to results from the model. In this section, equipment used and experimental procedures are presented.

3.1 Aging in a Healthy Three-Cell Stack

The first part of this project analyzed aging in a three-cell at steady state conditions. The operation of the stack at nominal conditions occurred for a period of four weeks. Throughout the four weeks, data was collected and analyzed each day to evaluate aging and degradation patterns within the stack. This section describes the equipment used and procedures followed on experiments conducted on the healthy stack.

3.1.1 Equipment

Equipment used in this project consisted of a fuel cell bench and accompanying software. This section will describe the stack assembly, operating conditions and monitoring software used to conduct the experiment.

3.1.1.1 Fuel Cell Bench

A schematic and picture of the work bench are shown in Figure 18 and Figure 19 respectively. The fuel cell bench was comprised of a stack, evaporator, flow instruments and a pump. For the fuel cell system, pure hydrogen and air (21% oxygen) was supplied to the anode and cathode respectively.

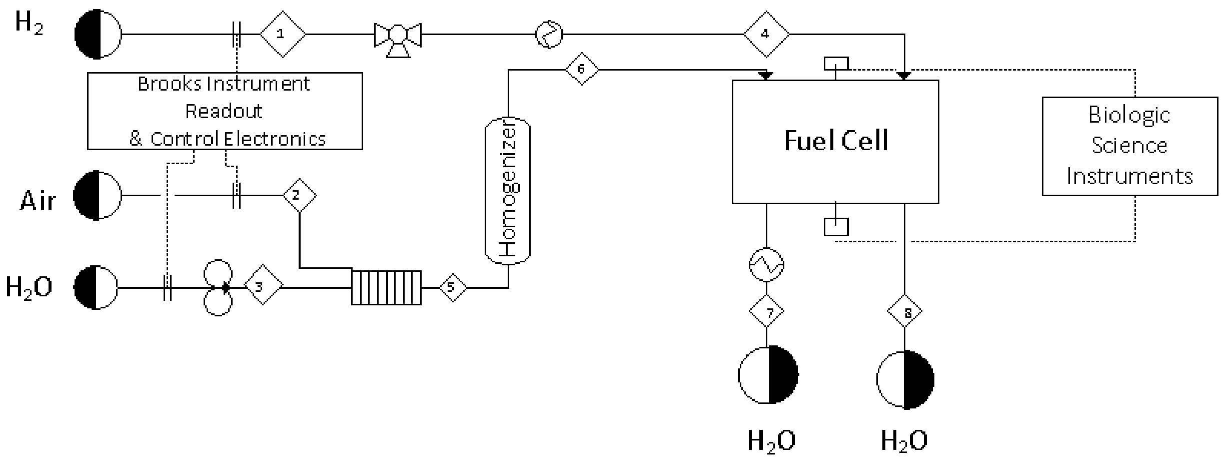

Figure 18 Experimental Schematic

1. Fuel Cell
2. Brooks Instrument: Flow Indicators
3. Humidified Air In
4. Dry Hydrogen In
5. Homogenizer
6. Temperature Control
7. Cathode: Effluent Water Out
8. Anode: Effluent Water Out
9. Cooling Water Temperature Control
10. Temperature Indicators
11. Biologic Science: EIS

Figure 19 Experimental Bench and Hood

Hydrogen and humidified air flow rates were determined based on Faraday's law of electrolysis. The law states that the quantity of a substance produced or consumed by electrolysis is directly proportional to the quantity of electricity used. To provide an excess amount of gas needed for the target current density (0.3 A/cm^2), the stoichiometric coefficient (λ) of hydrogen was set to 1.5 (50% excess); λ of oxygen was set to 3. At the anode, dry hydrogen gas entered the system at 0.94 L/min atone atmosphere, and 55°C. To ensure humidified air was flowing into the cathode, air at 4.48 L/min and deionized water at 0.38 g/min were mixed in an evaporator at 110°C. Figure 20 illustrates the heater configuration. Air flowed above the plate while water was heated through the channels. After contact with the heater, the water evaporated, mixing with air and forming a heterogeneous vapor mixture.

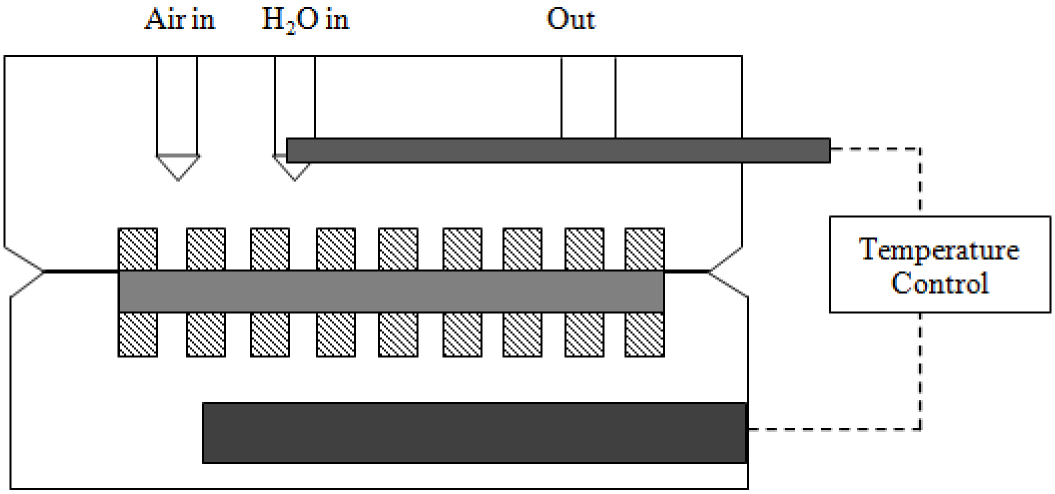

Figure 20 Water/Air Heater Configuration (Huang, 2012)

The flow rate of water corresponds to the amount of saturated water necessary to humidify the air adequately. The heterogeneous mixture was then introduced to a homogenizer to produce a homogenous vapor at 55°C and 62% relative humidity. At both the anode and cathode side, water exited and was retained in two large beakers. In order to guarantee the accuracy of the water balance at the cathode side, the outlet flow was first cooled in a condenser with cooling water supply at 3°C. The flow rate at the anode side was too small for vapor condensate to make an appreciable difference in the balance.

To maintain steady state conditions, fluid flow rates were monitored using Brooks Instrument Readout & Control Electronics; heaters were monitored using Huber Polystate CC3 Heater.

3.1.1.2 Stack Assembly

The fuel cell used for these experiments was composed of three healthy cells connected in series. Each cell was compiled of carbon paper (Sigracet® made by SGL Technologies) as the gas diffusion layer, a fresh MEA (PRIMEA® made by Gore) and two bipolar plates. The "carbon paper" itself was a bilayer with a macroporous side adjacent to the bipolar plate and flow field with a microporous side adjacent to the catalyst layer. The MEA was comprised of the electrolyte and catalyst layers. The electrolyte was an ePTFE enhanced perfluorosulfonic acid (PFSA) polymeric membrane. The catalyst on the anode side was 0.45 mg/cm^2 of a 50:50 mixture of platinum to ruthenium particles on carbon support and the cathode side was 0.40 mg/cm^2 of platinum on carbon support. The active area of each MEA per cell was 100 cm^2. The basic assembly is shown in Figure 21.

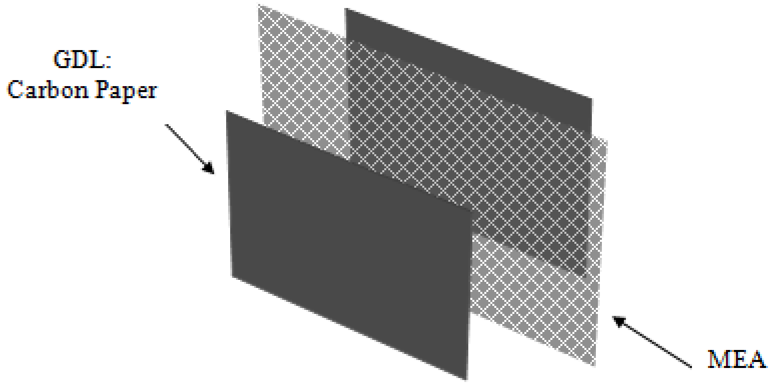

Figure 21 MEA and Carbon Paper Layers

The bipolar plate used at the end each cell is displayed in Figure 22. Figure 22 A illustrates the gas distribution to the fuel cell. This side of the plate faces towards the gas diffusion layer at both the anode and cathode sides. The Figure 22 B displays the reverse side of the bipolar plate. On this side, hot water is distributed evenly through the plate: the distribution of hot water is utilized to heat the cell and maintain a temperature of 55℃ .

Figure 22: (left) A) Bipolar Plate reactant distribution channels and (right) B) hot water distribution channels (UBzM, 2012)

The nominal conditions of the stack are summarized in Table 2.

Table 1 Nominal Operating Conditions.

Steady State Operating Conditions	
Temperature	55℃
Area (cm^2)	100
Current (A)	30
Current Density (A/cm^2)	0.3
Relative Humidity	
Anode	0%
Cathode	62%

The three cells are connected in series as shown in Figure 23, where dotted lines represent electrical connections used to measure the potential and impedance of each cell. Figure 24 displays the actual set up in the lab.

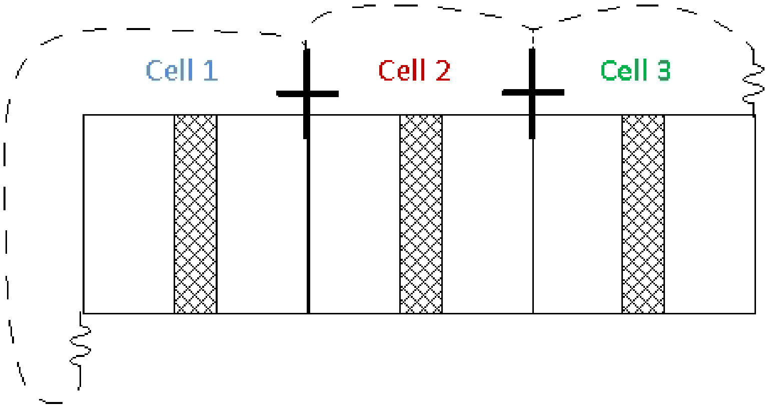

Figure 23 Cell to cell connections in stack

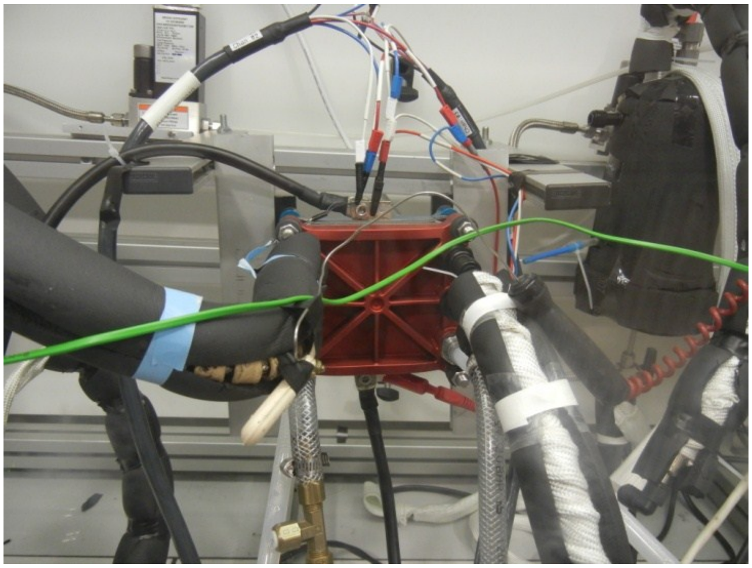

Figure 24 Fuel Cell Stack Apparatus

3.1.2 Experimental Procedures

3.1.2.1 Galvanostatic Electrochemical Impedance Spectroscopy

Every 24 hours, impedance data were collected and analyzed using EC-Lab© software. Electrochemical Impedance experiments were conducted by applying and AC current over a frequency range of 10 kHz to 100 mHz. Data were then collected and extracted from EC-Lab software. Impedance spectra in EC-Lab displayed Nyquist plots for the stack as well as for each individual cell. The exported data, 50 points per spectrum, were imported into Excel™ to be fitted to theoretical models following procedures previously developed in the lab. The following parameters were adjusted to the experimental model:

Table 2 EIS Modeling Parameters. These parameters demonstrate the resistances associated with the fuel cell stack. Resistances could then be compared and graphed to gain understanding of the aging processes within the stack.

Membrane & Connection		**Cathode**		**Anode**	
L	Inductance	R_c	Charge Transfer Resistance	R_a	Charge Transfer Resistance
R_{ohm}	Ohmic Resistance	Q_c	Pseudo Capacitance	Q_a	Pseudo Capacitance
		n_c	Constant	n_a	Constant
		$R_{d\ c}$	Diffusion Resistance	$R_{d\ a}$	Diffusion Resistance
		T_{dc}	Time Constant	$T_{d\ a}$	Time Constant

In order to approximate values of different resistances within the fuel cell, experimental data was fit to plots in Microsoft® Excel. The Excel model relied upon two impedance spectroscopies: the Bode diagram and Nyquist plot. A plot of the Nyquist diagram fitted to experimental data is shown in Figure 25. Above the plot is an equivalent circuit showing the effect regions.

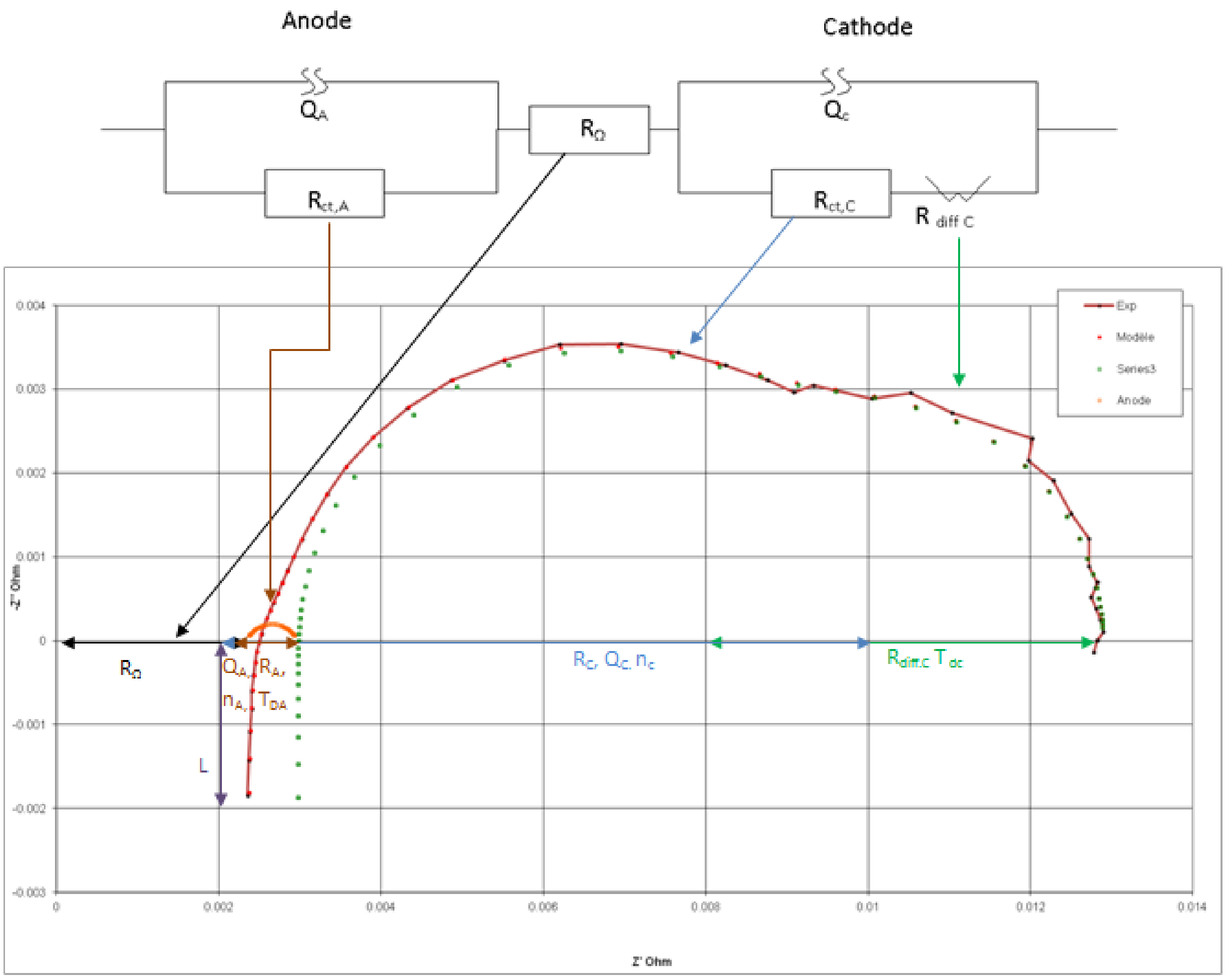

Figure 25 Experimental Nyquist Plot.

The model was first adjusted to fit the length of the plot by varying *L,* where *L* is the pseudo-inductance associated with the effects produced by connection points. Next, the ohmic resistance, R_Ω, was adjusted to fit the data to align the point where the graph intersected with the x-axis.

Later, the ohmic resistance and the charge transfer resistances were fitted to the model. This corresponded to the high frequency arc and incorporated R_Ω, R_c, Qc, n_c and $Q_{a.}$. Charge transfer resistance at the anode is small in comparison to the cathode and can therefore be fixed: at the anode R_a, is calculated to be 1/10 R_c.

After fitting charge the high frequency arc, the diffusion resistance or the low frequency arc was fitted to the model (R_{dc} and T_{dc}). The diffusion resistance at the anode was considered negligible and was set to zero. An overall fit of resistances was then conducted to appropriately fit both plots. Figure 26 shows examples of both plots fitted to the data.

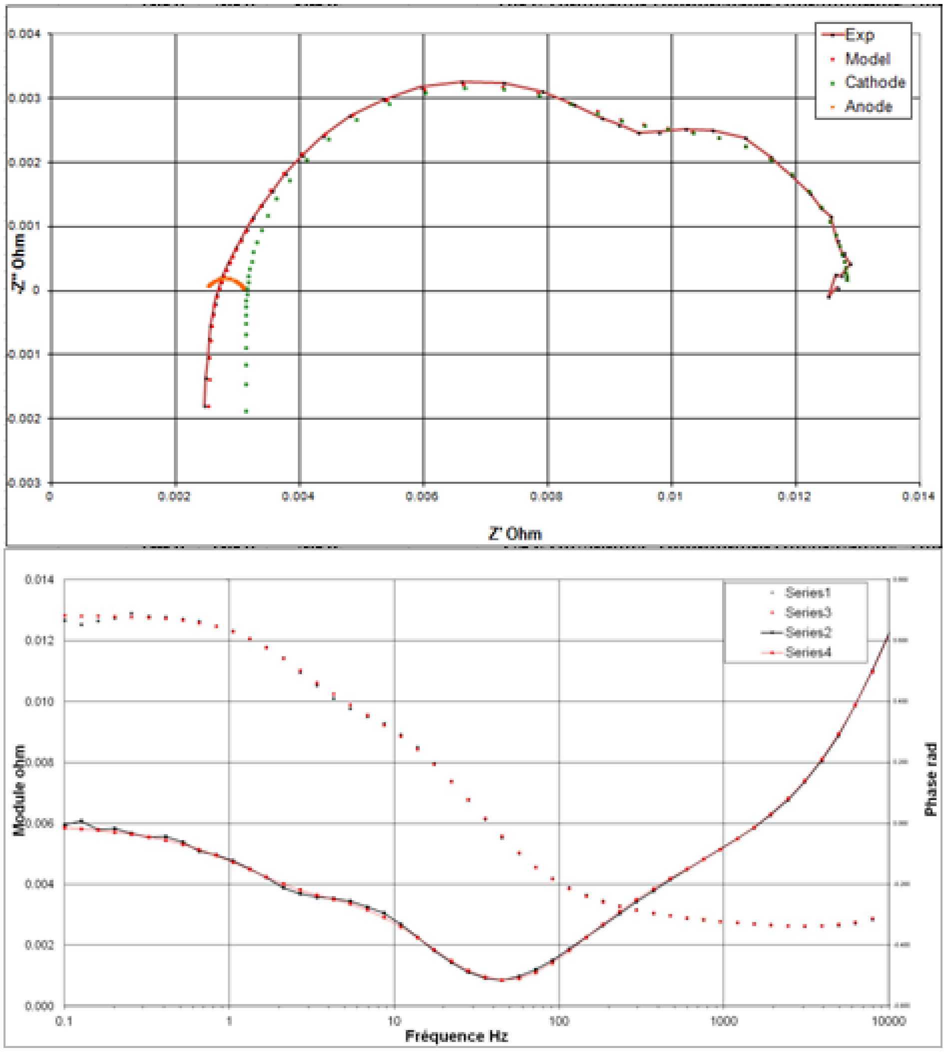

Figure 26 GEIS Fitting. (Top) Nyquist Plot and (Bottom) Bode Diagram.

This process was repeated for the stack and each individual cell for a total of four experimental values per day. In the model, the cathode capacitance Q_c, was determined to be the pseudo-capacitance. Q_c could not be measured directly because it is linked to the exponent, n_c. The capacitance was then estimated with a true capacitor, C_c and equivalent resistance, R_{Ceq}. The following relations were used (Franck-Lacaze et al., 2009).

$$C_c = Q_c \omega^{n_c - 1} \sin\left(\frac{n_c \pi}{2}\right) \tag{30}$$

$$R_{C,eq} = \frac{R_C}{1 + R_c Q_c \omega^{n_c} \cos\left(\frac{n_c \pi}{2}\right)} \tag{31}$$

After fitting, R_Ω, $R_{ct,eq}$ and V were plotted against time in hours.

3.1.2.2 Water Balance Calculations

Water management in a PEMFC is crucial to its stability and performance over its lifespan. At the end of each day, the water produced from each side of the cell was collected and massed. The temperature of the water vapor at the anode and cathode was also recorded. To monitor water production within the fuel cell, calculations were performed to compare the theoretical water production to the actual water produced within the stack.

First, a mass balance was conducted on the anode side of the fuel cell

$$F_{H_2 in} = F_{H_2 out} + F_{H_2 cons} \tag{32}$$

$$F_{H_2 cons} = \frac{I}{2F} \quad \text{and} \quad F_{H_2 in} = \lambda F_{H_2 cons} \tag{33}$$

where F is Faraday's constant (96485 coulombs/mol), I is the current (30A), and λ is the stoichiometric coefficient of hydrogen (1.5). Next, the water flow rates exiting at the anode is calculated. Water exiting at the anode was due to water transport from the cathode to the anode.

Because effluent water is both in vapor and liquid form, two calculations were conducted. The flow rate of vapor water exiting the anode ($F_{H_2O\ vap\ out\ A}$) is expressed as:

$$\mathrm{F_{H_2O\ vap\ out\ A}} = \frac{\mathrm{y_{H_2OA}}\left(\mathrm{F_{H_2OutA}}\right)}{1 - \mathrm{y_{H_2OA}}} \tag{34}$$

where $y_{H_2O\ A}$ is the water vapor fraction and F_{H_2OutA} is the flow rate of liquid water out of the anode. The water vapor fraction was calculated using Antoine's equation

$$\mathrm{P_{A\ H_2O}(atm)} = \exp\left(11.6703 - \frac{3816.44}{(273.15 + \mathrm{T}) - 46.13}\right) \tag{35}$$

where *T* is the measured temperature of the vapor exiting the anode in Celsius. By dividing the partial pressure by the total pressure (1 atm), the water vapor fraction was found. The flow rate of liquid water was determined from the mass of water collected in the lab over the time in which the experiment took place (~24 hrs).

The same principles were then applied to the cathode side. An oxygen balance was conducted where

$$\mathrm{F_{O_2in}} = \mathrm{F_{O_2out}} + \mathrm{F_{O_2cons}} \tag{36}$$

$$\mathrm{F_{O_2in}} = \frac{\lambda \mathrm{I}}{4\mathrm{F}} \quad \text{and} \quad \mathrm{F_{O_2out}} = \mathrm{F_{O_2in}}\left(1 - \frac{1}{3}\right) \tag{37}$$

Here, λ is 3. At the cathode, air is fed therefore; to calculate the flow of air into the cathode, $F_{O2,\ in}$ must be divided by 21%, i.e. the molar fraction of oxygen in air.

$$\mathrm{F_{air,in}} = \frac{\mathrm{F_{O_2in}}}{0.21} \tag{38}$$

At the cathode, water also entered the system. A complete water balance must then be conducted. Before entering the fuel cell, water and air enter a homogenizer. From the temperature of the cell, fixed at 55°C the temperature of the homogenizer can be found.

$$\mathrm{RH} = \frac{\mathrm{P}_{\mathrm{H_2O}}^{\mathrm{sat}}(\mathrm{T}_{\mathrm{Homogenizer}})}{\mathrm{P}_{\mathrm{H_2O}}^{\mathrm{sat}}(\mathrm{T}_{\mathrm{cell}})} \tag{39}$$

In the above equation, the relative humidity, *RH* is set to 62%. The saturated pressure values were equated using Antoine's equation. The temperature of the humidifier was then calculated. The water vapor fraction entering the system was then equated by:

$$\mathrm{y}_{\mathrm{H_2Oin}} = \frac{\mathrm{P}_{\mathrm{H_2O}}^{\mathrm{sat}}(\mathrm{T}_{\mathrm{Homogenizer}})}{\mathrm{P}_{\mathrm{Total}}} \tag{40}$$

The water vapor entering the fuel cell at the cathode was then found by:

$$\mathrm{F}_{\mathrm{H_2O\ vap\ in\ C}} = \frac{\mathrm{y}_{\mathrm{H_2Oin}}\left(\mathrm{F}_{\mathrm{air,in}}\right)}{1 - \mathrm{y}_{\mathrm{H_2Oin}}} \tag{41}$$

Water flow rates exiting the cathode were then calculated. The temperature of the vapor exiting the cathode was measured. The measured temperature was then used in Antoine's equation to determine the partial pressure of the vapor. The flow of the effluent vapor from the cathode was then

$$\mathrm{F}_{\mathrm{H_2O\ vap\ out\ C}} = \frac{\mathrm{y}_{\mathrm{H_2O}}(\mathrm{F}_{\mathrm{air\ out}})}{1-\mathrm{y}_{\mathrm{H_2O}}} \tag{42}$$

where y_{H_2O} is the vapor fraction determined by Henry's law and $F_{air\ out}$ was found by

$$\mathrm{F}_{\mathrm{air\ out}} = \mathrm{F}_{\mathrm{N_2}} + \mathrm{F}_{\mathrm{O_2 out}} \tag{43}$$

Similar to the anode, liquid water collected was weighed and then divided by the duration of time to calculate the flow rate of water produced at the cathode.

To calculate the percent error and the water transport coefficient (α), the theoretical water produced must first be calculated. Theoretical water produced is then calculated by:

$$\mathrm{F}_{\mathrm{H_2O\ Produced}} = \frac{\mathrm{I}}{2\mathrm{F}} \tag{44}$$

The water transport coefficient is then calculated by:

$$\alpha = \frac{F^{A}_{H_2O \text{ total out}}}{F_{H_2O \text{ Produced}}} \tag{45}$$

The outlet excess reactant coefficient was also calculated with the following relationship:

$$W = \frac{F_{H_2O \text{ out}}}{F_{\text{saturated } H_2O \text{ vapor}}} \tag{46}$$

By analyzing these two coefficients over time, an analysis was conducted on the degradation of the fuel cell stack.

3.2 Aging in a Defective Stack

Analysis of a three-cell defective stack was the second part of this project. The three-cell stack was connected in series with a defect in the first cell. The defect in the first cell consisted of a single pinhole in the MEA made by puncturing the MEA with a thumbtack. To produce comparable data to the healthy stack previously tested, equipment, operating conditions and stack assembly were identical to that of the healthy stack. Each experiment conducted on the healthy stack was repeated for the defective stack. Data was collected and analyzed daily and compared data from the healthy stack.

3.3 Theoretical Modeling

The final section of this project conducted at ENSIC consisted of predicting and verifying fuel cell performance through theoretical models. Using the polarization curve model developed in section 2.4.3, parameters were adjusted to fit experimental data previously collected on a single cell PEMFC. The single cell consisted of a 100 cm^2 MEA operating at 55°C. At the anode, the catalyst was composed of equal parts ruthenium and platinum; the cathode catalyst was composed of platinum. Data collected from the single cell ranged from a current density (*i*) of 0.1 A/cm^2 to 0.8 A/cm^2. EIS data was also extracted from the single cell.

3.3.1Modeling Parameters

The polarization modeling was first conducted. Specific parameters from the single cell are shown in Table 3. Parameters were estimated from literature from a typical PEMFC (Datta, 2011; Vilekar & Datta, 2010).

Table 3 Parameters for theoretical model. Parameters were specific to the single cell fuel cell and estimated according to literature (Datta, 2011; Vilekar & Datta, 2010). Sample calculations can be found in Appendix A

Operating Parameters		**Anode**		**Cathode**	
T (K)	328	αa	0.5	αc	0.5
P_T (atm)	1	vae	1	vce	-2
		iaoref(A/cm^2)	3.00E-3	icl(A/cm^2)	1.5
		ial(A/cm^2)	4	icoref(A/cm^2)	1E-10
		$E_{A,\varphi 0}$ (kJ/mol)	34.6	$E_{C,\varphi 0}$ (kJ/mol)	67.0

Because the cell operated at (55°C) the thermodynamic voltage was adjusted by:

$$V_0 = 1.229 - 8.46 \times 10^{-4}(\mathrm{T} - 298) + \frac{\mathrm{RT}}{4\mathrm{F}}\ln(\mathrm{p}_{\mathrm{H_2}}^2 \mathrm{p}_{\mathrm{O_2}}) \tag{47}$$

where p_{O_2} and p_{H_2} were the partial pressures of oxygen and hydrogen respectfully. Partial pressures were then calculated by:

$$\mathrm{p}_{\mathrm{O_2}} = \mathrm{x}_{\mathrm{O_2}}(\mathrm{P_T} - \mathrm{p_W}) \tag{48}$$

$$\mathrm{p}_{\mathrm{H_2}} = \mathrm{x}_{\mathrm{H_2}}(\mathrm{P_T} - \mathrm{p_W}) \tag{49}$$

The partial pressure of water (p_W) was calculated using Antoine's equation. The mole fraction *(x)* of oxygen and hydrogen were 0.21 and 1 respectively.

The roughness factor γ_m was then adjusted in accordance to catalyst parameters described in Table 4. At the anode, the catalyst was composed of equal parts ruthenium and platinum. Since the oxidation on ruthenium was negligible, the catalyst loading at the anode was calculated by:

$$m_{m,total} = M_{PT}y + M_{RU}y \tag{50}$$

where 0.45 mg cm^{-2} was the total catalyst loading at the anode and M_i was the molar mass (Huang, 2012). By first evaluating the number of moles *(y),* platinum loading at the anode was then equated.

Table 4 Roughness parameters (Huang, 2012).

	Anode	Cathode
$\boldsymbol{d_m}\ (\boldsymbol{nm})$	5.60	3.20
$\boldsymbol{m_m}\left(\frac{\boldsymbol{mg}}{\boldsymbol{cm^2}}\right)$	0.225	0.400
$\boldsymbol{\rho_m}\left(\frac{\boldsymbol{g}}{\boldsymbol{cm^3}}\right)$	21.45	21.45
$\boldsymbol{\varphi}$	0.95	0.95

The exchange current densities were then determined for the anode and cathode as described in section 2.4.3 where:

$$\mathrm{i_0} = \gamma_{\mathrm{m}}\left(\frac{\mathrm{p_i}}{\mathrm{p_{i,ref}}}\right)\exp\left\{-\frac{\mathrm{E_\Phi}}{\mathrm{R}}\left(\frac{1}{\mathrm{T}}-\frac{1}{\mathrm{T_{ref}}}\right)\right\}\mathrm{i^*_{0ref}} \tag{51}$$

Next, the crossover current at the cathode was calculated by:

$$\mathrm{i_{C,x}} = \frac{2\mathrm{Fk_Hp_H}}{\mathrm{L_{EL}}} \tag{52}$$

where $\mathrm{L_{EL}}$ was the thickness of the membrane (18μm). $\mathrm{K_H}$ or the permeability of hydrogen was calculated by (Vilekar & Datta, 2010):

$$\mathrm{k_H} = 6.61 \times 10^{-8}\exp\left(-\frac{21030}{\mathrm{R\,T}}\right) \tag{53}$$

Both the anode and cathode overpotentials were then calculated using methods described in **2.4.3.**

To complete the polarization model, the membrane overpotential was evaluated. From section 2.4.3, the membrane overpotential was derived as:

$$\eta_{EL} = i\left(\frac{L_{EL}}{\sigma_{EL}}\right) \tag{54}$$

where $L_{EL}$was the membrane thickness (18μm). The protonic conductivity $\sigma_{EL}$was estimated using (Thampan et al., 2001) as well as assumptions made due to the material manufactured by Gore. σ_{EL} was calculated by:

$$\sigma_{EL} = (\epsilon_o(\epsilon_B - \chi))^{1.5}\left(\frac{349.8}{1+\delta}\right)\exp\left(-\frac{E_u}{R}\left(\frac{1}{T}-\frac{1}{298}\right)\right)C_{H_2O}\beta \tag{55}$$

where the Nafion volume fraction in the Gore ePTFE membrane, ϵ_o, was estimate to be 0.7, the ratio of effective diffusion coefficients, δ, was 5.5, and the activation energy, E_u, was 14000. The volume fraction of water in the membrane, ϵ_B, was evaluated by

$$\epsilon_B = \frac{\lambda}{\frac{537}{18}+\lambda} \tag{56}$$

where λ (14) was the number of molecules absorbed per –SO$_3$H group. The concentration of water, C_{H_2O} was also related to λ by:

$$C_{H_2O} = \frac{1}{18\lambda} \tag{57}$$

The percolation threshold or the ability of the electrochemical species to pass through the membrane was expressed as:

$$X = \frac{1.8}{\frac{537}{18}+1.8} \tag{58}$$

The degree of dissociation in terms of the equilibrium constant, K_A, was:

$$\beta = \frac{\lambda + 1 - \sqrt{(\lambda + 1)^2 - 4\lambda\left(1 - \frac{1}{K_A}\right)}}{2\left(1 - \frac{1}{K_A}\right)} \tag{59}$$

where

$$K_A = 6.2\exp\left(\frac{52300}{R}\left(\frac{1}{T} - \frac{1}{298}\right)\right) \tag{60}$$

The theoretical polarization curve was then plotted with data extracted from the single cell. Estimated values i.e. limiting current densities and reference exchange current densities were evaluated to ensure that the model and data correlated.

After obtaining the theoretical polarization curve, the theoretical resistances (R_A, R_c, R_{EL}) were compared resistances extracted from EIS.

For complete theoretical calculations, please see Appendix A.

4.0 Results and Discussion

The main objective of this project was to compare and analyze aging in a three-cell healthy stack to a three-cell stack with a pinhole defect operating at nominal conditions. The next objective was to verify the use of theoretical models to predict cell performance of a single cell. This section will investigate gathered experimental results in comparison to literature and theory.

4.1 Aging in a Healthy Three-Cell Stack

The analysis of the healthy three-cell stack in this project yielded results that corresponded to degradation theories and mechanisms detailed in this report. This portion of the report will provide a review of the results and suggest the degradation phenomena that reduced the PEMFC stack performance over time.

4.1.1 Electrochemical Impedance Spectroscopy

By modeling the impedance spectra, resistance values within the fuel cell stack could be obtained and analyzed. Data collected daily for four weeks from the healthy stack was graphed as shown in the figures below. Experimental data illustrated a relative constant ohmic resistance for the three individual cells; however, the second cell in series (Cell 2) demonstrated a lower ohmic resistance. An overall increase in charge transfer and diffusion resistances was also observed. Complete data is included in Appendix B.

4.1.1.1 R_Ω

The ohmic resistances extracted from the cells remained relatively constant throughout the four week period as seen in Figure 27. The ohmic resistance of each cell is of the same magnitude; however, Cell 2 demonstrates a smaller resistance than Cell 1 and Cell 3. This inconsistency in ohmic resistance may be attributed to the setup of the stack. Physically within the stack, Cell 2 was sandwiched between Cell 1 and Cell 3, requiring different clips to achieve contact with the electrodes. The difference in resistance, about 0.025 ohm cm^2, was observed between Cell 2 and Cell 1 and 3.

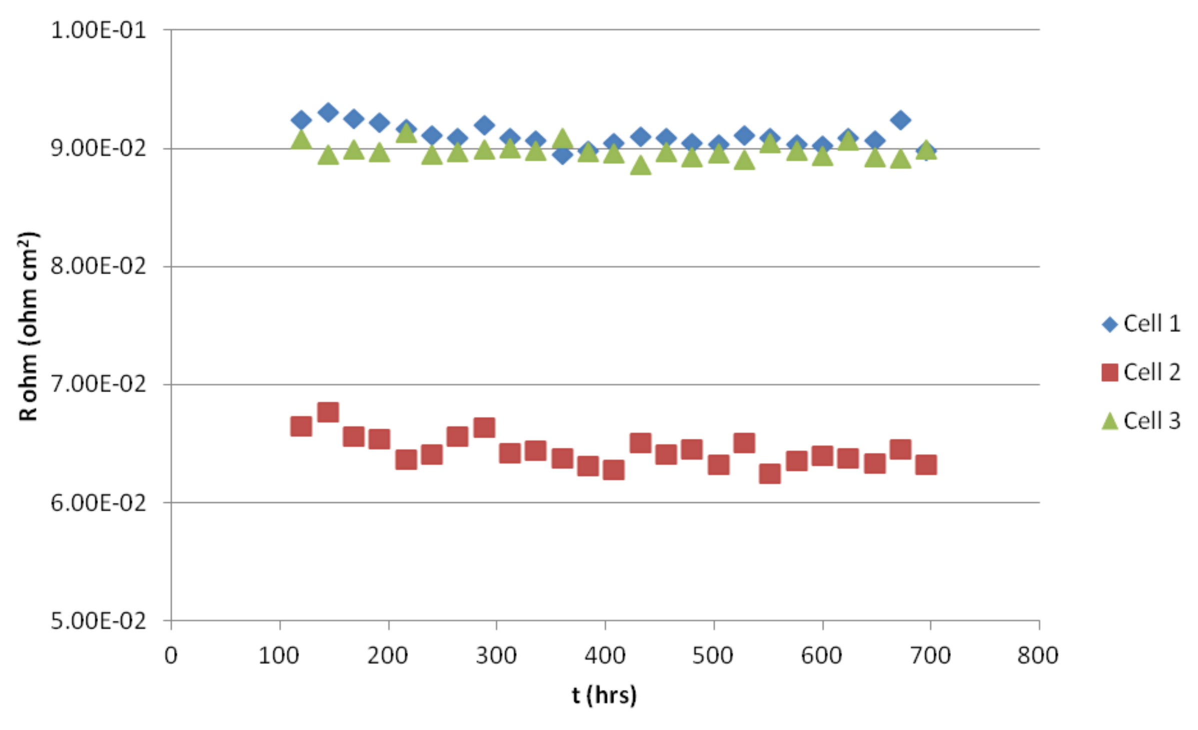

Figure 27 Healthy Stack: $R_{ohm, C}$. Ohmic resistance is relatively constant throughout the four week period. The stack was composed of three healthy cells connected in series with an active MEA area of 100cm^2 per cell; operating conditions were T_{FC}=55°C, $T_{ambient}$ fluctuated over span of experiment. i=0.3A/cm^2, P=1 atm.

Although the ohmic resistance remained fairly constant throughout the experiment, theoretically, the ohmic resistances should slightly increase. From this data, conclusions for performance, based on the positioning of the cells cannot be made considering the difference in Cell 2 probably was due to differing cable resistance.

The reproducibility of results across the cells suggests that the components of the fuel cell were not subject to gross manufacturing defects as well. Membrane drying probably did not contribute to the ohmic resistance since the membrane was well saturated. It is likely that some of the chemical mechanisms for membrane degradation detailed in the background of this report occurred in the PEMFC stack; however, a water fractions analysis would be necessary to understand what portion of the polymer chains cleaved. The mechanisms shown in Equations 4-8 and Equations 9-11 are most likely to have occurred.

Ostwald ripening of platinum or ruthenium catalyst may have caused platinum precipitation within the membrane, and increased ohmic resistance. This would proceed to block ionomeric pores in the membrane, limit proton conductivity and potentially provide surface for crossover gases to react and produce pinholes. It is unlikely that significant precipitation occurred given the time span of the experiment. Factoring the steady-state setup of the fuel cell, with constant reactant gas flow rates and relative humidity, these results validate the consistency in the ohmic resistance seen in previously in experiments run by LRGP.

4.1.1.2 R_d

The diffusion resistances were observed to increase at similar rates for each of the three cells, demonstrated in Figure 28. The rate of increase of the diffusive resistance in Cell 2 was greater than those of either of the other two cells. This is indicative of a hindrance between the catalyst layer and the bipolar plates of the cells. Greater mass transport resistance in Cell 2 could be due to the geometry of the inlet flows and outlet flows of the fuel cell stack or even temperature variations between the inner cell and the outer two cells or across the GDLs of the cells. An increase in mass transport resistance may also be due to water generation and accumulation due to carbon (carbon support and GDLs) degradation. As water accumulates, oxygen transport at the cathode is limited. In addition to traveling through the GDL, the oxygen must diffuse through the excess water molecules too. Oxidation of oxygen containing groups at the surface of carbon is likely to have occurred. The data's upward trend suggests that the corrosion of the carbon support of the catalyst and the carbon may be a primary contributor to the increases in diffusion resistance.

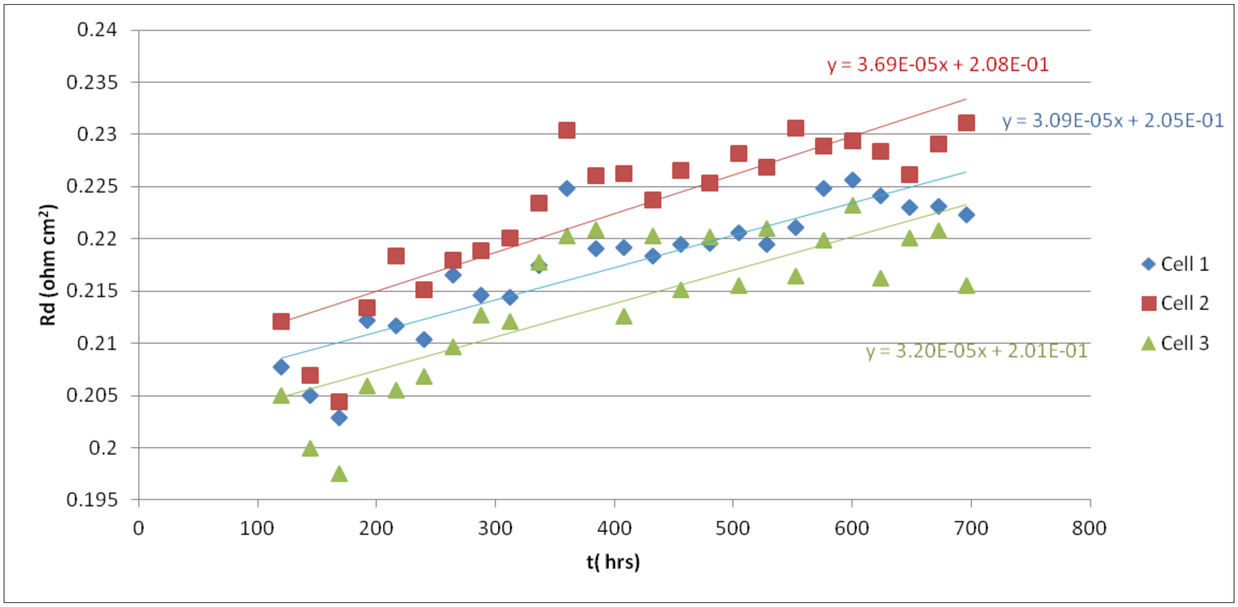

Figure 28 Healthy Stack: Individual Cell $R_{d,\ C}$. The diffusion resistance at the cathode over the four week period linearly increases. The stack was composed of three healthy cells connected in series with an active MEA area of $100cm^2$ per cell; operating conditions were T_{FC}=55°C, $T_{ambient}$ fluctuated over span of experiment. i=0.3A/cm^2, P=1 atm

4.1.1.3 R_{ct}

Like diffusion resistances, the charge transfer resistances increased for each of the three cells. The rate of increase was not uniform for each cell as shown in Figure 29. The charge transfer resistance in Cell 2 increases faster than that of the other two cells. As the charge transfer resistance grows, the kinetics of the oxygen reduction reaction (ORR) slows down. The increase in charge transfer resistance across the cell can be substantiated by recognizing the chemical degradation at the three-phase-interface between the membrane and cathode. It is here that oxygen is reduced, accepting electrons. It is also a prime region for undesired, membrane and catalyst degradation to occur.

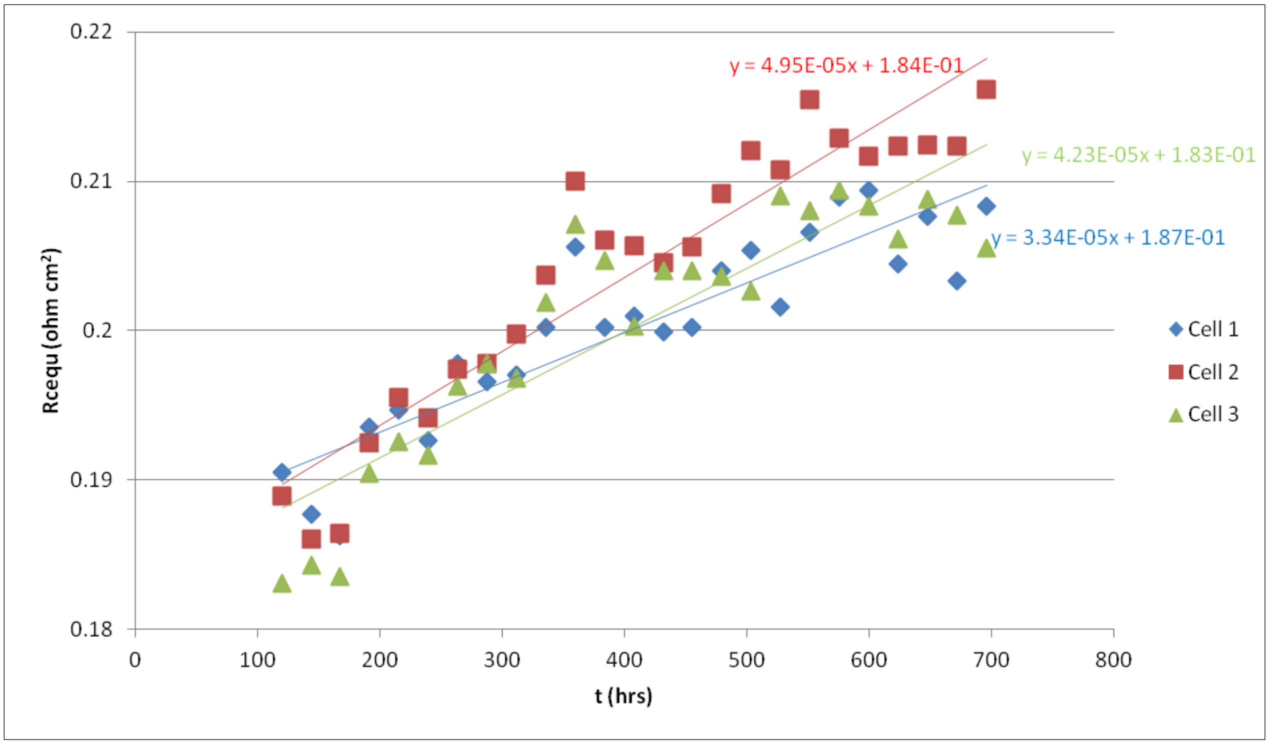

Figure 29 Healthy Stack: Individual Cell $R_{ct,\,C}$. Like diffusion resistance, the charge transfer resistance at the cathode also linearly increases over time. Cell 2 provides a larger resistance than Cell 1 or 3. The stack was composed of three healthy cells connected in series with an active MEA area of $100cm^2$ per cell; operating conditions were $T_{FC}=55^oC$, $T_{ambient}$ fluctuated over span of experiment. $i=0.3A/cm^2$, P=1 atm

A decrease in catalyst surface area may also promote catalyst degradation. Catalyst degradation through dissolution into water may have contributed to Ostwald ripening, in which this dissolved catalyst may deposit in the membrane on agglomerate on the electrode. Corrosion of the carbon support as mentioned in section 4.1.1.2 is also a probable factor increasing charge transfer resistance.

Equations 5-7 detail how destructive radicals are formed within a PEMFC, through the breakdown of hydrogen peroxide that can be formed with the presence of hydrogen crossover at the cathode. The general increase in charge transfer resistance could also be attributed to thermal variations to the system caused by temperature fluctuations impacting outlet streams. The increase of the charge transfer resistance also could be due to water accumulation. Accumulation in fuel cells blocks active catalyst sites, slowing oxygen reduction reaction kinetics at the cathode.

4.1.2 Cell Voltages

From spectrometry data, voltage data was also obtained. Over time, the voltage decreased within each cell. When the voltage fluctuated, it did so in a pattern consistent across all the cells in the stack. This was most probably a result of changes to operating conditions. Such conditions included hydrogen supply and temperature. Figure 30 illustrates the voltage from each healthy cell over the four week period.

The cell voltages indicate that performance of the cells in the fuel cell stack was steadily declining over the four-week experiment. The differences in perceived performance output may be a result of varying resistances in the cables used to record voltage. The positioning of the cells may have played a legitimate role in the differing voltages of the cells if the resistances of the cables were insignificant. The reactant gas streams entering the fuel cell stack entered at Cell 1 and then flowed through Cell 2 and then Cell 3. It is probable that the flow rates of the gases were higher in Cell 1, gradually decreasing through Cell 2 and then Cell 3 due to pressure drop. This expected difference in pressure drop and corresponding flow rate, may have dried out the membrane in Cell 1, more so than in Cell 2 or Cell 3, potentially causing the difference seen in the data. The resistance discussion provided by the EIS spectroscopy in section 4.1.1 presented possible degradation mechanisms occurring in the cells. These mechanisms are also applicable to the reduction in cell voltage, although conclusions regarding the differences in voltages of the individual cells cannot be fully extracted.

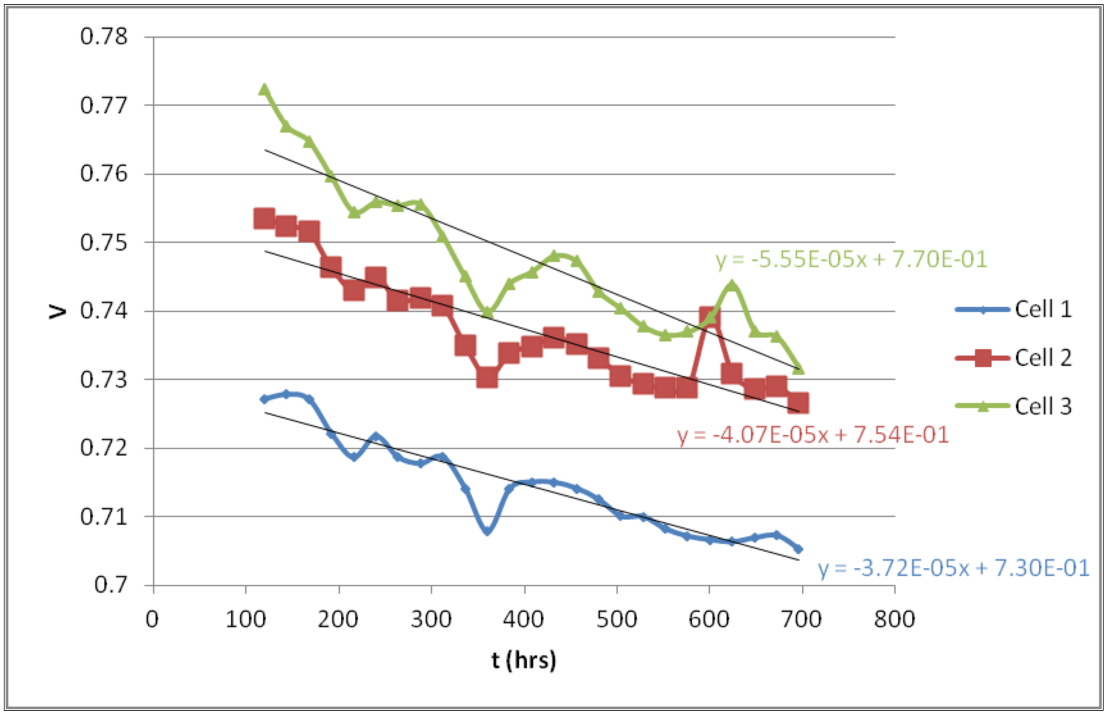

Figure 30 Healthy Stack: Individual Cell Voltage. Decreasing linearly with time at similar magnitudes for the each of the cells in the stack, voltage is a primary indicator of fuel cell degradation. The stack was composed of three healthy cells connected in series with an active MEA area of 100cm^2 per cell; operating conditions were T_{FC}=55°C, $T_{ambient}$ fluctuated over span of experiment. i=0.3A/cm^2, P=1 atm

4.1.3 Water Management

Over a span of four weeks, water mass and outlet temperature data were collected for the PEMFC stack. The data gathered from the stack helped in the computational analysis of the mass balance and water management, and thereby can be used as a metric for PEMFC efficiency. Water was collected from the anode and cathode outlets of the stack, but it is important to recognize that no water is generated or supplied to the anode side. Water enters cells at the cathode side through the humidified air and is generated by the ORR. Two parameters were used to observe the residence time of water in the stack: the water transport coefficient, α, and W.

The water transport coefficient is the ratio of the net water flux or flow rate out of the fuel cell at the anode side, to the water produced by the cell. α is an indicator of water management within the cell, indicating the net water flux from the cathode to the anode since dry hydrogen is fed to the anode side.

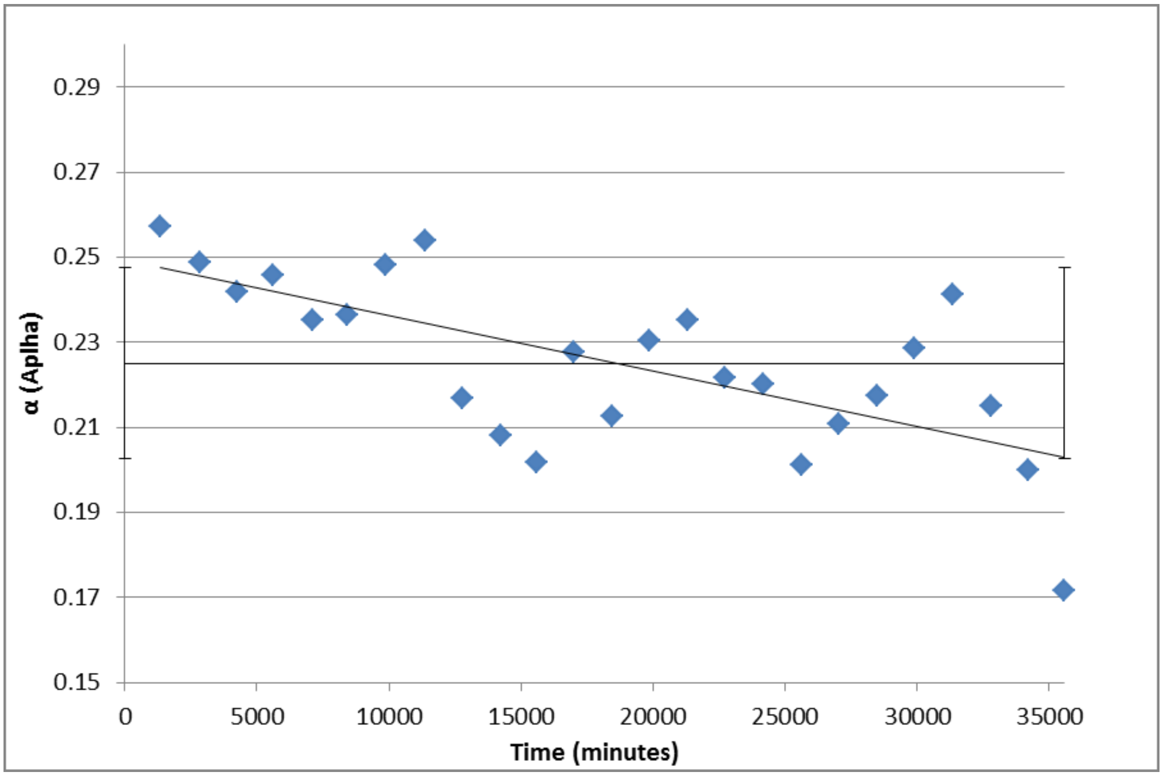

Figure 31 Healthy Stack: Water Transport Coefficient α over a run time of 35570 minutes. 10% error bars are shown based on average value of data points. The data shows a moderate downward trend as either electro-osmotic drag becomes stronger or diffusive flux becomes weaker. (T_{FC}=55°C, $T_{ambient}$ fluctuated over span of experiment. i=0.3A/cm^2

Figure 31 shows the data from the healthy stack run over the span of four weeks. The data indicates a moderate drop in α over time; however, the correlation is not strong enough to warrant a causal relationship. If the relationship was valid, the electro-osmotic drag may have increased, the diffusive flux may have decreased, or a combination of the two, may have occurred.

The excess reactant coefficient W is the ratio of the water flow (both vapor and liquid) of one outlet of the PEMFC to the flux of saturated vapor exiting the same outlet of the fuel cell.

(Huang, 2012) This coefficient generalizes the phases of water that exist the cell. The water is completely vapor when W is between zero and one, saturated vapor when W is equal to one and completely liquid when W is greater than one. Values for W were calculated for both the anode and cathode sides of the fuel cell and are presented in Figure 32 and Figure 33.

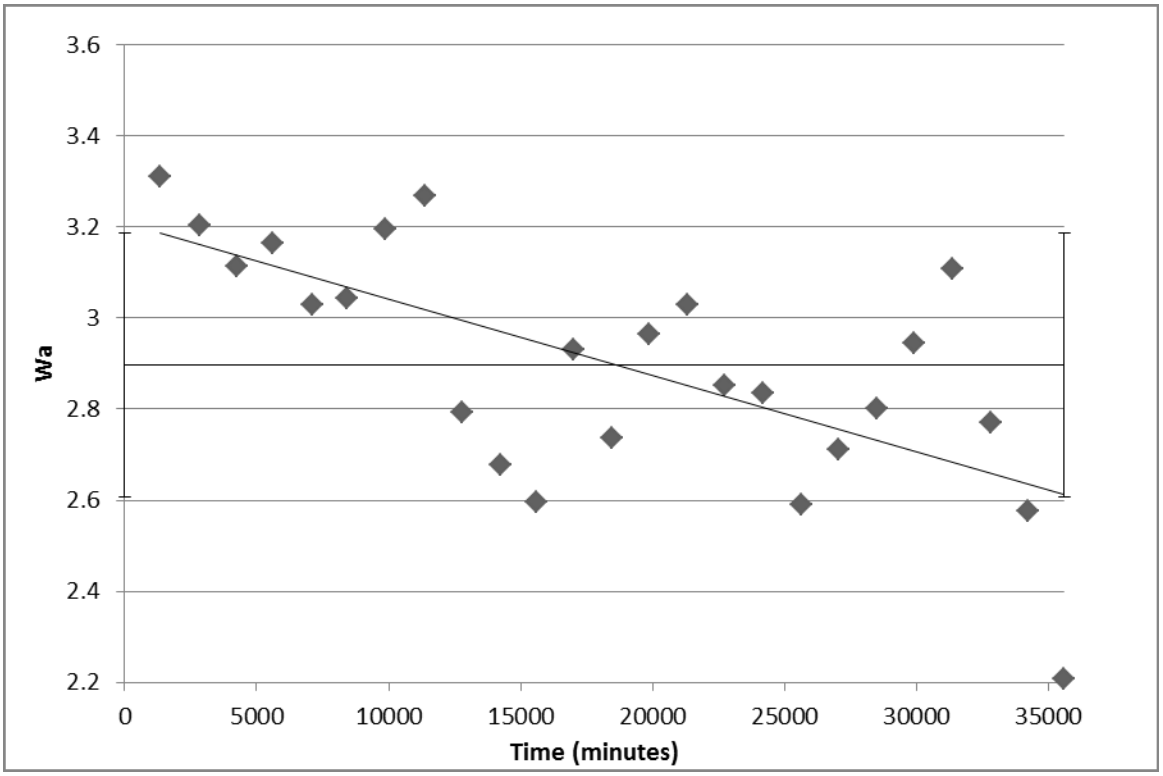

Figure 32 Healthy Stack: Excess Reactant Coefficient W_a over a run time of 35570 minutes. 10% error bars are shown based on average value of data points. The data shows a slight downward trend as the vapor content of the anode stream increases. (T_{FC}=55°C, $T_{ambient}$ fluctuated over span of experiment. i=0.3A/cm^2)

Figure 32 shows the values of W_a over the experiment performed with a healthy stack of fuel cells. The data shows that W is exclusively positive, illustrating that water there is a significant amount more water at the anode side than calculated at saturation. This indicates that liquid water is present in excess at the anode. Figure 33 displays the values of W_c over the duration of the experiment, and is also positive, but less so than W_a. This indicates that the cathode also has more liquid water than expected at saturation, but to a lesser extent than the anode outlet.

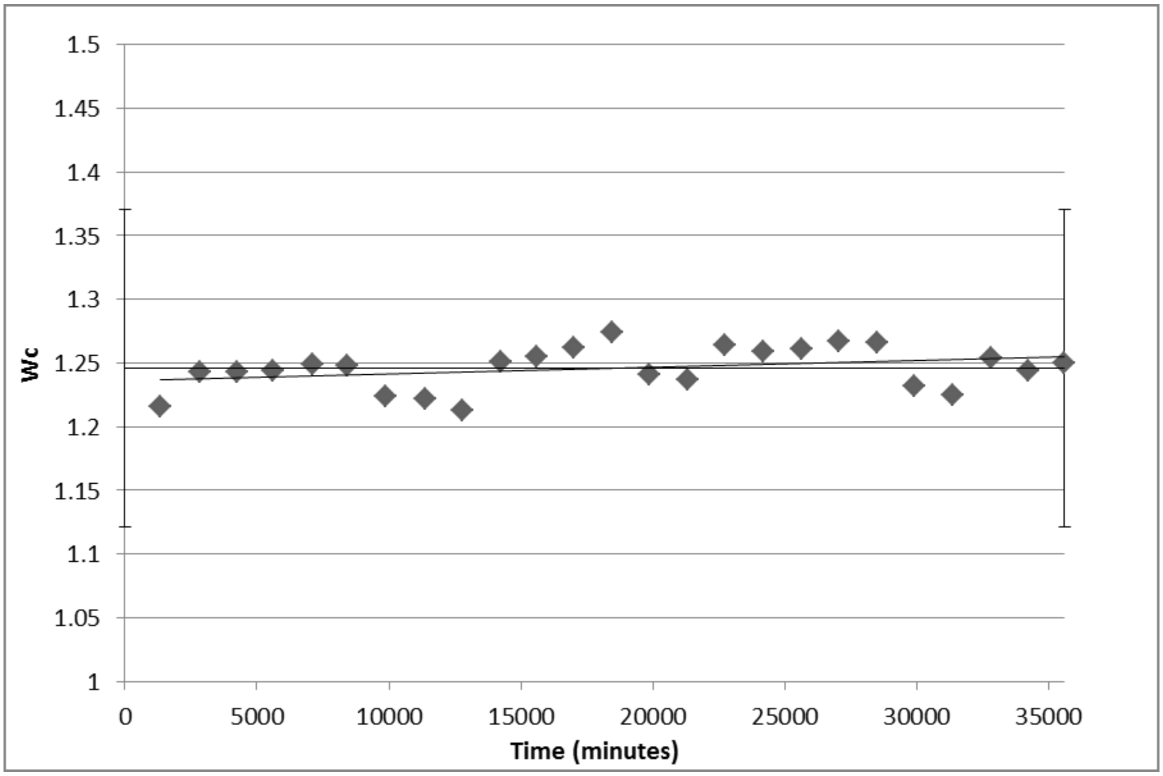

Figure 33 Healthy Stack: Excess Reactant Coefficient W_c over a run time of 35570 minutes. 10% error bars are shown based on average value of data points. The data shows a slight downward trend as the vapor content of the cathode stream increases. (T_{FC}=55°C, $T_{ambient}$ fluctuated over span of experiment. i=0.3A/cm^2)

The W_a values are seen to have much more variation than W_c data. This variation stems from the inherent difference in mass transport of the water at the cathode and the anode. At the cathode, the water travels through the GDL, bipolar plate and exits the stack. At the anode, however, the water must travel across the membrane in addition to the GDL and bipolar plate of the anode side, increasing variability. These values correspond to the positive α values discussed earlier in this section, since the net flux is from the cathode to the anode side. This verifies that the membrane is likely to be fully saturated, as the W_a values are firmly positive, and the α values indicate that the water solely entering at the cathode side is indeed travelling to the anode side.

Membrane drying, therefore, should contribute significantly to reduced performance and degradation of the PEMFC stack over time. The fuel cell researchers at ENSIC, have decided that humidification for fuel cells proves to deliver greater performance based on literature and prior experiments, although a general consensus in academia and the industry has not been reached. (Huang, 2012)

4.2 Aging in a Defective Stack

In an effort to observe the effects of pinhole defects in a PEMFC stack, the MEA of the first cell in a three-cell stack was punctured to produce pinholes. At first, one pinhole was introduced; however, no discernible differences in the data trends were observed. Hydrogen supply problems also occurred throughout the experiment. After a week, this test was terminated and followed by a similar setup, except with 16 pinhole defects reproduced in the first cell of the three-cell stack as shown in Figure 34.

Figure 34 MEA with 16 pinholes.

This test also encountered problems; however, with a fault in a hydrogen supply line the data was invalidated. Since the data in these two experiments were gathered over a short span, they were not particularly effective at showing a change in the patterns of the fuel cell stack over time.

4.3 Theoretical Modeling

Polarization and EIS data collected on a single cell were compared to theoretical models and calculations. Figure 35 illustrates the correlation of the theoretical model to polarization data collected using the given parameters. Here, the theoretical model closely correlates to the experimental data. Discrepancies occur between the theoretical and experimental values at higher current densities.

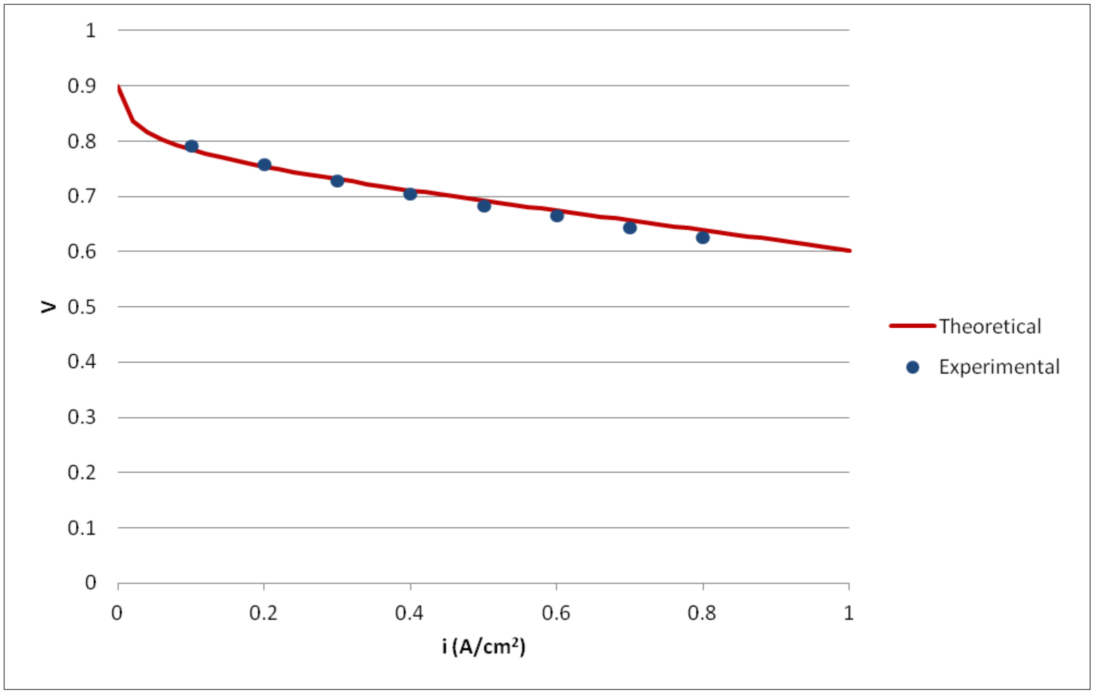

Figure 35 Theoretical polarization curve correlation with experimental data. T=55°C, P=1atm, RH= 62%, σ_{EL}=.026 s cm^{-1}, i_{CL}= 1.5 A cm^{-2} i_{AL}= 4 A cm^{-2}, R_I=0 rest of values found in Section 3.3

Next, the calculated and extracted resistances from EIS were compared. Figures 36 and 37 illustrate the correlation between the theoretical and experimental charge transfer resistances.

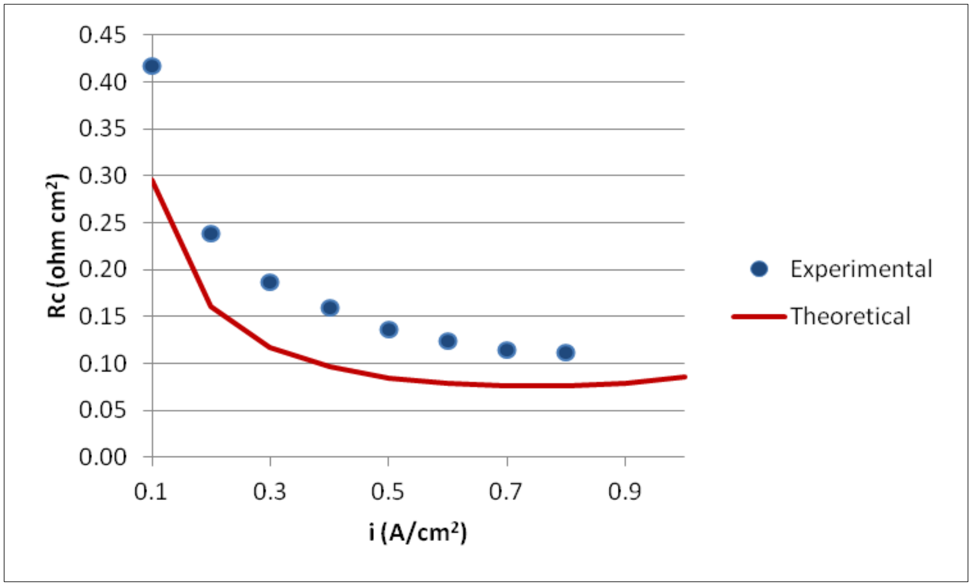

Figure 36 R_c compared to model. The cathode charge transfer resistances display the same decreasing trend. The model and EIS data do not closely correlate. T=55°C, P=1atm, RH= 62%, σ_{EL}=.026 s cm^{-1}, i_{CL}= 1.5 A cm^{-2} i_{AL}= 4 A cm^{-2}, R_I=0 rest of values found in Section 3.3

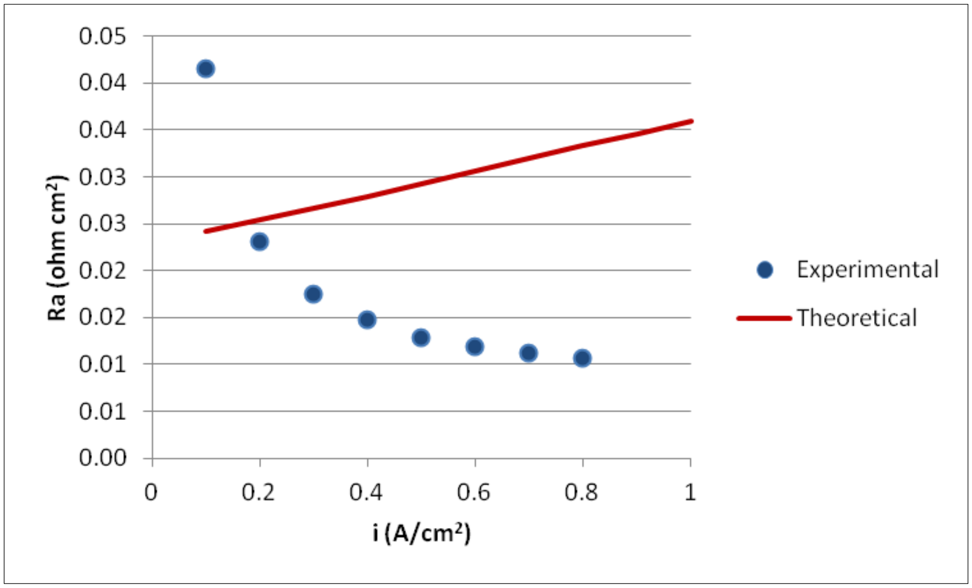

Figure 37 R_A compared to model. Experimental and theoretical charge transfer resistance did not trend the same T=55°C, P=1atm, RH= 62%, σ_{EL}=.026 s cm^{-1}, i_{CL}= 1.5 A cm^{-2} i_{AL}= 4 A cm^{-2}, R_I=0 rest of values found in Section 3.3

Although the charge transfer resistances at the cathode demonstrated the same decreasing trend, values were slightly skewed. Anode charge transfer resistances did not match the predicted resistances calculated from the model. In an effort to further model the anode charge transfer resistance, another model was proposed. The new model simplified Equation 27 to:

$$R_A = \frac{RT}{2F\alpha_A^*\nu_{Ae-i_{Ao}}\sqrt{1+\frac{1}{4}\left(\frac{i}{i_{Ao}}\right)^2}} \qquad (61)$$

where any resistance due to diffusion was negated (Lapique, 2012). The new relationship, shown in **Figure 38**, further confirmed that the model was not sufficient to predict anode charge transfer resistance collected from EIS.

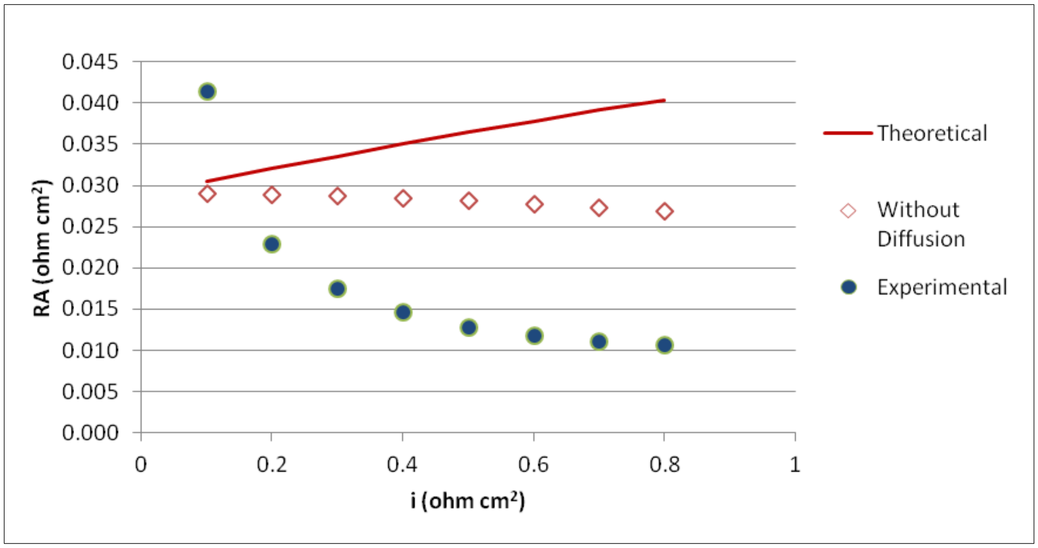

Figure 38 R_A compared to model. Experimental and theoretical charge transfer resistance did not trend the same T=55°C, P=1atm, RH= 62%, σ_{EL}=.026 s cm^{-1}, i_{AL}= 0 A cm^{-2}, R_I=0 rest of values found in Section 3.3

Significant differences between the anode charge transfer resistances may be due to two reasons. The first is the uncertainty in EIS fitting. Anode charge transfer resistance is incorporated into the high frequency arc of the Nyquist plot. This arc is dominated by the resistances occurring at the cathode. Anode charge transfer resistance is then set to one tenth of the cathode charge transfer resistance. This is why both experimental charge transfer resistances trend in the same manner. The second explanation is the kinetics within a fuel cell. Reaction kinetics within a fuel cell is complex consisting of many parameters. A more specific model may be needed to appropriately predict fuel cell behavior at the anode.

Finally, the calculated (R_{EL}) and experimental (R_{Ω}) ohmic resistances were compared. From EIS data, the ohmic resistance was constant at 0.108 ohm cm^2. The theoretical resistance was calculated to be 0.068 ohm cm^2. Although not exact, ohmic resistance were comparable identifying that the model was sufficient.

4.3.1 Predicting Healthy Stack Performance

By developing the polarization curve, the decline in voltage of the healthy fuel cell stack was modeled. Over the four weeks, the decline in potential could be attributed to decrease in catalyst surface roughness, $\gamma_{m.}$ If the decline in surface area is due to catalyst dissolution and agglomeration, the kinetics can be given by:

$$\frac{d\gamma_m}{dt} = -k\gamma_m \tag{62}$$

which was integrated to obtain an expression for both the anode and cathode surface roughness. (Gu et al., 2009)

$$\gamma_m = \gamma_{m0}e^{-kt} \tag{63}$$

In this case, k, the rate constant, was predicted to be $9 \times 10^{-4}/\mathrm{h}$. By using this correlation and estimated rate constant, data collected from the healthy stack was compared to the model as seen in Figure 39. Here, the predicted decline in voltage can only be related to Cell 1.

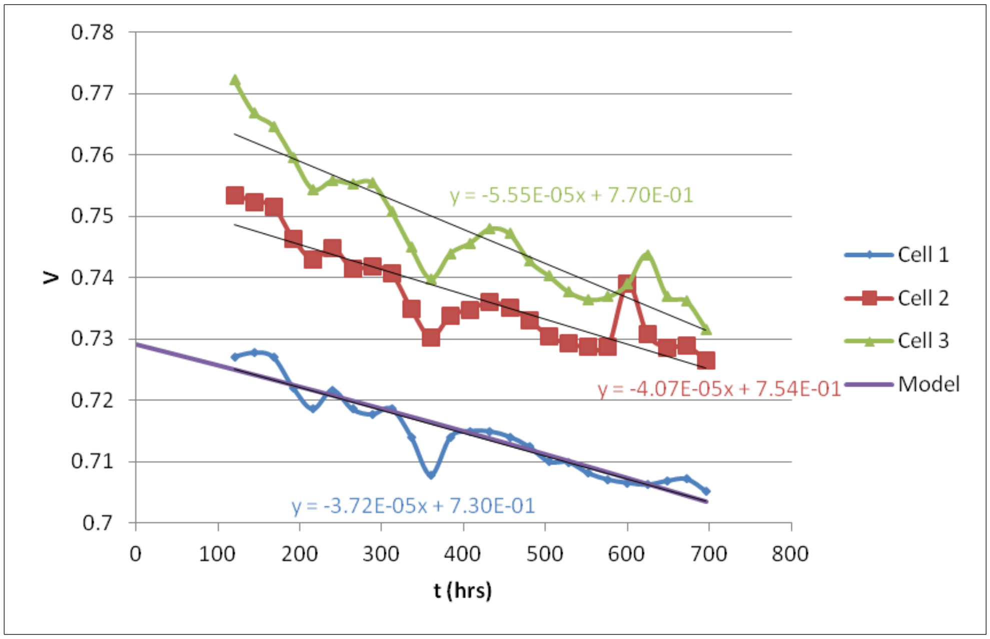

Figure 39 Predicted decline of cell voltage. Predicted values were compared to voltage decline from the healthy fuel cell stack at an operating current density of 0.3 A/cm^2. T=55C, P=1atm.

Using the same method, the increase in cathode charge transfer resistance in the healthy stack was predicted as seen in Figure 40.

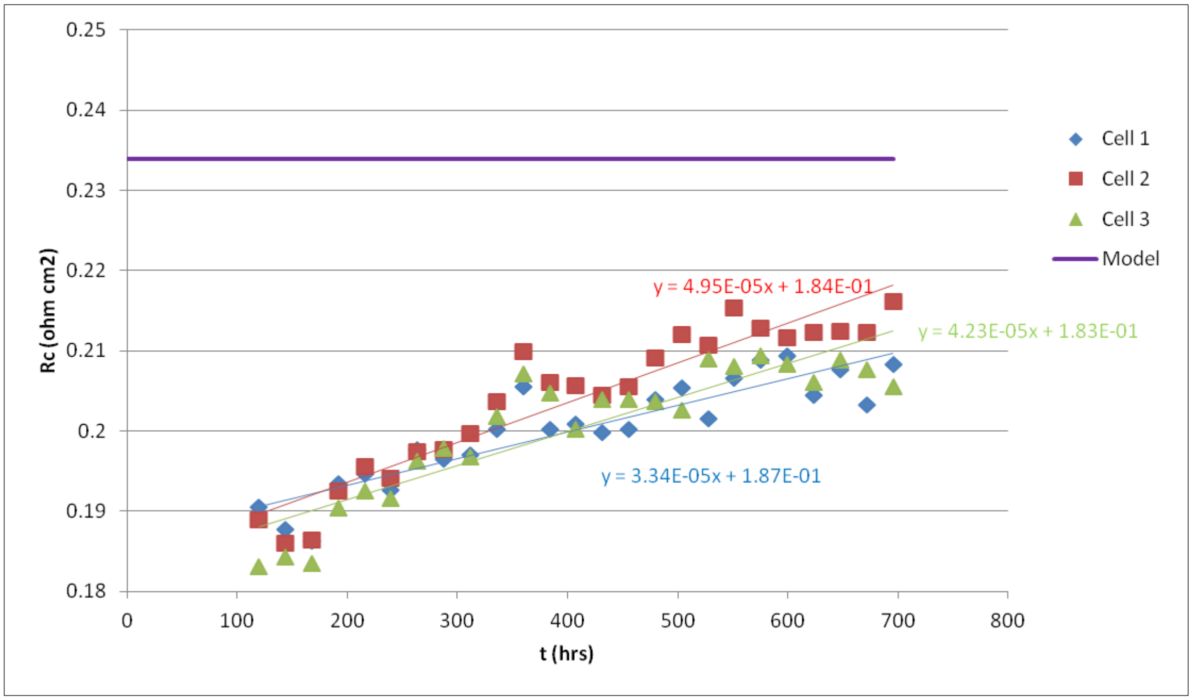

Figure 40 Predicted increase in cathode charge transfer resistance. Operating conditions were current density of 0.3 A/cm^2. T=55C, P=1atm

Although the model may predict voltage decline, it is not sufficient in predicting resistance for the healthy stack. Further research is needed to develop model to predict resistances within a fuel cell stack.

5.0 Conclusion and Future Work

The electrochemical impedance spectroscopy (EIS) results illustrate that degradation was present within the three-healthy-cell fuel cell stack examined in this project. The EIS experiment data correlated well to the trends of increasing resistances that occur with the degradation mechanisms detailed in this report. With the ohmic resistance remaining fairly constant and the charge transfer resistance and diffusion resistance increasing over the span of four weeks, the resistances match the relative rates of the degradation models. Based on position and geometry of the cells within the fuel cell stack that was employed in this project, the data seemed to show that Cell 2 had greater diffusion resistance than the other two cells, and a higher rate of increase in charge transfer resistance. The diffusion resistance results are not distinguished enough to truly determine a different trend for Cell 2 than Cells 1 and 3; however, since the rate of increase in the charge transfer resistance was higher for Cell 2, it is possible that the trend would have continued. Further experiments using accelerated stress testing or ones that are longer in duration could be conducted to validate these trends.

The data from the water balance analysis also supported some of the expected phenomena in a PEMFC. The water transport coefficient, representative of the net flow of water through the membrane, verified that the net flow is in the direction from the cathode to the anode since all of the values were steadily positive. The net flow expected to be in this direction since water is generated at the cathode and humidified air is delivered to the cathode side. The excess reactant coefficients for the anode and cathode showed a similar trend in consistency of data. The vapor content in the anode outlet increased slightly over time while the cathode outlet vapor content decreased slightly.

In current literature and research, many aging tests are conducted on single cells. From experiments conducted on the healthy stack, further research areas were identified. Experiments with increased operating temperature or pressure may be an area of interest. Other future experiments may include current cycling, humidity cycling and further accelerated aging tests.

Ensuing experiments on aging in a defective stack turned out to be unsuccessful due to complications and the short time span of this project. The initial experimental plan was to test pinhole defects in one cell of the fuel cell stack. The results revealed that one artificial pinhole could not create significant results that differentiated from what has been observed in prior experiments. In an attempt to see the effects pinholes in membrane electrode assemblies represented in data, an MEA with sixteen pinholes was placed into the PEMFC stack. However, problems with the hydrogen supply limited invalidated the data from this experiment and another experiment was not possible before the conclusion of this report. Further consideration for realistic pinhole defect simulation and positioning in an MEA or across MEAs in a stack could be applied.

The theoretical modeling involved in this project was in relation to polarization curves and data from EIS. To intertwine the two models, the data from a fuel cell run was utilized and matched to the polarization curve. The experimental data fit well to the polarization curve and only begins to stray at higher current densities. The charge transfer resistances from the EIS data were also compared, with the cathode values trending the same as theoretical model and the anode values not fitting very well. The experimental anode values here are largely misrepresented because of the assumptions and uncertainty of the EIS fitting and polarization curve model. The anode charge transfer is modeled in EIS off of a portion of the Nyquist plot that is dominated by the cathode resistances. Since the kinetics of the hydrogen oxidation reaction are much faster than the oxygen reduction reaction, the data for the anode is essential represented as a scaled-down version of the cathode resistances. The polarization curve model was adapted to correspond with the experimental data for voltage and cathode charge transfer resistance gathered from the healthy stack. The model predicted future cell voltages reasonably for the first cell in the stack, but not the second or third. The relation did not translate well for the charge transfer resistance. It may be possible to modify one or both of these models to incorporate the theories applied more appropriately.

Overall, experiments conducted at ENSIC in Nancy, France, were successful. Interpretation of the data collected can be used as a model for further research. Although experiments on the defective stack were terminated, modified experimental procedures may be conducted to analyze degradation patterns in a defective stack.

References

Asghari, S, Mokmeli, A., & Samavati, M. (2010). Study of PEM fuel cell performance by electrochemical impedance spectroscopy. *International Journal of Hydrogen Energy*, *2010*(35), 9289-9290.

Baker, R., & Zhang, J. (April 2011). Electrochemistry Encyclopedia: PEM fuel cells. YCES – Case Western Reserve University. Retrieved February 2, 2012, from http://electrochem.cwru.edu/encycl/art-f04-fuel-cells-pem.htm

Borup, R. L., Davey, J. R., Garzon, F. H., Wood, D. L., Inbody, M. A. PEM fuel cell electrocatalyst durability measurements. Journal of Power Sources 164 (2006) pp. 76-81.

Choi, E., Halder, P., & Datta, R. (2006). Proton-exchange membrane fuel cells In *Encylopedia of Chemical Processing* (pp. 2501-2528). New York: Taylor & Francis

Choi, E., & Moss, J. A. (2009). *Observation of a polymer electrolyte membrane fuel cell degradation under dynamic load cycling*. Informally published manuscript, Worcester Polytechnic Institute, Worcester, MA.

Datta, R. personal communication. 2012

Datta, R. (2011). *PEM fuel cell/DMFC principles*.

Dhaunshkodi, S. R. (2010). *Proton exchange membrane fuel cells*. Boca Raton: Taylor & Francis Group.

Emerson, A., & Montville, L. (2010). *Electrochemical characterization and water balance of a PEM fuel cell.* Informally published manuscript,Worcester Polytechnic Institute, Worcester, MA.

Genova-Dimitrova, P., Baradie, B., Foscallo, D., Poinsignon, C., & Sanchez, J. (2001).

Ionomeric membranes for proton exchange membrane fuel cell (PEMFC): sulfonated polysulfone associated with phosphatoantimonic acid. Journal of Membrane Science, 185(1), 59–71.

Gu, Y., St.Pierre, J., Joly, A., Goeke, R., Datye, A., & Atanassov, P. (2009). Aging studies of pt/glassy carbon model electrocatalysts. *Journal of The Electrochemical Society*, *156*(4), B4485-B492. doi: 10.1149/1.3077608

Han, M., Xu, J.H., Chan, S.H., Jiang, S.P. (2008). Characterization of has diffusion layers of PEMFC. Electrochemica Acta (53), 5361-5367.

Huang, B. personal communication. 2012

Lapique, F. personal communicatin. 2012

Larminie, J., & Dicks, A. (2003). *Fuel cell systems explained*. West Sussex: John Wiley & Sons.

Lee, S. J., Mukerjee, S., McBreen, J., Rho, Y., Kho, Y., & Lee, T. (1998). Effects of Nafion impregnation on performances of PEMFC electrodes. Electrochimica Acta, 43(24), 3693-3701.

Lu, W., Liu, Z., Wang, C., Mao, Z., Zhang, M. (2011). The effects of pinholes on proton exchange membrane fuel cell performance. International Journal of Energy Research (35), 24-30.

Luo, Z., Li, D., Tang, H., Pan, M., Ruan, R. (2006). Degradation behavior of membrane electrode-assembly materials in 10-cell PEMFC stack. International Journal of Hydrogen Energy (31), 1831-1837.

McDonald, R., Mittelsteadt, C., & Thompson, E. (2004). Effects of Deep Temperature Cycling on Nafion® 112 Membranes and Membrane Electrode Assemblies. Fuel Cells, 4(3), 208-213.

Mekhielf, S., Saidur, R., & Safari, A. (2011). Comparative study of different fuel cells.

"SGL Technologies GmbH - SIGRACET® GDL - Optimized Gas Diffusion Layers for All Fuel Cells." *Fuel Cell Markets - Fuel Cell and Hydrogen Products*. Web. 17 Feb. 2012. <http://www.fuelcellmarkets.com/products_and_services/3,1,617,17,28418.html?subsite=617&language=1>.

Schiraldi, D. Perfluorinated Polymer Electrolyte Membrane Durability. *Journal of* Macromolecular Science, 46(2006), 315-327.

Scribner Associates. (2011). *Electrochemical impedance spectroscopy (eis)*. Retrieved from http://www.scribner.com/files/tech-papers/Scribner Associates - Electrochemical Impedance Spectroscopy for Fuel Cell Research.pdf

Spendelow, J., & Marcinkoski, J. (2009, October 7). Fuel Cell System Cost - 2009. DOE Hydrogen Program Record. Retrieved February 8, 2012, from www.hydrogen.energy.gov/pdfs/9012_fuel_cell_system_cost.pdf

Srinivasan, S. (2006). *Fuel cells*. (pp. 3-25). New York: Springer Science. *Renewable and Sustainable Energy Reviews*, *16*(2012), 981-989.

Thampan, T., Malhotra, S., Zhang, J., & Datta, R. (2001). PEM fuel cell as a membrane reactor. *Catalysis Today*, *67*(2001), 15-32.

Vilekar, S., & Datta, R. (2009). The effect of hydrogen crossover on open-circuit voltage in polymer electrolyte membrane fuel cells. *Journal of Power Sources*, *185*(2010), 2241-2247.

Wang, X., Huang, Y., Cheng, C., & Jang, J. (2009). Flow field optimization for proton exchange membrane fuel cells with varying channel heights and widths. Electrochimica Acta, 54, 5522-5530.

Wu, J., Yuan, X., Wang, H., Blanco, M., Martin, J., & Zhang, J. (2008). Diagnostic tools in PEM fuel cell research: Part I electrochemical techniques. *International Journal of Hydrogen Energy*, *33*(2008a), 1735-1746.

Wu, J., Yuan, X., Martin, J., Wan, J., Zhang, J., Shen, J., Wu, S., Merida, W.. A review of PEM fuel cell durability: Degradation mechanisms and mitigation strategies. Journal of Power Sources 184 (2008b). pp 104-119. June 11th, 2008. Accessed January 18th, 2011.

Xie,T. & Hayden, C.A. (2007). A kinetic model for the chemical degradation of perfluorinated sulfonic acid ionomers : weak end groups versus side chain cleavage. Polymer (48), 5497-5506.

Yuan, X., Song, C., Wang, H., & Zhang, J. (2010).*Electrochemical impedance spectroscopy in PEM fuel cells*. Springer: Springer-Verlag London Limited.

Zhang, J., Yuan, X., Wang, H., & Sun, J. (2007). Ac impedance techniques in PEM fuel cells diagnostics: A review. *International Journal of Hydrogen Energy*, *32*(2007), 4365-4380.

Appendix A: Sample Calculations

Water Balance (Data collected from 01/08/2012)

$$\mathrm{F_{H_2cons}} = \frac{\mathrm{I}}{2\mathrm{F}} = \frac{30\ \mathrm{A}}{2 \times 96485\,\frac{couloumbs}{mol}} = 1.55 \times 10^{-4}\,\frac{\mathrm{mol}}{\mathrm{s}}$$

$$\rightarrow \mathrm{F_{H_2in}} = \lambda \mathrm{F_{H_2cons}} = 1.5 \times \left(1.55 * 10^{-4}\,\frac{\mathrm{mol}}{\mathrm{s}}\right) = 2.33 \times 10^{-4}\,\frac{\mathrm{mol}}{\mathrm{s}}$$

$$\mathrm{F_{H_2OutA}} = \mathrm{F_{H_2in}} \times \left[1 - \left(\frac{1}{\lambda}\right)\right] = \left(2.33 \times 10^{-4}\,\frac{\mathrm{mol}}{\mathrm{s}}\right) \times \left[1 - \left(\frac{1}{1.5}\right)\right]$$

$$\mathrm{F_{H_2O\ liq\ out\ A}} = \left(\frac{1\ \mathrm{mol\ water}}{18.01\ g}\right) \times \left(\frac{\mathrm{Mass_{beaker+water}} - \mathrm{Mass_{beaker}}}{time}\right)$$

$$= \left(\frac{1\ \mathrm{mol\ water}}{18.01\ g}\right) \times \left(\frac{445.78\ g - 264.12\ g}{91320\ s}\right) = 3.68 \times 10^{-5}\,\frac{mol}{s}$$

$$\mathrm{y_{H_2O\ A}}(\mathrm{at}\ P_{Total} = 1\ \mathrm{atm}) = \mathrm{P_{A\ H_2O}}(\mathrm{atm})$$

$$= \exp\left[11.6703 - \frac{3816.44}{(273.15\ \mathrm{K} + 20.4^{\mathrm{o}}C) - 46.13}\right] = 0.0234$$

$$\mathrm{F_{H_2O\ vap\ out\ A}} = \frac{\mathrm{y_{H_2OA}}(\mathrm{F_{H_2OutA}})}{1 - \mathrm{y_{H_2OA}}} = \frac{0.0234 \times \left(7.77 \times 10^{-5}\,\frac{mol}{s}\right)}{1 - 0.0234} = 1.86 \times 10^{-6}\,\frac{mol}{s}$$

$$\mathrm{F_{O_2cons}} = \frac{\mathrm{I}}{4\mathrm{F}} = \frac{30\ \mathrm{A}}{4 \times 96485\,\frac{couloumbs}{mol}} = 7.77 \times 10^{-5}\,\frac{mol}{s}$$

$$\rightarrow\ \mathrm{F_{O_2in}} = \lambda \mathrm{F_{O_2cons}} \quad = 3 \times \left(7.77 \times 10^{-5}\,\frac{mol}{s}\right)\ = 2.33 \times 10^{-4}\,\frac{\mathrm{mol}}{\mathrm{s}}$$

$$\mathrm{F_{H_2O\ liq\ out\ C}} = \left(\frac{1\ \mathrm{mol\ water}}{18.01\ g}\right) \times \left(\frac{\mathrm{Mass_{beaker+water}} - \mathrm{Mass_{beaker}}}{time}\right)$$

$$= \left(\frac{1\ \mathrm{mol\ water}}{18.01\ g}\right) \times \left(\frac{1447.6\ g - 377.9\ g}{91320\ s}\right) = 2.17 \times 10^{-4}\,\frac{mol}{s}$$

$$\mathrm{F}_{\mathrm{Air\ In\ C}} = \frac{\mathrm{F}_{\mathrm{O_2 in}}}{\mathrm{y}_{\mathrm{O_2 C}}} = \frac{2.33 \times 10^{-4}\,\frac{\mathrm{mol}}{\mathrm{s}}}{0.21} = 1.11 \times 10^{-3}\,\frac{mol}{s}$$

$$\mathrm{y}_{\mathrm{H_2O\ in\ C}}(@\ P_{Total} = 1\ \mathrm{atm}) = \mathrm{P}_{\mathrm{A\ H_2O}}(\mathrm{atm})$$

$$= \exp\left[11.6703 - \frac{3816.44}{(273.15\ \mathrm{K} + 45.4^{\mathrm{o}}C) - 46.13}\right] = 0.0964$$

$$\mathrm{F}_{\mathrm{H_2O\ vap\ in\ C}} = \frac{\mathrm{y}_{\mathrm{H_2O\ C}}(\mathrm{F}_{\mathrm{Air\ In\ C}})}{1 - \mathrm{y}_{\mathrm{H_2O\ C}}} = \frac{0.0964 \times \left(1.11 \times 10^{-3}\,\frac{mol}{s}\right)}{1 - 0.0964} = 1.18 \times 10^{-4}\,\frac{mol}{s}$$

$$\mathrm{y}_{\mathrm{H_2O\ Out\ C}}(\mathrm{at}\ P_{Total} = 1\ \mathrm{atm}) = \mathrm{P}_{\mathrm{A\ H_2O}}(\mathrm{atm})$$

$$= \exp\left[11.6703 - \frac{3816.44}{(273.15\ \mathrm{K} + 16.5^{\mathrm{o}}C) - 46.13}\right] = 0.0183$$

$$\mathrm{F}_{\mathrm{Air\ Out\ C}} = \mathrm{F}_{\mathrm{N_2\ Out\ C}} + \mathrm{F}_{\mathrm{O_2\ Out\ C}}$$

$$\mathrm{F}_{\mathrm{N_2\ Out\ C}} = \mathrm{F}_{\mathrm{N_2\ In\ C}} = \mathrm{y}_{\mathrm{N_2 In\ C}} \times \mathrm{F}_{\mathrm{Air\ In\ C}} = 0.79 \times \left(1.11 \times 10^{-3}\,\frac{mol}{s}\right) = 8.77 \times 10^{-4}\,\frac{mol}{s}$$

$$\mathrm{F}_{\mathrm{O_2\ Out\ C}} = \mathrm{F}_{\mathrm{O_2 in}} \times \left[1 - \left(\frac{1}{\lambda}\right)\right] = \left(2.33 \times 10^{-4}\,\frac{\mathrm{mol}}{\mathrm{s}}\right) \times \left[1 - \left(\frac{1}{3}\right)\right] = 1.55 \times 10^{-4}\,\frac{mol}{s}$$

$$\rightarrow \mathrm{F}_{\mathrm{Air\ Out\ C}} = 8.77 \times 10^{-4}\,\frac{mol}{s} + 1.55 \times 10^{-4}\,\frac{mol}{s} = 1.03 \times 10^{-3}\,\frac{mol}{s}$$

$$\mathrm{F}_{\mathrm{H_2O\ vap\ out\ C}} = \frac{\mathrm{y}_{\mathrm{H_2O\ C}}(\mathrm{F}_{\mathrm{Air\ Out\ C}})}{1 - \mathrm{y}_{\mathrm{H_2O\ C}}} = \frac{0.0183 \times \left(1.03 \times 10^{-3}\,\frac{mol}{s}\right)}{1 - 0.0183} = 1.92 \times 10^{-5}\,\frac{mol}{s}$$

$$\mathrm{F}_{\mathrm{H_2O\ prod}} = \frac{\mathrm{I}}{2\mathrm{F}} = \frac{30\ \mathrm{A}}{2 \times 96485\,\frac{couloumbs}{mol}} = 1.55 \times 10^{-4}\,\frac{\mathrm{mol}}{\mathrm{s}}$$

$$\alpha = \frac{\mathrm{F}_{\mathrm{H_2O\ out\ total\ A}}}{\mathrm{F}_{\mathrm{H_2O\ Produced}}} = \frac{\mathrm{F}_{\mathrm{H_2O\ vap\ out\ A}} + \mathrm{F}_{\mathrm{H_2O\ liq\ out\ A}}}{\mathrm{F}_{\mathrm{H_2O\ Produced}}} = \frac{1.86 \times 10^{-6}\frac{mol}{s} + 3.68 \times 10^{-5}\frac{mol}{s}}{1.55 \times 10^{-4}\frac{\mathrm{mol}}{\mathrm{s}}} = 0.249$$

$$W = \frac{F_{H_2O\text{ out}}}{F_{H_2O\text{ vap in C}}} = \frac{F_{H_2O\text{ vap out A}} + F_{H_2O\text{ liq out A}} + F_{H_2O\text{ vap out C}} + F_{H_2O\text{ liq out C}}}{F_{H_2O\text{ vap in C}}} =$$

$$\frac{1.86\times10^{-6}\frac{mol}{s} + 3.68\times10^{-5}\frac{mol}{s} + 1.92\times10^{-5}\frac{mol}{s} + 2.17\times10^{-4}\frac{mol}{s}}{1.18\times10^{-4}\frac{mol}{s}} = 2.32$$

Theoretical Modeling

$$\mathrm{V} = \mathrm{V_0} + \eta_\mathrm{A} - \eta_\mathrm{c} + \eta_\mathrm{EL} + \eta_\mathrm{I}$$

$$\mathrm{p_w} = \exp\left(11.6703 - \frac{3816.44}{(273.15 + 55) - 46.13}\right)$$

$$\mathrm{p_{H_2}} = 1(1 - \mathrm{p_w}) = .845\ atm$$

$$\mathrm{p_{O_2}} = 0.21(1 - \mathrm{p_w}) = .177\ atm$$

$$V_0 = 1.229 - 8.46 \times 10^{-4}(\mathrm{T} - 298) + \frac{\mathrm{RT}}{4\mathrm{F}} ln\left(\mathrm{p_{H_2}^2 p_{O_2}}\right) = 1.19\mathrm{V}$$

Anode:

$$0.45 \times 10^{-3} = M_{PT}y + M_{RU}y = 195.084y + 101.7y$$

$$y = 1.519 \times 10^{-6}$$

$$M_{PT}y = .225 \times 10^{-6} = m_M$$

$$\gamma_\mathrm{mA} = 0.95(.000225)\frac{6}{21.45(5.6 \times 10^{-7})} = 106.8$$

$$\mathrm{i_{A0}} = 135.1\left(\frac{.845}{1}\right)\exp\left\{-\frac{34600}{\mathrm{R}}\left(\frac{1}{328} - \frac{1}{298}\right)\right\} 3.0 \times 10^{-3} = .972$$

$$\eta_\mathrm{a} = \frac{\mathrm{R} * 328}{.5 * 1\mathrm{F}}\sinh^{-1}\left[\frac{1}{2}\left\{\frac{\mathrm{i}/1.23}{1 - \mathrm{i}/4}\right\}\right]$$

Cathode:

$$\gamma_\mathrm{mC} = 0.95(.0004)\frac{6}{21.45(3.2 \times 10^{-7})} = 332.4$$

$$\mathrm{i_{C0}} = 332.4\left(\frac{.845}{1}\right)\exp\left\{-\frac{67000}{\mathrm{R}}\left(\frac{1}{328} - \frac{1}{298}\right)\right\} 1 \times 10^{-10} = 7 \times 10^{-8}$$

$$\mathrm{K_H} = 6.61 \times 10^{-8}\exp\left(-\frac{21030}{R328}\right)$$

$$\mathrm{i_{C,x}} = \frac{2FK_HP_H}{L_{EL}} = \frac{2F2.95 \times 10^{-11}.845}{.0018} = 2.68 \times 10^{-3}$$

$$\mathrm{\eta_c} = \frac{\mathrm{RT}}{.5 * -2\mathrm{F}} \sinh^{-1}\left[\frac{1}{2}\left\{\frac{(\mathrm{i} + \mathrm{i_{C,x}})/\mathrm{i_{C,0}}}{1 - (\mathrm{i} + \mathrm{i_{C,x}})/\mathrm{i_{C,L}}}\right\}\right]$$

Electrolyte

$$\mathrm{\eta_{EL}} = \mathrm{i}\left(\frac{\mathrm{L_{EL}}}{\mathrm{\sigma_{EL}}}\right)$$

$$\lambda = 14$$

$$\epsilon_B = \frac{\lambda}{\frac{537}{18} + \lambda} \quad \epsilon_o = 0.7$$

$$\mathrm{X} = \frac{1.8}{\frac{537}{18} + 1.8}$$

$$C_{HO} = \frac{1}{18\lambda}$$

$$K_A = 6.2 \exp\left(\frac{52300}{R}\left(\frac{1}{328} - \frac{1}{298}\right)\right)$$

$$\beta = \frac{\lambda + 1 - \sqrt{(\lambda + 1)^2 - 4\lambda\left(1 - \frac{1}{K_A}\right)}}{2\left(1 - \frac{1}{K_A}\right)}$$

$$\sigma_{EL} = (\epsilon o(\epsilon_B - \chi))^{1.5}\left(\frac{349.8}{1 + 5.5}\right)\exp\left(-\frac{14000}{R}\left(\frac{1}{328} - \frac{1}{298}\right)\right)C_{H_2O}\beta = 0.026$$

$$\mathrm{V} = \mathrm{V_0} - \frac{\mathrm{RT}}{\mathrm{\alpha_A^*\,\nu^{\,*}_{Ae-}F}} \sinh^{-1}\left[\frac{1}{2}\left\{\frac{\mathrm{i_A}/\mathrm{i_{A,0}}}{1 - \mathrm{i_A}/\mathrm{i_{A,L}}}\right\}\right] + \frac{\mathrm{RT}}{\mathrm{\alpha_C^*\,\nu^{\,*}_{Ce-}F}} \sinh^{-1}\left[\frac{1}{2}\left\{\frac{(\mathrm{i_C} + \mathrm{i_{C,x}})/\mathrm{i_{C,0}}}{1 - (\mathrm{i_C} + \mathrm{i_{C,x}})/\mathrm{i_{C,L}}}\right\}\right] - \mathrm{i_{EL}}\left(\frac{\mathrm{L_{EL}}}{\mathrm{\sigma_{EL}}}\right) - \mathrm{i(Ri)}$$

Resistances

$$R_A = \frac{\mathrm{RT}}{\left(2\alpha_A^* \, \nu^{\,*}_{Ae-} F i_{A,0}\right)(1 - i/i_{A,L})^2 \sqrt{1 + \frac{1}{4}\left\{\frac{i/i_{A,0}}{1 - i/i_{A,L}}\right\}^2}}$$

$$R_C = \frac{RT}{\left(2\alpha_C^* \, \nu^{\,*}_{Ce-} F i_{C,0}\right)(1 - i/i_{C,L})^2 \sqrt{1 + \frac{1}{4}\left\{\frac{i/i_{C,0}}{1 - i/i_{C,L}}\right\}^2}}$$

$$R_{EL} = \frac{L_E}{\sigma_{EL}} = 0.6886$$

Appendix B: Healthy Stack EIS Data

Stack

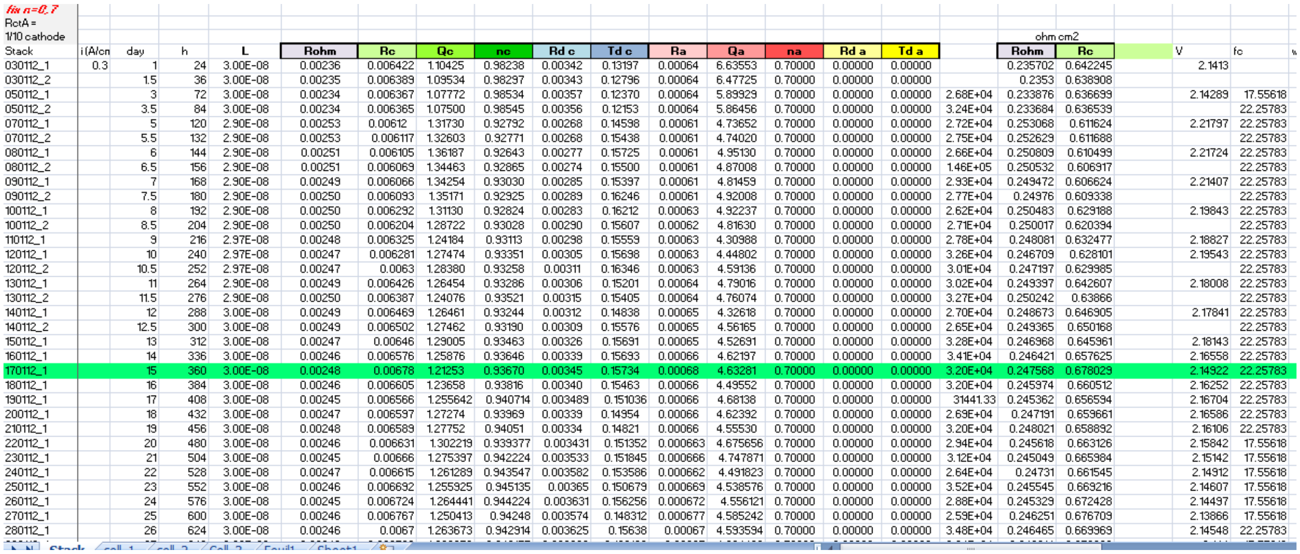

fix n=0.7
RctA =
1/10 cathode

																	ohm cm2				
Stack	i (A/cm	day	h	L	**Rohm**	**Rc**	**Qc**	**nc**	**Rd c**	**Td c**	**Ra**	**Qa**	**na**	**Rd a**	**Td a**		**Rohm**	**Rc**		V	fc
030112_1	0.3	1	24	3.00E-08	0.00236	0.006422	1.10425	0.98238	0.00342	0.13197	0.00064	6.63553	0.70000	0.00000	0.00000		0.235702	0.642245		2.1413	
030112_2		1.5	36	3.00E-08	0.00235	0.006389	1.09534	0.98297	0.00343	0.12796	0.00064	6.47725	0.70000	0.00000	0.00000		0.2353	0.638908			
050112_1		3	72	3.00E-08	0.00234	0.006367	1.07772	0.98534	0.00357	0.12370	0.00064	5.89929	0.70000	0.00000	0.00000	2.68E+04	0.233876	0.636699		2.14289	17.55618
050112_2		3.5	84	3.00E-08	0.00234	0.006365	1.07500	0.98545	0.00356	0.12153	0.00064	5.86456	0.70000	0.00000	0.00000	3.24E+04	0.233684	0.636539			22.25783
070112_1		5	120	2.90E-08	0.00253	0.00612	1.31730	0.92792	0.00268	0.14598	0.00061	4.73652	0.70000	0.00000	0.00000	2.72E+04	0.253068	0.611624		2.21797	22.25783
070112_2		5.5	132	2.90E-08	0.00253	0.006117	1.32603	0.92771	0.00268	0.15438	0.00061	4.74020	0.70000	0.00000	0.00000	2.75E+04	0.252629	0.611688			22.25783
080112_1		6	144	2.90E-08	0.00251	0.006105	1.36187	0.92643	0.00277	0.15725	0.00061	4.95130	0.70000	0.00000	0.00000	2.66E+04	0.250809	0.610499		2.21724	22.25783
080112_2		6.5	156	2.90E-08	0.00251	0.006069	1.34463	0.92865	0.00274	0.15500	0.00061	4.87008	0.70000	0.00000	0.00000	1.46E+05	0.250532	0.606917			22.25783
090112_1		7	168	2.90E-08	0.00249	0.006066	1.34254	0.93030	0.00285	0.15397	0.00061	4.81459	0.70000	0.00000	0.00000	2.93E+04	0.249472	0.606624		2.21407	22.25783
090112_2		7.5	180	2.90E-08	0.00250	0.006093	1.35171	0.92925	0.00289	0.16246	0.00061	4.92008	0.70000	0.00000	0.00000	2.77E+04	0.24976	0.609338			22.25783
100112_1		8	192	2.90E-08	0.00250	0.006292	1.31130	0.92824	0.00283	0.16212	0.00063	4.92237	0.70000	0.00000	0.00000	2.62E+04	0.250483	0.629188		2.19843	22.25783
100112_2		8.5	204	2.90E-08	0.00250	0.006204	1.28722	0.93028	0.00290	0.15607	0.00062	4.81630	0.70000	0.00000	0.00000	2.71E+04	0.250017	0.620394			22.25783
110112_1		9	216	2.97E-08	0.00248	0.006325	1.24184	0.93113	0.00298	0.15559	0.00063	4.30988	0.70000	0.00000	0.00000	2.78E+04	0.248081	0.632477		2.18827	22.25783
120112_1		10	240	2.97E-08	0.00247	0.006281	1.27474	0.93351	0.00305	0.15698	0.00063	4.44802	0.70000	0.00000	0.00000	3.26E+04	0.246709	0.628101		2.19543	22.25783
120112_2		10.5	252	2.97E-08	0.00247	0.0063	1.28380	0.93258	0.00311	0.16346	0.00063	4.59136	0.70000	0.00000	0.00000	3.01E+04	0.247197	0.629985			22.25783
130112_1		11	264	2.90E-08	0.00249	0.006426	1.26454	0.93286	0.00306	0.15201	0.00064	4.79016	0.70000	0.00000	0.00000	3.02E+04	0.249397	0.642607		2.18008	22.25783
130112_2		11.5	276	2.90E-08	0.00250	0.006387	1.24076	0.93521	0.00315	0.15405	0.00064	4.76074	0.70000	0.00000	0.00000	3.27E+04	0.250242	0.63866			22.25783
140112_1		12	288	3.00E-08	0.00249	0.006469	1.26461	0.93244	0.00312	0.14838	0.00065	4.32618	0.70000	0.00000	0.00000	2.70E+04	0.248673	0.646905		2.17841	22.25783
140112_2		12.5	300	3.00E-08	0.00249	0.006502	1.27462	0.93190	0.00309	0.15576	0.00065	4.56165	0.70000	0.00000	0.00000	2.65E+04	0.249365	0.650168			22.25783
150112_1		13	312	3.00E-08	0.00247	0.00646	1.29005	0.93463	0.00326	0.15691	0.00065	4.52691	0.70000	0.00000	0.00000	3.28E+04	0.246968	0.645961		2.18143	22.25783
160112_1		14	336	3.00E-08	0.00246	0.006576	1.25876	0.93646	0.00339	0.15693	0.00066	4.62197	0.70000	0.00000	0.00000	3.41E+04	0.246421	0.657625		2.16558	22.25783
170112_1		15	360	3.00E-08	0.00248	0.00678	1.21253	0.93670	0.00345	0.15734	0.00068	4.63281	0.70000	0.00000	0.00000	3.20E+04	0.247568	0.678029		2.14922	22.25783
180112_1		16	384	3.00E-08	0.00246	0.006605	1.23658	0.93816	0.00340	0.15463	0.00066	4.49552	0.70000	0.00000	0.00000	3.20E+04	0.245974	0.660512		2.16252	22.25783
190112_1		17	408	3.00E-08	0.00245	0.006566	1.255642	0.940714	0.003489	0.151036	0.00066	4.68138	0.70000	0.00000	0.00000	31441.33	0.245362	0.656594		2.16704	22.25783
200112_1		18	432	3.00E-08	0.00247	0.006597	1.27274	0.93969	0.00339	0.14954	0.00066	4.62392	0.70000	0.00000	0.00000	2.69E+04	0.247191	0.659661		2.16586	22.25783
210112_1		19	456	3.00E-08	0.00248	0.006589	1.27752	0.94051	0.00334	0.14821	0.00066	4.55530	0.70000	0.00000	0.00000	3.20E+04	0.248021	0.658892		2.16106	22.25783
220112_1		20	480	3.00E-08	0.00246	0.006631	1.302219	0.939377	0.003431	0.151352	0.000663	4.675656	0.70000	0.00000	0.00000	2.94E+04	0.245618	0.663126		2.15842	17.55618
230112_1		21	504	3.00E-08	0.00245	0.00666	1.275397	0.942224	0.003533	0.151845	0.000666	4.747871	0.70000	0.00000	0.00000	3.12E+04	0.245049	0.665984		2.15142	17.55618
240112_1		22	528	3.00E-08	0.00247	0.006615	1.261289	0.943547	0.003582	0.153586	0.000662	4.491823	0.70000	0.00000	0.00000	2.64E+04	0.24731	0.661545		2.14912	17.55618
250112_1		23	552	3.00E-08	0.00246	0.006692	1.255925	0.945135	0.00365	0.150679	0.000669	4.538576	0.70000	0.00000	0.00000	3.52E+04	0.245545	0.669216		2.14607	17.55618
260112_1		24	576	3.00E-08	0.00245	0.006724	1.264441	0.944224	0.003631	0.156256	0.000672	4.556121	0.70000	0.00000	0.00000	2.88E+04	0.245329	0.672428		2.14497	17.55618
270112_1		25	600	3.00E-08	0.00246	0.006767	1.250413	0.94248	0.003574	0.148312	0.000677	4.585242	0.70000	0.00000	0.00000	2.59E+04	0.246251	0.676709		2.13866	17.55618
280112_1		26	624	3.00E-08	0.00246	0.0067	1.263673	0.942914	0.003625	0.15638	0.00067	4.593594	0.70000	0.00000	0.00000	3.48E+04	0.246465	0.669969		2.14548	22.25783

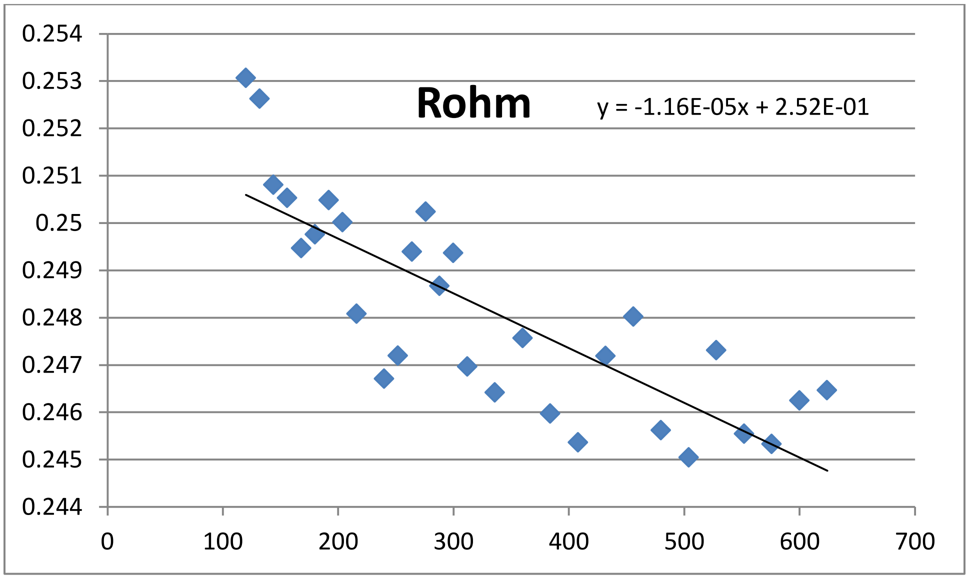

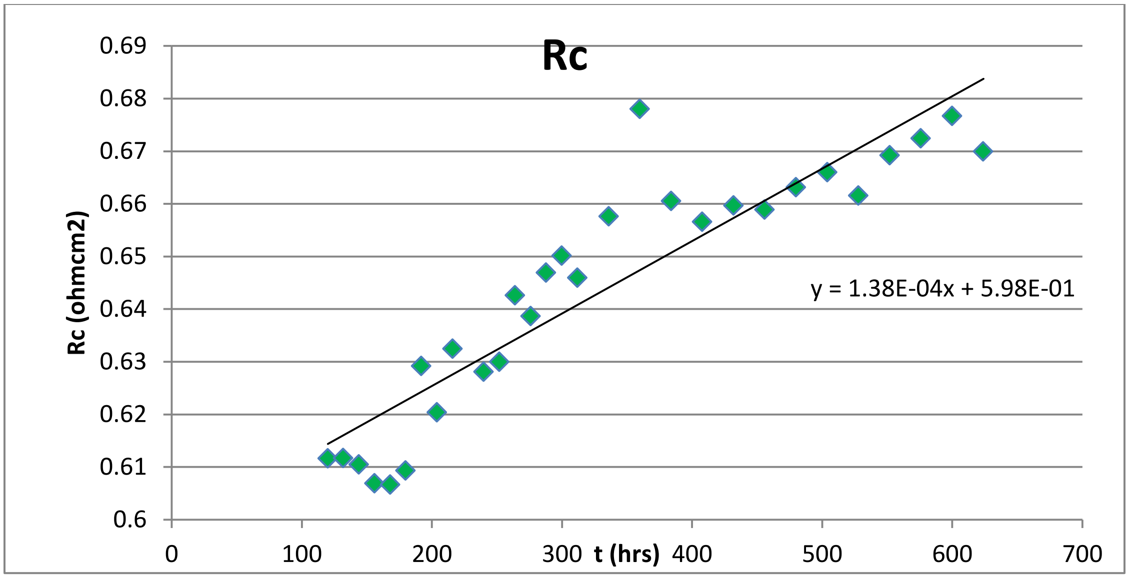

Cell 1

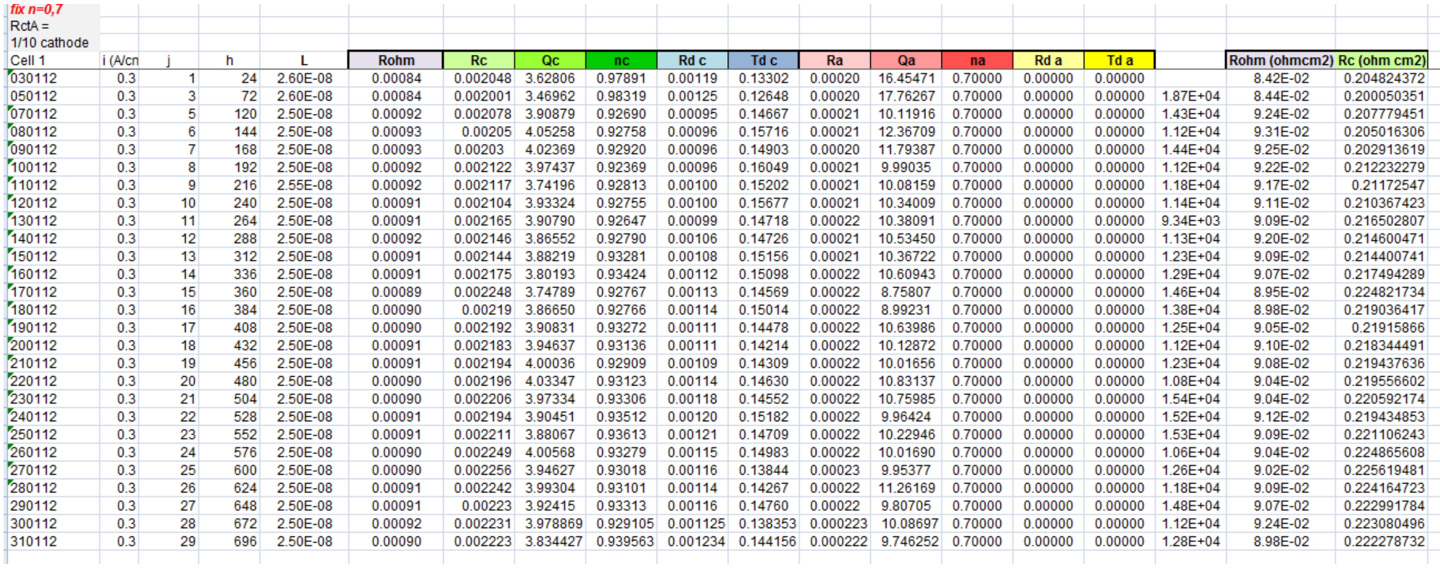

fix n=0,7
RctA =
1/10 cathode

Cell 1	i (A/cn	j	h	L	Rohm	Rc	Qc	nc	Rd c	Td c	Ra	Qa	na	Rd a	Td a		Rohm (ohmcm2)	Rc (ohm cm2)
030112	0.3	1	24	2.60E-08	0.00084	0.002048	3.62806	0.97891	0.00119	0.13302	0.00020	16.45471	0.70000	0.00000	0.00000		8.42E-02	0.204824372
050112	0.3	3	72	2.60E-08	0.00084	0.002001	3.46962	0.98319	0.00125	0.12648	0.00020	17.76267	0.70000	0.00000	0.00000	1.87E+04	8.44E-02	0.200050351
070112	0.3	5	120	2.50E-08	0.00092	0.002078	3.90879	0.92690	0.00095	0.14667	0.00021	10.11916	0.70000	0.00000	0.00000	1.43E+04	9.24E-02	0.207779451
080112	0.3	6	144	2.50E-08	0.00093	0.00205	4.05258	0.92758	0.00096	0.15716	0.00021	12.36709	0.70000	0.00000	0.00000	1.12E+04	9.31E-02	0.205016306
090112	0.3	7	168	2.50E-08	0.00093	0.00203	4.02369	0.92920	0.00096	0.14903	0.00020	11.79387	0.70000	0.00000	0.00000	1.44E+04	9.25E-02	0.202913619
100112	0.3	8	192	2.50E-08	0.00092	0.002122	3.97437	0.92369	0.00096	0.16049	0.00021	9.99035	0.70000	0.00000	0.00000	1.12E+04	9.22E-02	0.212232279
110112	0.3	9	216	2.55E-08	0.00092	0.002117	3.74196	0.92813	0.00100	0.15202	0.00021	10.08159	0.70000	0.00000	0.00000	1.18E+04	9.17E-02	0.21172547
120112	0.3	10	240	2.50E-08	0.00091	0.002104	3.93324	0.92755	0.00100	0.15677	0.00021	10.34009	0.70000	0.00000	0.00000	1.14E+04	9.11E-02	0.210367423
130112	0.3	11	264	2.50E-08	0.00091	0.002165	3.90790	0.92647	0.00099	0.14718	0.00022	10.38091	0.70000	0.00000	0.00000	9.34E+03	9.09E-02	0.216502807
140112	0.3	12	288	2.50E-08	0.00092	0.002146	3.86552	0.92790	0.00106	0.14726	0.00021	10.53450	0.70000	0.00000	0.00000	1.13E+04	9.20E-02	0.214600471
150112	0.3	13	312	2.50E-08	0.00091	0.002144	3.88219	0.93281	0.00108	0.15156	0.00021	10.36722	0.70000	0.00000	0.00000	1.23E+04	9.09E-02	0.214400741
160112	0.3	14	336	2.50E-08	0.00091	0.002175	3.80193	0.93424	0.00112	0.15098	0.00022	10.60943	0.70000	0.00000	0.00000	1.29E+04	9.07E-02	0.217494289
170112	0.3	15	360	2.50E-08	0.00089	0.002248	3.74789	0.92767	0.00113	0.14569	0.00022	8.75807	0.70000	0.00000	0.00000	1.46E+04	8.95E-02	0.224821734
180112	0.3	16	384	2.50E-08	0.00090	0.00219	3.86650	0.92766	0.00114	0.15014	0.00022	8.99231	0.70000	0.00000	0.00000	1.38E+04	8.98E-02	0.219036417
190112	0.3	17	408	2.50E-08	0.00090	0.002192	3.90831	0.93272	0.00111	0.14478	0.00022	10.63986	0.70000	0.00000	0.00000	1.25E+04	9.05E-02	0.21915866
200112	0.3	18	432	2.50E-08	0.00091	0.002183	3.94637	0.93136	0.00111	0.14214	0.00022	10.12872	0.70000	0.00000	0.00000	1.12E+04	9.10E-02	0.218344491
210112	0.3	19	456	2.50E-08	0.00091	0.002194	4.00036	0.92909	0.00109	0.14309	0.00022	10.01656	0.70000	0.00000	0.00000	1.23E+04	9.08E-02	0.219437636
220112	0.3	20	480	2.50E-08	0.00090	0.002196	4.03347	0.93123	0.00114	0.14630	0.00022	10.83137	0.70000	0.00000	0.00000	1.08E+04	9.04E-02	0.219556602
230112	0.3	21	504	2.50E-08	0.00090	0.002206	3.97334	0.93306	0.00118	0.14552	0.00022	10.75985	0.70000	0.00000	0.00000	1.54E+04	9.04E-02	0.220592174
240112	0.3	22	528	2.50E-08	0.00091	0.002194	3.90451	0.93512	0.00120	0.15182	0.00022	9.96424	0.70000	0.00000	0.00000	1.52E+04	9.12E-02	0.219434853
250112	0.3	23	552	2.50E-08	0.00091	0.002211	3.88067	0.93613	0.00121	0.14709	0.00022	10.22946	0.70000	0.00000	0.00000	1.53E+04	9.09E-02	0.221106243
260112	0.3	24	576	2.50E-08	0.00090	0.002249	4.00568	0.93279	0.00115	0.14983	0.00022	10.01690	0.70000	0.00000	0.00000	1.06E+04	9.04E-02	0.224865608
270112	0.3	25	600	2.50E-08	0.00090	0.002256	3.94627	0.93018	0.00116	0.13844	0.00023	9.95377	0.70000	0.00000	0.00000	1.26E+04	9.02E-02	0.225619481
280112	0.3	26	624	2.50E-08	0.00091	0.002242	3.99304	0.93101	0.00114	0.14267	0.00022	11.26169	0.70000	0.00000	0.00000	1.18E+04	9.09E-02	0.224164723
290112	0.3	27	648	2.50E-08	0.00091	0.00223	3.92415	0.93313	0.00116	0.14760	0.00022	9.80705	0.70000	0.00000	0.00000	1.48E+04	9.07E-02	0.222991784
300112	0.3	28	672	2.50E-08	0.00092	0.002231	3.978869	0.929105	0.001125	0.138353	0.000223	10.08697	0.70000	0.00000	0.00000	1.12E+04	9.24E-02	0.223080496
310112	0.3	29	696	2.50E-08	0.00090	0.002223	3.834427	0.939563	0.001234	0.144156	0.000222	9.746252	0.70000	0.00000	0.00000	1.28E+04	8.98E-02	0.222278732

Cell 2

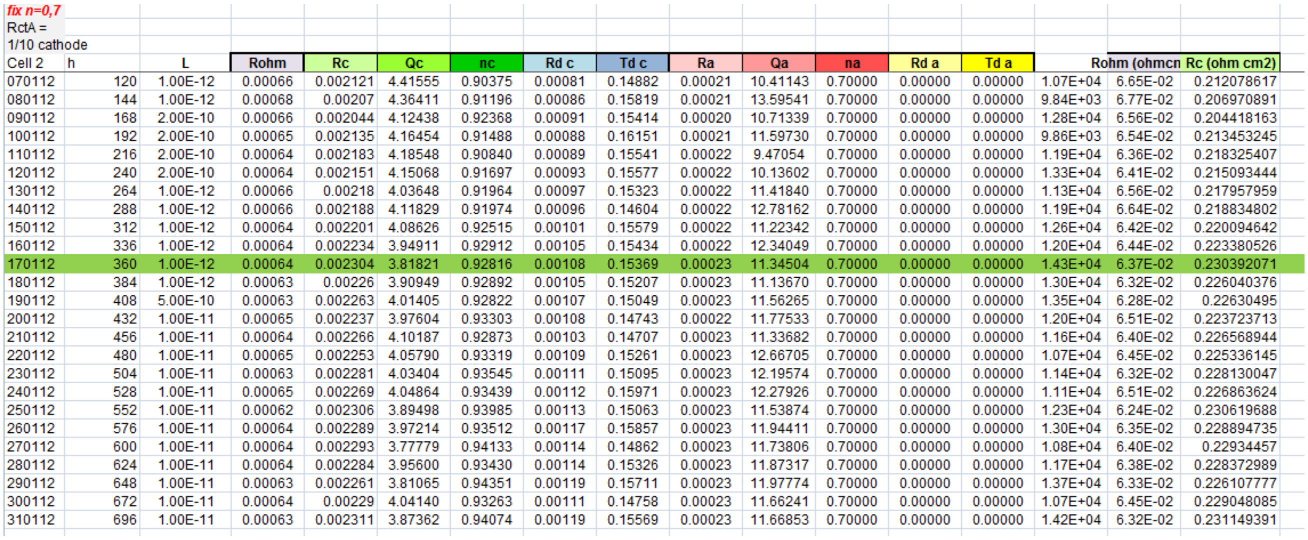

fix n=0,7
RctA =
1/10 cathode

Cell 2	h	L	Rohm	Rc	Qc	nc	Rd c	Td c	Ra	Qa	na	Rd a	Td a		Rohm (ohmcn	Rc (ohm cm2)
070112	120	1.00E-12	0.00066	0.002121	4.41555	0.90375	0.00081	0.14882	0.00021	10.41143	0.70000	0.00000	0.00000	1.07E+04	6.65E-02	0.212078617
080112	144	1.00E-12	0.00068	0.00207	4.36411	0.91196	0.00086	0.15819	0.00021	13.59541	0.70000	0.00000	0.00000	9.84E+03	6.77E-02	0.206970891
090112	168	2.00E-10	0.00066	0.002044	4.12438	0.92368	0.00091	0.15414	0.00020	10.71339	0.70000	0.00000	0.00000	1.28E+04	6.56E-02	0.204418163
100112	192	2.00E-10	0.00065	0.002135	4.16454	0.91488	0.00088	0.16151	0.00021	11.59730	0.70000	0.00000	0.00000	9.86E+03	6.54E-02	0.213453245
110112	216	2.00E-10	0.00064	0.002183	4.18548	0.90840	0.00089	0.15541	0.00022	9.47054	0.70000	0.00000	0.00000	1.19E+04	6.36E-02	0.218325407
120112	240	2.00E-10	0.00064	0.002151	4.15068	0.91697	0.00093	0.15577	0.00022	10.13602	0.70000	0.00000	0.00000	1.33E+04	6.41E-02	0.215093444
130112	264	1.00E-12	0.00066	0.00218	4.03648	0.91964	0.00097	0.15323	0.00022	11.41840	0.70000	0.00000	0.00000	1.13E+04	6.56E-02	0.217957959
140112	288	1.00E-12	0.00066	0.002188	4.11829	0.91974	0.00096	0.14604	0.00022	12.78162	0.70000	0.00000	0.00000	1.19E+04	6.64E-02	0.218834802
150112	312	1.00E-12	0.00064	0.002201	4.08626	0.92515	0.00101	0.15579	0.00022	11.22342	0.70000	0.00000	0.00000	1.26E+04	6.42E-02	0.220094642
160112	336	1.00E-12	0.00064	0.002234	3.94911	0.92912	0.00105	0.15434	0.00022	12.34049	0.70000	0.00000	0.00000	1.20E+04	6.44E-02	0.223380526
170112	360	1.00E-12	0.00064	0.002304	3.81821	0.92816	0.00108	0.15369	0.00023	11.34504	0.70000	0.00000	0.00000	1.43E+04	6.37E-02	0.230392071
180112	384	1.00E-12	0.00063	0.00226	3.90949	0.92892	0.00105	0.15207	0.00023	11.13670	0.70000	0.00000	0.00000	1.30E+04	6.32E-02	0.226040376
190112	408	5.00E-10	0.00063	0.002263	4.01405	0.92822	0.00107	0.15049	0.00023	11.56265	0.70000	0.00000	0.00000	1.35E+04	6.28E-02	0.22630495
200112	432	1.00E-11	0.00065	0.002237	3.97604	0.93303	0.00108	0.14743	0.00022	11.77533	0.70000	0.00000	0.00000	1.20E+04	6.51E-02	0.223723713
210112	456	1.00E-11	0.00064	0.002266	4.10187	0.92873	0.00103	0.14707	0.00023	11.33682	0.70000	0.00000	0.00000	1.16E+04	6.40E-02	0.226568944
220112	480	1.00E-11	0.00065	0.002253	4.05790	0.93319	0.00109	0.15261	0.00023	12.66705	0.70000	0.00000	0.00000	1.07E+04	6.45E-02	0.225336145
230112	504	1.00E-11	0.00063	0.002281	4.03404	0.93545	0.00111	0.15095	0.00023	12.19574	0.70000	0.00000	0.00000	1.14E+04	6.32E-02	0.228130047
240112	528	1.00E-11	0.00065	0.002269	4.04864	0.93439	0.00112	0.15971	0.00023	12.27926	0.70000	0.00000	0.00000	1.11E+04	6.51E-02	0.226863624
250112	552	1.00E-11	0.00062	0.002306	3.89498	0.93985	0.00113	0.15063	0.00023	11.53874	0.70000	0.00000	0.00000	1.23E+04	6.24E-02	0.230619688
260112	576	1.00E-11	0.00064	0.002289	3.97214	0.93512	0.00117	0.15857	0.00023	11.94411	0.70000	0.00000	0.00000	1.30E+04	6.35E-02	0.228894735
270112	600	1.00E-11	0.00064	0.002293	3.77779	0.94133	0.00114	0.14862	0.00023	11.73806	0.70000	0.00000	0.00000	1.08E+04	6.40E-02	0.22934457
280112	624	1.00E-11	0.00064	0.002284	3.95600	0.93430	0.00114	0.15326	0.00023	11.87317	0.70000	0.00000	0.00000	1.17E+04	6.38E-02	0.228372989
290112	648	1.00E-11	0.00063	0.002261	3.81065	0.94351	0.00119	0.15711	0.00023	11.97774	0.70000	0.00000	0.00000	1.37E+04	6.33E-02	0.226107777
300112	672	1.00E-11	0.00064	0.00229	4.04140	0.93263	0.00111	0.14758	0.00023	11.66241	0.70000	0.00000	0.00000	1.07E+04	6.45E-02	0.229048085
310112	696	1.00E-11	0.00063	0.002311	3.87362	0.94074	0.00119	0.15569	0.00023	11.66853	0.70000	0.00000	0.00000	1.42E+04	6.32E-02	0.231149391

Cell 3

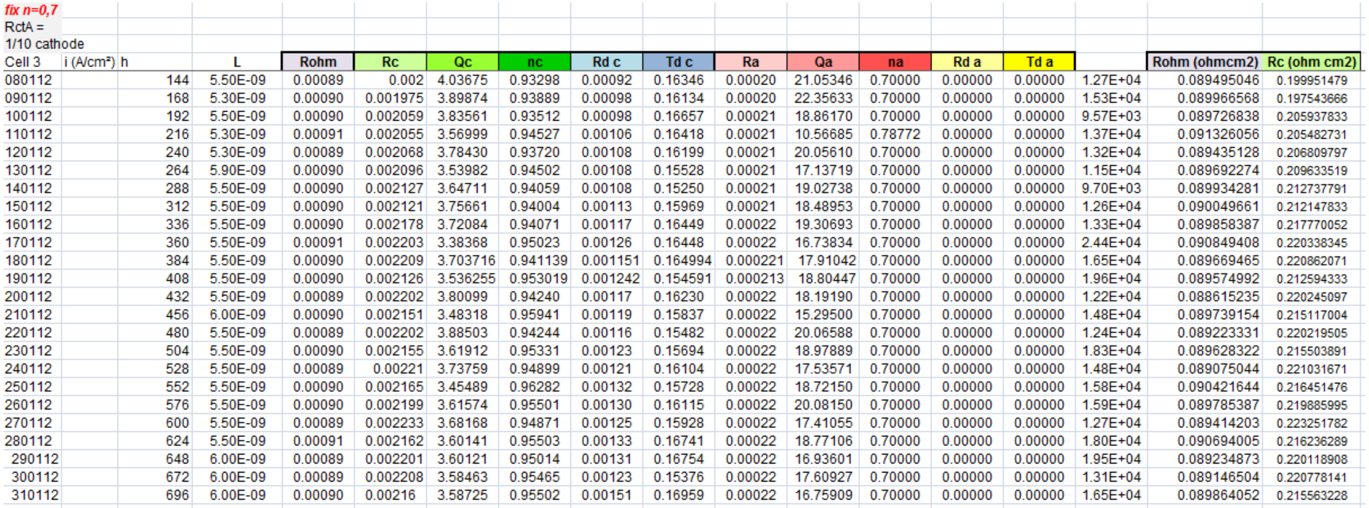

fix n=0,7
RctA =
1/10 cathode

Cell 3	i (A/cm²)	h	L	Rohm	Rc	Qc	nc	Rd c	Td c	Ra	Qa	na	Rd a	Td a		Rohm (ohmcm2)	Rc (ohm cm2)
080112		144	5.50E-09	0.00089	0.002	4.03675	0.93298	0.00092	0.16346	0.00020	21.05346	0.70000	0.00000	0.00000	1.27E+04	0.089495046	0.199951479
090112		168	5.30E-09	0.00090	0.001975	3.89874	0.93889	0.00098	0.16134	0.00020	22.35633	0.70000	0.00000	0.00000	1.53E+04	0.089966568	0.197543666
100112		192	5.50E-09	0.00090	0.002059	3.83561	0.93512	0.00098	0.16657	0.00021	18.86170	0.70000	0.00000	0.00000	9.57E+03	0.089726838	0.205937833
110112		216	5.30E-09	0.00091	0.002055	3.56999	0.94527	0.00106	0.16418	0.00021	10.56685	0.78772	0.00000	0.00000	1.37E+04	0.091326056	0.205482731
120112		240	5.30E-09	0.00089	0.002068	3.78430	0.93720	0.00108	0.16199	0.00021	20.05610	0.70000	0.00000	0.00000	1.32E+04	0.089435128	0.206809797
130112		264	5.90E-09	0.00090	0.002096	3.53982	0.94502	0.00108	0.15528	0.00021	17.13719	0.70000	0.00000	0.00000	1.15E+04	0.089692274	0.209633519
140112		288	5.50E-09	0.00090	0.002127	3.64711	0.94059	0.00108	0.15250	0.00021	19.02738	0.70000	0.00000	0.00000	9.70E+03	0.089934281	0.212737791
150112		312	5.50E-09	0.00090	0.002121	3.75661	0.94004	0.00113	0.15969	0.00021	18.48953	0.70000	0.00000	0.00000	1.26E+04	0.090049661	0.212147833
160112		336	5.50E-09	0.00090	0.002178	3.72084	0.94071	0.00117	0.16449	0.00022	19.30693	0.70000	0.00000	0.00000	1.33E+04	0.089858387	0.217770052
170112		360	5.50E-09	0.00091	0.002203	3.38368	0.95023	0.00126	0.16448	0.00022	16.73834	0.70000	0.00000	0.00000	2.44E+04	0.090849408	0.220338345
180112		384	5.50E-09	0.00090	0.002209	3.703716	0.941139	0.001151	0.164994	0.000221	17.91042	0.70000	0.00000	0.00000	1.65E+04	0.089669465	0.220862071
190112		408	5.50E-09	0.00090	0.002126	3.536255	0.953019	0.001242	0.154591	0.000213	18.80447	0.70000	0.00000	0.00000	1.96E+04	0.089574992	0.212594333
200112		432	5.50E-09	0.00089	0.002202	3.80099	0.94240	0.00117	0.16230	0.00022	18.19190	0.70000	0.00000	0.00000	1.22E+04	0.088615235	0.220245097
210112		456	6.00E-09	0.00090	0.002151	3.48318	0.95941	0.00119	0.15837	0.00022	15.29500	0.70000	0.00000	0.00000	1.48E+04	0.089739154	0.215117004
220112		480	5.50E-09	0.00089	0.002202	3.88503	0.94244	0.00116	0.15482	0.00022	20.06588	0.70000	0.00000	0.00000	1.24E+04	0.089223331	0.220219505
230112		504	5.50E-09	0.00090	0.002155	3.61912	0.95331	0.00123	0.15694	0.00022	18.97889	0.70000	0.00000	0.00000	1.83E+04	0.089628322	0.215503891
240112		528	5.50E-09	0.00089	0.00221	3.73759	0.94899	0.00121	0.16104	0.00022	17.53571	0.70000	0.00000	0.00000	1.48E+04	0.089075044	0.221031671
250112		552	5.50E-09	0.00090	0.002165	3.45489	0.96282	0.00132	0.15728	0.00022	18.72150	0.70000	0.00000	0.00000	1.58E+04	0.090421644	0.216451476
260112		576	5.50E-09	0.00090	0.002199	3.61574	0.95501	0.00130	0.16115	0.00022	20.08150	0.70000	0.00000	0.00000	1.59E+04	0.089785387	0.219885995
270112		600	5.50E-09	0.00089	0.002233	3.68168	0.94871	0.00125	0.15928	0.00022	17.41055	0.70000	0.00000	0.00000	1.27E+04	0.089414203	0.223251782
280112		624	5.50E-09	0.00091	0.002162	3.60141	0.95503	0.00133	0.16741	0.00022	18.77106	0.70000	0.00000	0.00000	1.80E+04	0.090694005	0.216236289
290112		648	6.00E-09	0.00089	0.002201	3.60121	0.95014	0.00131	0.16754	0.00022	16.93601	0.70000	0.00000	0.00000	1.95E+04	0.089234873	0.220118908
300112		672	6.00E-09	0.00089	0.002208	3.58463	0.95465	0.00123	0.15376	0.00022	17.60927	0.70000	0.00000	0.00000	1.31E+04	0.089146504	0.220778141
310112		696	6.00E-09	0.00090	0.00216	3.58725	0.95502	0.00151	0.16959	0.00022	16.75909	0.70000	0.00000	0.00000	1.65E+04	0.089864052	0.215563228